REPUBLIC OF TÜRKİYE

YILDIZ TECHNICAL UNIVERSITY

GRADUATE SCHOOL OF SCIENCE AND ENGINEERING

MODELLING AND CONTROL OF CARDIOVASCULAR SYSTEMS DIAGNOSTICS AND PREDICTION OF THEIR ANOMALIES

Mehmet İŞCAN

DOCTOR OF PHILOSOPHY THESIS

Department of Mechatronics Engineering

Mechatronics Engineering Program

Supervisor

Assoc. Prof. Dr. Aydın YEŞİLDİREK

Co-Supervisor

Assoc. Prof. Dr. Abdurrahman Kamuran KADIPAŞAOĞLU

July, 2023

REPUBLIC OF TÜRKİYE

YILDIZ TECHNICAL UNIVERSITY

GRADUATE SCHOOL OF SCIENCE AND ENGINEERING

MODELLING AND CONTROL OF CARDIOVASCULAR SYSTEMS DIAGNOSTICS AND PREDICTION OF THEIR ANOMALIES

A thesis submitted by Mehmet İŞCAN in partial fulfillment of the requirements for the degree of DOCTOR OF PHILOSOPHY is approved by the committee on 06.07.2023 in Department of Mechatronics Engineering, Mechatronics Engineering Program.

Assoc. Prof. Dr. Aydın YEŞİLDİREK
Yildiz Technical University
Supervisor

Assoc. Dr. Abdurrahman Kamuran KADIPAŞAOĞLU
Yildiz Technical University
Co- supervisor

Approved By the Examining Committee

Assoc. Prof. Dr. Aydın YEŞİLDİREK, Supervisor
Yildiz Technical University _____

Prof. Dr. Volkan TUZCU, Member
Istanbul Medipol University _____

Assoc. Prof. Dr. Cüneyt YILMAZ, Member
Yildiz Technical University _____

Asst. Prof. Dr. Ertuğrul BAYRAKTAR, Member
Yildiz Technical University _____

Prof. Dr. Murat DOĞRUEL, Member
Marmara University _____

I hereby declare that I have obtained the required legal permissions during data collection and exploitation procedures, that I have made the in-text citations and cited the references properly, that I haven't falsified and/or fabricated research data and results of the study and that I have abided by the principles of the scientific research and ethics during my Thesis Study under the title of "Modelling and Control of Cardiovascular Systems Diagnostics and Prediction of Their Anomalies" supervised by my supervisor, Assoc. Prof. Dr. Aydın YEŞİLDİREK. In the case of a discovery of false statement, I am to acknowledge any legal consequence.

Mehmet İŞCAN

This work was supported by Phinite Engineering and Technology Corporation which Mehmet İŞCAN owns.

Dedicated to my family

and my best friend

and my assistants

ACKNOWLEDGEMENTS

I would like to thank my supervisor Assoc. Prof. Dr. Aydın YEŞİLDİREK for his invaluable supervision, support, and tutelage during the course of my PhD degree. My gratitude extends to the Faculty of Machine for the funding opportunity to undertake my studies at the Department of Mechatronic engineering in Yıldız Technical University. Additionally, I would like to express gratitude to Ali İhsan TAŞ, Berkay GÜRKAN, Ali Burak ÖZDEN for his treasured support which was influential in shaping my experiment methods and critiquing my results. I also thank Mert GÜRKAN brother for their supports. My appreciation also goes out to my family and friends for their encouragement and support all through my studies.

Mehmet İŞCAN

TABLE OF CONTENTS

LIST OF SYMBOLS x

LIST OF ABBREVIATIONS xi

LIST OF FIGURES xiii

LIST OF TABLES xv

ABSTRACT xvi

ÖZET xviii

1 INTRODUCTION 1

1.1 Cardiovascular System 1

1.2 Heart Valves 4

1.3 Cardiovascular Hybrid Mock Loops 8

1.4 Prediction and Diagnostics of Cardiovascular Diseases 11

1.5 Motivation and Hypothesis 13

2 NOVEL AORTIC HEART VALVE MODEL PARAMETERIZING NORMAL AND PATHOLOGICAL CASES: AORTIC STENOSIS AND REGURGITATION 15

2.1 Abstract 15

2.2 Introduction 15

2.3 Material and Methods 19

2.3.1 Leaflet Structure and Analogy of Mass-Spring-Damper Model 19

2.3.2 Valve Blood Flow Resistance 23

2.3.3 State Space Representation of Aortic Valve Dynamics 25

2.4 Experiments and Results 29

2.4.1 The System Tests and Results 30

2.4.2 Pathophysiological Cases: The Aortic Valvular Stenosis and The Aortic Valve Regurgitation 34

2.4.3 Aortic Valvular Stenosis 35

2.4.4 Aortic Regurgitation 36

2.5 Discussion and Conclusion 37

3 A NEW CARDIOVASCULAR MOCK LOOP DRIVEN BY ACTIVE CAPACITANCE IN NORMAL AND ABNORMAL CONDITIONS 41

3.1 Abstract 41

3.2 Introduction 41

3.3 Material and Methods 46

3.3.1 Proposed Hybrid Mock Circulatory Loop 46

3.3.2 System Dynamic Representation 49
3.3.3 A New Volume-Elastance Equation 59
3.3.4 Stability Analysis 62
3.3.5 Error System Dynamics 62
3.4 Results 64
3.5 Discussion 68
3.6 Conclusion 71
4 AN IMRPOVED INSTANTANEOUS AORTIC VALVE RESISTANCE ESTIMATION DURING THE ENTIRE CARDIAC CYCLE USING AI 73
4.1 Abstract 73
4.2 Introduction 74
4.3 Model Based Approach 76
4.3.1 The Proposed I-AVR Estimator Design 76
4.3.2 The Instantaneous Aortic Valve Resistance Integrated Cardiovascular Model 78
4.3.3 The Discretization of the Cardiovascular System and Extended Kalman Filter Design 81
4.3.4 Input Transformation 85
4.3.5 Training and Test Dataset Preparation 86
4.3.6 Convolutional Neural Network 86
4.4 Results 89
4.5 Discussion 93
4.6 Conclusion 95
5 A NOVEL FRAMEWORK TO DIAGNOSE CARDIOVASCULAR DISEASES USING PHYSIOLOGICAL CONSCIOUS DEEP NEURAL NETWORKS 97
5.1 Abstract 97
5.2 Introducition 97
5.3 Framework of the Artificial Cardiologist Assistant 100
5.3.1 Modelling CVS and Morbidity 100
5.3.2 Generation of CV Physiological Dataset for Deep-Learning 103
5.3.3 The PCAE Architecture for CVS 105
5.3.4 Diagnostics Model 109
5.3.5 Use of PCAE for CVD Treatment 110
5.4 Illustrations 110
5.4.1 PCAE Modelling Simulations 111
5.4.2 Excitation of PCAE by Critical Parameters 115

5.5 Conclusion 118
6 CONCLUSION **120**
REFERENCES **123**
PUBLICATIONS FROM THE THESIS **134**

LIST OF SYMBOLS

h	Activation Function
f	Activation Level Function
γ	Angle
A	Area
b	Bias Vector
C	Compliance
g	Conductance
c	Damper Coefficient
ρ	Density
x	Displacement
c	Damper Coefficient
E	Elastance
F	Force
Q	Flow Rate
G	Gravitational Acceleration
L	Inertance
m	Mass
P	Pressure
R	Resistance
k	Stiffness Coefficient
t	Time
τ	Time Constant
v	Velocity
V	Volume
W	Weight Matrix

LIST OF ABBREVIATIONS

AE	Autoencoder
AOP	Aortic Pressure
AS	Aortic Stenosis
AV	Aortic Valve
AVN	Atrioventricular Node
AVR	Aortic Valve Resistance
CCS	Cardiac Conduction System
CNN	Convolutional Neural Network
CO	Cardiac Output
CVD	Cardiovascular Disease
CV	Cardiovascular
CVS	Cardiovascular System
CVST	Cardiovascular Signal Transformation
CVP	Cardiovascular Parameters
D-AVR	Dynamic Aortic Valve Resistance
DL	Deep Learning
DU	Doppler Ultrasound
EKF	Extended Kalman Filter
ECG	Electrocardiogram
FSM	Frank-Starling Mechanism
hMCL	Hybrid Mock Circulatory Loop
LAP	Left Atrium Pressure
LV	Left Ventricle
LVP	Left Ventricle Pressure
LVAD	Left Ventricle Assisted Device
LVQ	Left Ventrcile Flow Rate
LVV	Left Ventricular Volume
MS	Mitral Stenosis
PCAE	Physiologically Conscious Autoencoder
PV	Physiological Ventricle
SA	Sinoatrial Node
SGDM	Stochastic Gradient Descent with Momentum

STD	Standart Deviation
SV	Stroke Volume
SVR	Systemic Vascular Resistance
TPR	Total Peripheral Resistance
TV-LVE	Time Varying Elastance of Left Ventricle
VRC	Vascular Resistance Change
WHO	World Health Organization

LIST OF FIGURES

Figure 1.1 Human circulation system **2**
Figure 1.2 Anatomy of the heart **3**
Figure 1.3 Heart valves **6**
Figure 2.1 Anatomy of the AV **20**
Figure 2.2 The nonlinear model of mass-spring-damper system **21**
Figure 2.3 Simplified geometry of leaflets **23**
Figure 2.4 Improved Mulier model **26**
Figure 2.5 Validation process **30**
Figure 2.6 The LVP and AOP for α =0.1, c=2 ..... **31**
Figure 2.7 AOP and LVP variables for changing parameters **32**
Figure 2.8 Blood flow rate (LVQ) for changing parameters **33**
Figure 2.9 Opening angle variables for changing parameters **34**
Figure 2.10 Comparisons of the reference model, the proposed model, and the physiological outcomes **35**
Figure 2.11 Comparison of the LVP under AS and healthy conditions **36**
Figure 2.12 Comparisons of the physiological parameters under AV regurgitation and healthy conditions **37**
Figure 3.1 Mechanical structure of mock loop design **47**
Figure 3.2 Functional block diagram of the proposed system **48**
Figure 3.3 Results of the numerical and hMCL. a) LVP b) AOP c) LVV d) only hMCL **65**
Figure 3.4 The tracking performance of capacitance. a) Left atrium b) Aorta **66**
Figure 3.5 The results of AS and SVR response: a) LVP b) AOP c) LVV d) Aorticr Resistance e) SVR **67**
Figure 3.6 The results of different heart rate. a) LVP b) AOP c) LVV d) hMCL LVP and AOP **67**
Figure 4.1 The proposed estimation algorithm **77**
Figure 4.2 Aortic valve model [92] **78**
Figure 4.3 Instantaneous aortic resistance integrated cardiovascular analogue model **80**
Figure 4.4 The validation procedures for the proposed estimator **89**
Figure 4.5 The results of LVP, AOP, I-AVC and LVQ in healthy case **90**
Figure 4.6 The results of LVP and AOP, I-AVC and LVQ in aortic stenosis case **91**

Figure 4.7 The results of x, ζ, ζ, θ and A on both the healthy and AS case **92**
Figure 4.8 The results of pressure-volume relation on both healthy and aortic stenosis case **93**
Figure 5.1 Dataset generation of CVS model development **101**
Figure 5.2 Latent variables during dataset generation **104**
Figure 5.3 PCAE based CVD classification **106**
Figure 5.4 Closed loop PCAE operations **110**
Figure 5.5 Validation processs of the proposed PCAE algorithm **111**
Figure 5.6 PCAE principal variables responses to in-silico model and in-vitro device [117] **112**
Figure 5.7 PCAE critical parameter responses to in-silico model and in-vitro device [117] **113**
Figure 5.8 Confusion matrix of the CVS diagnostics model classification **113**
Figure 5.9 Transient response of CVS PVs to externally triggered Emax **115**
Figure 5.10 Healthy case of the CL-PCAE results **116**
Figure 5.11 AS of the CL-PCAE results **116**
Figure 5.12 Systemic resistance change case of the CL-PCAE results **117**

LIST OF TABLES

Table 2.1 Geometrical parameters of the heart model **27**
Table 2.2 Comparison of the proposed model with other works **39**
Table 3.1 Symbols table **49**
Table 3.2 Numerical and hMCL results **69**
Table 3.3 Comparison table under (PV), AS and SVR change **69**
Table 4.1 Symbols table **87**
Table 5.1 CV health condition parameterization **102**
Table 5.2 PCAE data slicing for training and valiadation **105**
Table 5.3 Classification results of CVS data **114**
Table 5.4 Comparison of estimation of CVS parameters **119**

ABSTRACT

Modelling and Control of Cardiovascular Systems Diagnostics and Prediction of Their Anomalies

Mehmet İŞCAN

Department of Mechatronics Engineering

Mechatronics Engineering Program

Doctor of Philosophy Thesis

Supervisor: Assoc. Prof. Dr. Aydın YEŞİLDİREK

Co- supervisor: Assoc. Prof. Dr. Abdurrahman Kamuran KADIPAŞAOĞLU

This thesis presents four innovative methods in the field of cardiovascular research. The first method involves the development of a novel heart valve model that accurately represents physiological patterns such as healthy, aortic stenosis, and regurgitation. The model combines a nonlinear mass-spring-damper representation of the elastic leaflet body's motion with a cardiovascular lumped parameter model, taking into account fluid resistance, flow rate, pressures, and leaflet position. The model successfully demonstrates phenomena such as backflow, vortex formation, dicrotic notch, and reverse pressure effects. The second method introduces a hybrid mock circulatory loop (hMCL) design and control approach for simulating critical cardiovascular diseases. The hMCL incorporates a new left ventricle volume-elastance equation that combines autoregulation and ventricular contractility. The stability of the closed-loop hMCL is demonstrated, and physiological responses to scenarios like aortic stenosis, changes in vascular resistance, and heart rate variations are accurately replicated. The third method presents an improved model for dynamic aortic valve resistance (AVR) using a convolutional neural network (CNN). The model combines "in-silico" and "in-vitro" measurements, and the CNN

is trained to predict AVR residue during the ejection phase. The proposed model outperforms previous methods by considering dynamic AVR and achieves high accuracy in real-time estimation. Finally, the fourth method introduces a framework that integrates "in vitro" and "in silico" measurements to estimate cardiovascular parameters and diagnose cardiovascular conditions. The framework incorporates a modified autoencoder with a partially guided latent space, enabling physiological consciousness integration. The models show accurate estimation of critical parameters and demonstrate the ability to classify the severity of cardiovascular diseases. Overall, these methods advance the understanding of cardiovascular dynamics and enable more accurate simulations, predictions, and diagnostics in cardiovascular research.

Keywords: Autoencoder, Heart Valves, Cardiovascular Modelling, Nonlinear Control, Physiologically Consciousness Neural Network,

ÖZET

Kardiyovasküler Sistemlerin Modellenmesi ve Kontrolü ile Anomalilerin Teşhis ve Tahmini

Mehmet İŞCAN

Mekatronik Mühendisliği Anabilim Dalı

Doktora Tezi

Danışman: Doç. Dr. Aydın YEŞİLDİREK

Eş-Danışman: Doç. Dr. Abdurrahman Kamuran KADIPAŞAOĞLU

Bu tez, kardiyovasküler araştırma alanında bir dizi yenilikçi yöntem sunmaktadır. İlk yöntem, sağlıklı, aort stenozu ve regürjitasyon gibi fizyolojik desenleri doğru bir şekilde temsil eden yeni bir kalp kapak modelinin geliştirilmesini içermektedir. Model, elastik yaprakcık hareketini temsil eden doğrusal olmayan kütle-yay-sönümleyici bir modele, kardiyovasküler bir toplam parametre modeli ile birleştirerek, akış direnci, debi, basınçlar ve yaprakcık pozisyonunu dikkate almaktadır. Model, geri akış, girdap oluşumu, dikrotik girinti ve ters basınç etkileri gibi fenomenleri başarıyla göstermektedir. İkinci yöntem, kritik kardiyovasküler hastalıkları simüle etmek için bir hibrit taklit dolaşım döngüsü (hTDD) tasarımı ve kontrol yaklaşımını tanıtmaktadır. hTDD, oto-regülasyonu ve ventrikül kontraktilesini birleştiren yeni bir sol ventrikül hacim-elastans denklemi içermektedir. Kapalı döngü hTDD'nin kararlılığı gösterilmiş ve aort stenozu, vasküler direnç değişiklikleri ve kalp hızı varyasyonları gibi senaryolara fizyolojik yanıtlar başarıyla kopyalanmıştır. Üçüncü yöntem, dinamik aort kapağı direncini (AKD) daha iyi bir şekilde modellemek için bir evrişimli sinir ağı (ESA) kullanmaktadır. Model, "bilgisayar modellemeli" ve "yapay ortamdaki" ölçümleri

birleştirir ve ESA, eksenleme fazında AKD artığı tahmin etmek üzere eğitilir. Önerilen model, dinamik AKD'yi dikkate alarak önceki yöntemlerden daha iyi performans göstermekte ve gerçek zamanlı tahminde yüksek doğruluk elde etmektedir. Son olarak, dördüncü yöntem, kardiyovasküler parametreleri tahmin etmek ve kardiyovasküler durumları teşhis etmek için " yapay ortamdaki" ve " bilgisayar modellemeli" ölçümleri birleştiren bir çerçeve sunmaktadır. Çerçeve, kısmen yönlendirilmiş bir gizli uzaya sahip modifiye edilmiş bir otokodlayıcıyı içermekte ve fizyolojik bilinçli nöronların entegrasyonuna imkan tanımaktadır. Modeller, kritik parametrelerin doğru tahminini göstermekte ve kardiyovasküler hastalıkların ciddiyetini sınıflandırma yeteneğini sergilemektedir. Genel olarak, bu yöntemler kardiyovasküler dinamiğin anlaşılmasını ilerletmekte ve kardiyovasküler araştırmalarda daha doğru simülasyonlar, tahminler ve teşhisler yapılmasını sağlamaktadır.

Anahtar Kelimeler: Doğrusal Olmayan Kontrol, Fizyolojik Bilinçli Sinir Ağı, Kardiyovasküler Modelleme, Kalp Kapakları, Otomatik Kodlayıcı

1
INTRODUCTION

1.1 Cardiovascular System

In human physiology, the cardiovascular system (CVS) is defined as the collection of systems that has the heart, the vessels carrying clean and dirty blood, and the lung system. This system, which has important functions such as nutrition and heating of the body, actively affects human health by meeting the basic needs of the body. The CVS, which basically consists of two parts (pulmonary and systemic circulation), supplies the circulation of blood in our body and provides metabolic balance based on the requirement of the energy consumption [1]. These two circulations are interconnected via the heart which is the main pressure generator for the whole CVS. In the heart, there are two sections including atriums and ventricles in which the former store the blood to transport through the ventricles and the latter transfer the blood through both the systemic and pulmonary circulation. Figure 1.1 represents the whole circulation system in human body.

In the systemic circulation, the nutrients and oxygen are transported to the organs while carbon dioxide and dirty materials are transferred into the blood. On the other hand, the blood coming from systemic circulation is carried out to the heart in order to oxygenate in the pulmonary circulation. The carbon dioxide diffuses from the pulmonary vessel to the lung resulting in that the blood becomes deoxygenated. The oxygenated blood is called artery which carries the oxygen through the body. When the organs are fed by these nutrient and oxygen, the veins transport the whole venous blood through the heart.

To activate the whole CVS, the heart produces the total activation energy sources to maintain the blood flow cycle of the CVS. It is considered as the only active part of the CVS by electrically contracted which we call cardiac conduction system (CCS) [2].

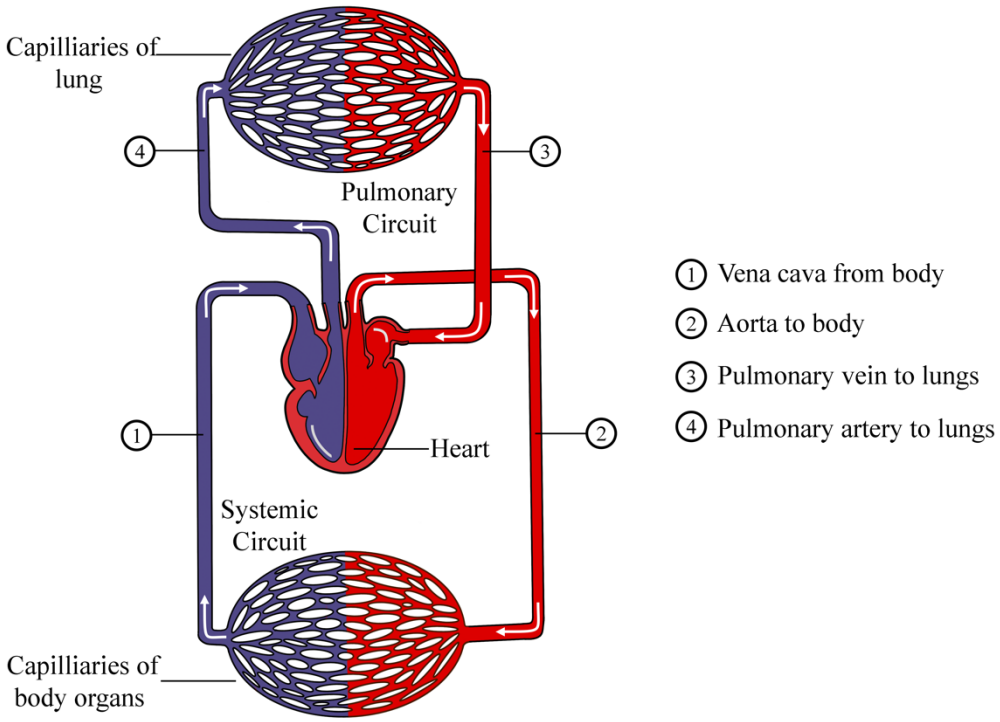


Figure 1.1 Human circulation system

CCS initiates the electrical signals sourced by sinoatrial node (SA) (the heart's pacemaker) to contract the heart muscle in both atrium and ventricles. SA transmit electrical signal into the atrioventricular node (AVN) to synchronize the period of the filling/ejection phase. Then, AV node is triggered by sufficient electrical storage which is greater than its threshold value. The purkinke fibers carries this triggered electrical potential through the whole ventricles. These whole processes are observed by electrocardiogram (ECG) which is a measure of the total electrical activity in the heart [3]. The abnormal conditions concerning CCS can easily be analyzed by using ECG signal which has been reported in many studies [4]–[6].

In CVS physiology, the heart possesses the internal pump activated by CCS in which the heart consists of the cardiac muscle that can lengthening or shorthening in time to generate sufficient pressure. This mechanism paves the way for transferring the blood thourgh either systemic or pulmonary circulation. In order to maintain the whole processes given above, the heart pressurizes the blood in both systemic and pulmonary circulations which are in the range of 10 – 180 mmHg and 2 – 30 mmHg, respectively [7]. These physiological limits directly determine the healthy range for sustaining CVS circulation cycle. Otherwise, the CVS abnormalities happen and to be detected for the CVS diseases.

In order to understand the physiology of the heart, the anatomy and physiological representation of the heart is illustrated in Figure 1.2.

The heart physiologically consists of two parts: the CCS and anatomy which represents the covering features of the heart through a cardiac cycle. In the heart, there are four chambers including the right/left atrium and ventricles. Each of the sections is restricted by heart valves such as mitral, aortic, pulmonary, and tricuspid valves in order to continue the rhythmic operation in cardiac cycle. Especially for the pulmonary and tricuspid valves, these are utilized to complete the pulmonary circulation in order to enrich oxygenate the blood. Besides, the mitral and aortic valves (AV) condition the systemic circulation loop by those opening/closing phase. Left side of the heart is associated with the systemic circulation while right side of it creates the pulmonary circulation loop.

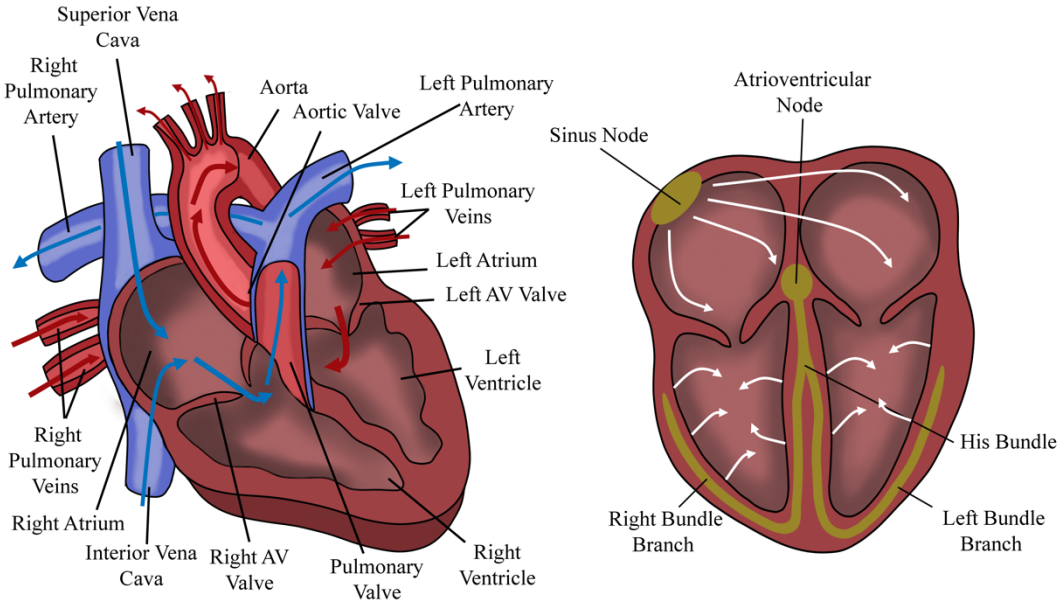


Figure 1.2 Anatomy of the heart

In cardiac cycle, there are two phases: systole and diastole in which the former is related to the contraction phase of the heart and the latter one is associated with the relaxation one. In the time course, the CCS initiates the electrical propagation of the heart by SA. Then, the cardiac muscle is contracted in order to generate the sufficient pressure for transporting the blood through both the pulmonary and

systemic circulation. When the contraction phase is done, the diastole phase is begun for filling the heart chamber due to the relaxation of the cardiac muscle. Generally, the time course of the cardiac cycle is driven in rhythmic period at the rate of 60 – 150 bpm for the resting adult. The only task is to transfer the blood into these circulations. In order to evaluate the performace of this physiological condition, the cardiac output (CO) which is the ratio of how much blood is circulated for a minute in the body, is an important indicator for diagnosing the cardiac states of the CVS. Generally, it is almost equal to 5 l/min for a resting adult and may vary for the abnormal CVS cycles [8].

For this synchronicity, there is one reported mechanism to regulate the CVS response which we call “Frank-Starling Mechanism” (FSM). FSM describes the direct relation between the stroke volume (SV) and end-diastolic volume in which the former represents the transferred blood volume in the ventricles and the latter is the end volumetric value of the ventricle at the end of diastole phase [9]. The time responses of cardiac muscle entirely depend on the length-tension relationship between cardiac muscle deflection and force values [10]. When the increase in blood volume at the end of diastolic phase, the cardiac muscle can produce higher contraction rate with respect to the length-tension relationship of cardiac one. This feature permits the synchronicity of CO with the venous return which means that CVS regulation is constantly maintained without any external inputs to the heart. It is noteworthy that the autonomous physiological property of the heart is highly contributed by FSM as well as CCS in which these two physiological properties construct the cardiac cycle while the other parts are regulated by the baroreflex or sensory output feedback system in CVS.

1.2 Heart Valves

Especially for the continuity of the blood flow rate in CVS, the active part of CVS which we call “the heart” is split into the two phases: systole and diastole described in the previous section. In the heart, the systole and diastole phase are actualized by CCS-induced electrical propagation in terms of contraction and relaxation on cardiac muscle. However, the requirement of the filling and ejection phases is not only depended on CCS mechanism but also mechanical valve which can be opened and closed with respect to the difference between inlet and outlet pressure values.

Heart valves play a crucial role in the proper functioning of the CV system. Understanding their physiology, anatomy, and importance is essential for comprehending the complex dynamics of the cardiac cycle and the impact of valve-related diseases.

Heart valves are specialized structures located within the heart that regulate blood flow, ensuring unidirectional movement and preventing backflow. The human heart consists of four valves: the tricuspid valve, the mitral valve, the pulmonary valve, and the AV. These valves consist of thin leaflets or cusps, composed of connective tissue covered by endothelial cells, and are attached to a supporting fibrous ring known as the annulus. The leaflets open and close in response to pressure changes during the cardiac cycle, allowing blood to flow in the desired direction.

Heart valves serve as vital components of the cardiovascular system (CVS), facilitating the efficient and regulated flow of blood throughout the body. By ensuring unidirectional flow, they prevent the backward flow of blood, maintaining the forward propulsion necessary for proper circulation. Heart valves also contribute to the maintenance of optimal blood pressure and CO, as well as the distribution of oxygen and nutrients to various organs and tissues.

There are four mechanical valves in the heart anatomy: tricuspid, pulmonary, aortic and mitral one [11]. For the pulmonary circulation, the tricuspid and pulmonary valves permit the blood to be transported from the lung to the heart. In physiological nature, these valves are operated in the pressure ranges of 5 – 30 mmHg which means that it is highly small values to degenerate the valve structures compared to the aortic and mitral valves. The aortic and mitral valves enable to condition the cardiac cycle periods to be filled or ejected the blood in the systemic circulation [12]. The physiological range of the systemic circulation is within 10 – 150 mmHg which is highly huge change resulting in the physiological problems or abnormalities especially on the AV. The general demonstration of the heart valves is given in Figure 1.3.

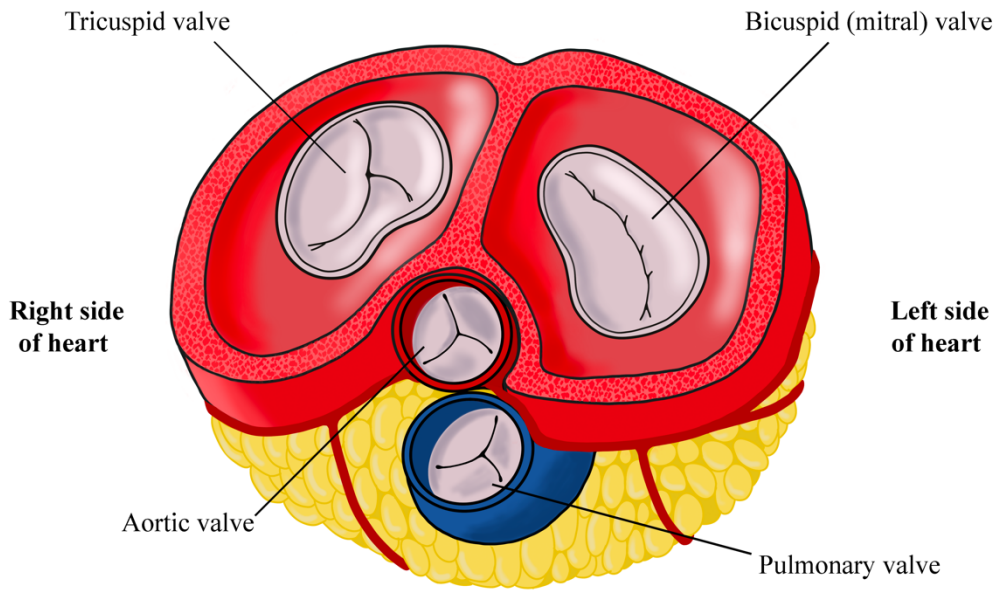


Figure 1.3 Heart valves

The heart valve consists of leaflets which partially closes the route between either the heart chambers (mitral and tricuspid) or circulation loops (aortic and pulmonary). Each leaflet has elastic body which can lengthening or shorthening in order to open or close the heart valves. Each of the leaflet can move forward or backward direction under the applied pressure difference for transporting sufficient blood into another CVS chamber. All heart valves posses three leaflet except the mitral one in which the formers are applied higher pressure difference then the mitral one.

In systole, the ventricles contract, and the tricuspid and mitral valves close to prevent the backflow of blood into the atria. Simultaneously, the pulmonary and AVs open, allowing blood to be ejected from the ventricles into the pulmonary artery and aorta, respectively. In diastole, the ventricles relax, and the tricuspid and mitral valves open, enabling the filling of the ventricles with blood from the atria. At the same time, the pulmonary and AVs close to prevent the regurgitation of blood back into the ventricles.

Scientific investigation of heart valves is essential for several reasons. Firstly, it enhances our understanding of the normal physiology and functioning of heart valves, aiding in the development of improved diagnostic and therapeutic strategies. Secondly, investigating heart valves allows for the identification and

characterization of valve-related diseases, leading to early detection, appropriate management, and the development of targeted interventions. Additionally, understanding the underlying mechanisms of valve diseases can contribute to the development of novel therapies and the optimization of surgical techniques.

To the best of our knowledge, the functionality of the heart valves has been stuied a lot in order to understand the underlying mechanism of them in terms of CV conditions such as normal and abnormal one [13], [14]. Especially for the abnormal conditions, there has been many treatments and drug-induced method to recover the CVD. In spite of the present methods, the treatment process of the heart valves is highly expensive due to the invasive operation on CVS resulting the limited number of solutions that leads to understand the underlying mechanism of the heart valves. There have been many attempts to model the heart valve analogy in computer simulation program in order to eliminate the dependency of the invasive operation. However, there is a need to perform some improvements on the modelling of the heart valves.

On the other hand, the heart valves posses a considerable effect on the physiology of the CVS since they condition the CVS functionality depending on the pressure and flow rates of the blood in each chamber of the CVS. Therefore, it is important to develop the general solution especially in both invasive and noninvasive methods in order to comprehend the dynamic behaivour in the CVS.

Especially for the systemic circulation, the AV is located between the left ventricle (LV) and the aorta, the largest artery in the body. It consists of three semilunar cusps, known as the right, left, and posterior cusps. The AV opens during systole when the pressure in the LV exceeds the pressure in the aorta, allowing blood to be ejected into the systemic circulation. During diastole, the AV closes, preventing the backflow of blood into the ventricle.

Several CVDs can affect the AV. Aortic stenosis (AS) is a common condition characterized by the narrowing of the valve opening, restricting blood flow from the LV into the aorta. Aortic regurgitation, on the other hand, involves the leakage or backward flow of blood from the aorta back into the LV during diastole. These conditions can lead to significant cardiovascular (CV) complications, including reduced CO, heart failure, and increased workload on the heart.

1.3 Cardiovascular Hybrid Mock Loops

CVDs remain a significant global health concern, necessitating innovative approaches to study and treat these conditions. In recent years, the hybrid mock circulatory loops (hMCL) have emerged as a promising methodology to overcome the limitations of traditional research methods. The complexity of CV physiology requires a comprehensive understanding of the interactions between the heart, blood vessels, and other vital organs. Traditional research methods, such as in silico (computer simulations), in vitro (laboratory experiments), and in vivo (animal studies), each have their strengths and limitations. However, they often fall short in capturing the dynamic and integrated nature of the circulatory system.

CV hMCL loops combine in silico modeling with physical circulatory components to create a dynamic and realistic experimental platform [15]. These loops simulate the flow of blood through a closed circuit that incorporates anatomically representative components, such as artificial blood vessels, valves, and chambers, which interact with computational models of the heart and other organs. The integration of computational simulations with physical circulatory components allows for a more accurate representation of physiological conditions and facilitates real-time interaction between the computational models and the circulatory system.

In silico tests involve computer simulations that use mathematical models to simulate physiological processes [16]. While they can provide insights into the behavior of the circulatory system, they may lack the complexity and variability observed in real biological systems. In vitro tests utilize isolated cells, tissues, or organs in laboratory settings. While they offer better control over experimental conditions, they may not fully capture the integrated interactions of the circulatory system. In vivo tests involve studies conducted on living organisms, typically animal models. While they provide a holistic representation of CV physiology, they can be expensive, time-consuming, and may not accurately reflect human pathophysiology.

Among the three approaches, in vitro testing offers several advantages. Firstly, it allows for controlled experimentation in a simplified yet representative environment. Researchers can manipulate variables, introduce specific conditions, and evaluate responses with greater precision. Secondly, in vitro models facilitate

the inclusion of human-specific parameters, enabling a more accurate representation of human CV physiology compared to animal models. Additionally, ethical concerns associated with animal studies can be mitigated by employing in vitro models. However, in vitro testing alone may still lack the complexity and dynamic interactions observed in the intact circulatory system.

CV hMCL offer a unique solution to bridge the gap between in silico and in vitro approaches, providing a more comprehensive understanding of circulatory dynamics [17]. By integrating computational models with physical circulatory components, these hybrid systems enable the evaluation of interventions, the investigation of disease mechanisms, and the optimization of medical devices in a realistic and dynamic setting. They allow for the inclusion of patient-specific parameters, facilitating personalized medicine approaches and the development of tailored treatment strategies. Moreover, CV hMCL enable researchers to study the systemic effects of interventions and simulate various physiological conditions, advancing our knowledge of CV pathophysiology and improving patient outcomes.

The AV induced CVDs have been extensively explained covering the AS and regurgation conditions. The utilization of hMCL device offers great advantages in testing AVs as well as modelling on the hybrid computational model. The advantages of using hMCL for AV testing:

- *Improved Physiological Relevance:* CV hMCL provides a more realistic representation of the human CV system compared to traditional testing methods. These loops incorporate anatomically accurate models of the heart, blood vessels, and associated structures, allowing for the replication of realistic hemodynamics. This enables researchers to assess AV performance under physiological conditions, considering factors such as pressure, flow rates, and CO.
- *Reproduction of Complex Flow Patterns:* CV hMCL allows for the replication of complex flow patterns observed in the human CV system. This is particularly important for assessing AV functionality, as the valve experiences varying flow velocities and turbulence during different phases of the cardiac cycle. By accurately reproducing these flow patterns, researchers can evaluate the valve's ability to open and close effectively, preventing backflow and ensuring efficient blood flow.

- *Flexibility in Simulation:* hMCL provide researchers with the flexibility to simulate various disease scenarios and pathologies related to AVs. For example, conditions such as AS or regurgitation can be mimicked by altering flow rates or introducing specific anatomical abnormalities. This capability allows for a comprehensive assessment of valve performance under different pathological conditions and aids in the development of improved diagnostic and treatment strategies.
- *Evaluation of Valve-Device Interactions:* With the advancements in medical device technology, CV hMCL offer a valuable platform to assess the interaction between AVs and prosthetic devices. These loops enable researchers to simulate the implantation of different types of prosthetic valves and evaluate their hemodynamic performance. This information is crucial for optimizing prosthetic valve design, minimizing complications, and enhancing patient outcomes.
- *Potential for Personalized Medicine:* hMCL can facilitate personalized medicine approaches in AV testing. By incorporating patient-specific parameters, such as anatomical data, hemodynamic profiles, and pathology characteristics, researchers can evaluate the performance of AVs in individual patients. This personalized approach can aid in the selection of appropriate treatment strategies, optimization of valve interventions, and improvement of patient outcomes.

The hMCL has also been utilized to replicate the FSM in literature. The advantages of using hMCL for Testing the FSM are given as follows:

- *Realistic Reproduction of Hemodynamics:* hMCL provide a more realistic and physiologically relevant representation of hemodynamic conditions compared to traditional experimental setups. These loops incorporate anatomically accurate models of the heart, blood vessels, and associated structures, enabling researchers to replicate the dynamic changes in preload and afterload that occur during the cardiac cycle. This allows for a more accurate assessment of the FSM and its modulation of cardiac performance.
- *Precise Control over Experimental Parameters:* hMCL offer researchers precise control over experimental parameters such as preload, afterload, and heart rate. By manipulating these parameters, the relationship between

preload and SV can be systematically investigated. This level of control allows for a detailed characterization of the FSM, including the determination of optimal preload conditions for maximizing CO.

- *Simulation of Pathological Conditions:* hMCL provide the ability to simulate various pathological conditions that affect the FSM. For example, conditions like heart failure or myocardial infarction can be replicated by altering parameters such as contractility or compliance. This enables researchers to study the impact of pathological changes on the FSM and explore potential therapeutic interventions.
- *Assessment of Ventricular Function and Performance:* By incorporating pressure and volume sensors within the hMCL, researchers can obtain real-time measurements of ventricular function and performance. This includes parameters such as SV, ejection fraction, and CO. These measurements allow for a quantitative evaluation of the FSM and its influence on overall cardiac performance.
- *Validation of Computational Models:* hMCL provide an invaluable platform for validating and refining computational models that simulate the FSM. Experimental data obtained from the mock circulatory loops can be used to verify the accuracy and predictive capabilities of these models, enhancing our understanding of cardiac function and guiding the development of computational tools for studying the FSM.

1.4 Prediction and Diagnostics of Cardiovascular Diseases

Nowadays, the prediction and diagnostics of CVD have become the paramount importance in order to get the early risk identification, proactive management and tailored treatment strategies [18]. Accurate prediction models and reliable diagnostic tests allow for the early identification of individuals at risk of developing CVDs. Early recognition enables targeted interventions, lifestyle modifications, and preventive measures to mitigate or delay disease progression. Prediction and diagnostics facilitate proactive disease management by enabling the early detection of CV abnormalities. Timely identification allows for prompt medical interventions, lifestyle modifications, and appropriate pharmacological treatments, which can slow disease progression and reduce associated complications. Accurate

prediction and diagnostics aid in tailoring treatment strategies to individual patients. With a better understanding of disease progression and risk factors, healthcare providers can personalize therapeutic approaches, optimizing treatment outcomes and minimizing adverse events.

Besides, AS and regurgitation are important indicators in the prediction and diagnostics of CVDs. AS and regurgitation are common and significant valvular disorders that affect the proper functioning of the heart. These conditions can be identified through clinical examinations, imaging techniques such as echocardiography, and other diagnostic tests. The presence and severity of AS and regurgitation provide valuable information for predicting and diagnosing CVDs. AS and regurgitation are associated with an increased risk of adverse CV events [19]. They are indicators of underlying structural and functional abnormalities in the heart, including hypertrophy, impaired ventricular function, and compromised CO. Recognizing and monitoring these conditions can help identify individuals who may be at higher risk for developing other CVDs [20].

Additionally, the FSM plays a crucial role in predicting and diagnosing CVD. The FSM describes the relationship between preload (end-diastolic volume) and SV in the heart. By evaluating this mechanism, clinicians can assess cardiac function and determine if there are impairments or abnormalities. Changes in the Frank-Starling relationship can indicate underlying CVDs, such as heart failure or myocardial infarction. The FSM helps predict disease progression by assessing the heart's ability to adapt to changes in preload. Alterations in the Frank-Starling relationship may indicate a compromised ability of the heart to pump blood effectively, leading to the development or progression of CVDs.

Aforesaid, the researchers should utilize CV hybrid mock loops in the prediction and diagnostics of CVDs. CV hybrid mock loops can replicate realistic hemodynamic conditions, allowing for accurate assessment of cardiac function and prediction of disease progression. These loops incorporate anatomically accurate models, enabling researchers to simulate disease scenarios and evaluate diagnostic markers. The hMCL can be customized to incorporate patient-specific parameters, such as anatomical data and pathological characteristics. This facilitates personalized medicine approaches by evaluating disease progression and response to treatment in individual patients. Mock circulatory loops provide a controlled

environment for validating and refining diagnostic tests. By comparing test results obtained from mock circulatory loops to clinical data, scientists can assess the accuracy and reliability of diagnostic tools, enhancing their predictive capabilities. Researchers can utilize mock circulatory loops to evaluate the efficacy of different treatment strategies, such as drug therapies or surgical interventions. These loops allow for the assessment of hemodynamic changes and functional outcomes, aiding in the optimization of treatment approaches.

In conclusion, the prediction and diagnostics of CVDs are essential for early risk identification, proactive management, and tailored treatment strategies. AS and regurgitation are important indicators in the prediction and diagnostics of CVDs, providing valuable information for risk assessment and identifying individuals at higher risk. The FSM is crucial in predicting and diagnosing CVDs by assessing cardiac function and predicting disease progression. Utilizing CV hybrid mock loops provides scientists with the means to replicate physiological conditions, facilitate personalized medicine approaches, validate diagnostic tests, and optimize treatment strategies. By harnessing these tools, scientists can advance our understanding of CVDs and improve patient care.

1.5 Motivation and Hypothesis

The extensive descriptions of the CVS and the related CVD have been explained in order to understand the main purpose of the proposed thesis. This thesis presents several innovative methods in the field of cardiovascular research. The first method introduces a novel heart valve model that accurately represents physiological patterns such as healthy, aortic stenosis, and regurgitation. The model combines a nonlinear mass-spring-damper representation of the elastic leaflet body's motion with a cardiovascular lumped parameter model, considering fluid resistance, flow rate, pressures, and leaflet position. The motivation behind this research is to develop a model that approaches the gold standard in physiological evaluation and includes additional phenomena like backflow and reverse pressure effects. The hypothesis is that the novel model can accurately simulate the physiological patterns and demonstrate the newly observed phenomena. The model's parameters are selected and validated through comparisons with reference models and physiological data, ensuring accurate representation of cardiovascular dynamics.

The second method presents a new design and control approach for a hybrid mock circulatory loop (hMCL) used in simulating critical cardiovascular diseases. The goal is to create a stable closed-loop system that accurately replicates physiological responses. The hypothesis is that by incorporating a left ventricle volume-elastance equation combining autoregulation and ventricular contractility, the hMCL can drive proportional valves and generate physiological pressures. The performance of the hMCL is evaluated by comparing its simulations with human data under various scenarios, including aortic stenosis, changes in vascular resistance, and heart rate variations. The hypothesis is validated by demonstrating that the hMCL can accurately replicate physiological responses and maintain consistent pressures.

The third method presents an improved model for dynamic aortic valve resistance (AVR) using a convolutional neural network (CNN). The motivation is to estimate AVR during the ejection phase and provide a powerful dynamic model. The hypothesis is that by combining "in-silico" and "in-vitro" measurements and utilizing a CNN, accurate real-time estimation of AVR can be achieved. The proposed model is validated using a hybrid mock circulatory loop (hMCL) and demonstrates high accuracy in estimating AVR for the ejection phase.

The fourth method introduces a framework that integrates "in vitro" and "in silico" measurements to estimate cardiovascular parameters and diagnose cardiovascular conditions. The framework incorporates a modified autoencoder with a partially guided latent space, allowing for the inclusion of physiological consciousness. The goal is to track left ventricle elastance deviation, mitral stenosis, aortic stenosis, and changes in systemic vascular resistance. The hypothesis is that by training the autoencoder on labeled datasets generated from "in-silico" data and validating it using in-vitro tests, accurate estimation and diagnosis of cardiovascular conditions can be achieved. The results demonstrate high accuracy in reproducing cardiovascular signals and the ability to classify the severity of cardiovascular diseases.

Overall, these methods aim to advance the understanding of cardiovascular dynamics, provide more accurate simulations and predictions, and enable improved diagnostics in cardiovascular research.

2
NOVEL AORTIC HEART VALVE MODEL PARAMETERIZING NORMAL AND PATHOLOGICAL CASES: AORTIC STENOSIS AND REGURGITATION

2.1 Abstract

In this paper, a novel heart valve model with parameters selections enabling to illustrate some physiological patterns such as healthy, AS and regurgitation has been shown. The motion of the elastic leaflet body is modeled by a nonlinear mass-spring-damper and coupled with a CV lumped parameter model. As a result, our model takes in to account a single continuous time-varying fluid resistance, the aortic flow rate, left ventricular and AOPs, and the leaflets' pose. This novel model is able to show the backflow, vortex and dicrotic notch phenomenon as approaching to the gold standard in physiological evaluation. The model also additionally presents reverse pressure effect on the AV in the diastolic phase that are not observed in the recent literature. The physiological validation is performed by comparing two reference models and previously reported on physiological data. Nominal leaflet spring (α) and damping (c) parameters have been determined for the healthy valve (α=0.1, c=2), AS (α=0.005, c=0.1), and aortic regurgitation (α=0.001, c=2). When compared to other studies, the left ventricular and AOP, leaflets' opening-closing angles are generated in similar patterns. Additionally, the reduction of the blood flow rate can now be observed in aortic regurgitation which is not presented in the literature. In conclusion, a set of critical AV conditions is parameterized by our novel model. The elastic structure of the leaflet model enabling us to demonstrate not only the vortex and dicrotic notch phenomenon but also the backflow and reverse pressure effect. Furthermore, it offers a generalized framework to realize extensive AV conditions.

2.2 Introduction

The cardiovascular system (CVS) plays a crucial role in the transportation of essential exchange materials, such as oxygen, nutrients, which are carried by the blood to and from the organs within the human body. According to the World

Health Organization (WHO) report, cardiovascular diseases (CVDs) are responsible for 17.9 million deaths worldwide in 2019, representing more than 30% of all [21]. One of the CVDs, heart valve dysfunction is considered as the primary cause of malfunctioning of the CVS as well as the heart [22]. Nowadays, about 300000 valve replacement surgeries are being performed on an annual basis, and this figure is predicted to triple within the next 30 years as the population ages [23]. Therefore, system modeling of the heart valve in terms of an engineering design approach becomes crucial for treating any heart disease.

Due to their crucial role in regulating blood flow and the cardiac cycle, all valves within the CVS are considered vital components. However, special attention is given to the AV, which holds particular significance. The AV acts as a separation between the LV and the aorta, the main conduit carrying blood from the heart to the muscles and organs. Moreover, it serves as the point of origin for the coronary arteries [24]. Valves characterized by triangular-shaped leaflets are referred to as cusps. During systole, the aortic leaflets facilitate the outflow of blood from the heart, while during diastole, they prevent backflow, ensuring a unidirectional flow from the ventricles to the arteries. Flow in the aorta follows a laminar flow regime, and the valve does not impede forward flow during systole. However, if the valve experiences stenosis, resulting in narrowing, turbulent jet flow may occur, leading to the detection of minimal backflow and turbulent eddies [25]. The presence of these eddies causes alterations in blood flow velocity, a phenomenon worth considering in advanced models. Moreover, stenosis may perturb ventricular pressure, thereby influencing flow regime and leaflet closure characteristics. Consequently, modeling the aortic sinuses becomes significant. The aortic sinuses, also known as the sinuses of Valsalva, are regions within the aortic root that are bordered by the AV cusps on the inside and the outward bulges of the aortic walls on the outside [26]. Physiological studies have revealed that the elastic recoil of the sinuses contributes to valve closure [27]. Sinus vortices and valve shape represent additional physiological phenomena that necessitate examination when transitioning from physiology to an analogical flow model. At the onset of the heart's contraction phase, the AV closes. As it rapidly opens, vortices form between the leaflets and the sinus walls, and the leaflets subsequently return to a position where the centers of their free margins slightly protrude into the sinuses. Although

this phenomenon significantly affects steady flow through the valve, existing AV models in the literature often overlook it. The vortices gradually dissipate during the latter phase of systole while continuing to impact blood flow patterns and control features of the valve [28].

Mathematical modeling studies concerning the AV in existing literature commenced with a simplistic representation, analogously likening it to a 'diode' within a unidirectional flow context [29]. In this model approach, the valve operates akin to a diode in the 'on' mode when ventricular pressure matches arterial pressure. This enables blood to flow into the aorta, subsequently facilitating systemic circulation throughout the body's muscles and organs. As the systole phase concludes, the AV autonomously closes, transitioning into the diode 'off' mode. However, this analogy assumes that blood flow through the valve and into the aorta remains unidirectional and constant, which inadequately captures heart failures associated with the AV, such as AV stenosis and valvular regurgitation. In cases of valve stenosis, as discussed earlier, muscle mass diminishes and thickness narrows, leading to potential alterations in the local flow pattern. Additionally, valvular heart diseases can induce variations in valve stiffness [30]. Consequently, these proposed AV models must account for such changes to facilitate accurate diagnosis and treatment procedures. Enhancing and optimizing the models entails tailoring the parameters of system dynamics for each specific heart disease, thereby improving their utility and applicability.

In the context of lumped parameter modeling in the CVS, the hydraulic resistance, influenced by the leaflet physiology, has conventionally been treated as a constant variable assessed within the state space representation of the Windkessel model [31]. However, it is important to account for the dynamic nature of valve physiology and allow for adjustable resistance values. Therefore, it becomes essential to analogically mimic the behavior of the heart valve. It is worth noting that the AV comprises not only soft tissue but also involves hydraulic resistance within the system modelling. A potential approach to modeling the AV involves employing a second-order dynamical system, analogous to a nonlinear mass-damper-spring model. This modeling approach can capture the diverse physiological conditions exhibited by the valve, including thinning, thickening, scarring (stenosis), and regurgitation, thus facilitating a more comprehensive system design perspective.

In the existing literature, Korakianitis et al. present a study on heart valve dynamics, focusing on the coupling of the CVS and the AV model, considering both healthy and aortic regurgitation conditions [32]. Aboelkassem et al. develop a mathematical model specifically addressing the AV, incorporating sinus vortices and capturing the opening-closing phases of the leaflets [33]. Their model successfully accounted for the dicrotic notch and effective orifice area in dynamic simulations. Additionally, Laubscher et al. proposed a lumped parameter model that integrated both the CV and AV systems, examining healthy conditions as well as AS by adjusting parameters associated with loss characteristics and orifice area [34]–[36]. However, these models do not account for the reverse pressure effect exerted on the AV during the diastole phase. Furthermore, previous studies do not calculate the time-varying resistance parameter for the AV, based on the movements of the leaflets within the AV structure.

In this study, we propose a novel dynamic model for the aortic valve that represents the physiological response of the valve using a nonlinear mass-damper-spring system. The model incorporates the active systolic pressure and left ventricular flow rate (LVQ) as state variables. The model outputs include LVQ, aortic opening pressure (AOP), opening-closing angle, and left ventricular pressure (LVP). Additionally, the stiffness and damping ratio of the leaflet model are dynamically assessed. By appropriately setting these coefficients, the time-varying resistance of the AV is derived from the leaflet motion, considering parameters such as the opening-closing angle, leaflet deflection, and adjustable factors. This approach enhances the controllability and adaptability of the system, enabling simulation of various physiological conditions, including AS and regurgitation. AS refers to the narrowing and stiffening of the valve opening, while regurgitation involves the backflow of blood from the LV to the aorta through the valve [37], [38]. Notably, this model incorporates the reverse movement of the leaflets, which is an advancement compared to previous models in the literature. The study also investigates the dynamic flow properties of the soft tissue-blood system, including the formation of eddies, vortex, AV, and time-dependent changes in muscle resistance. A comprehensive state space representation is presented, specifically designed to reflect the physiological properties of AVs in terms of nonlinear time-varying aortic resistance within the cardiovascular system (CVS). While traditional

heart models organize the state variables for each heart chamber into a matrix form, with four different variables describing each valve [39]. , our approach establishes a single state-space model that adequately captures valve flow and pumping speed. Drawing upon the Mulier model, the dynamics of the leaflets are described through relevant equations and parameters [40]. The proposed approach is implemented and tested using a SimulinkTM model, which incorporates the anticipated leaflet dynamics. Overall, these novel improvements contribute to the development of a comprehensive AV model suitable for studying and controlling various physiological heart valve diseases.

2.3 Material and Methods

This section will introduce the proposed AV model, which incorporates a mass-spring-damper analogy to represent the behavior of the leaflets and derives a hydraulic resistance equation for the LVQ. Firstly, the anatomical characteristics of the AV are discussed to establish the analogy between the mass-spring-damper system and the valve's properties. Secondly, the geometric interpretation of the leaflets is presented, outlining the underlying assumptions that make the application of the mass-spring-damper analogy appropriate. Thirdly, a novel equation for hydraulic resistance is derived based on the displacement of the leaflets within the proposed mass-spring-damper structure.

2.3.1 Leaflet Structure and Analogy of Mass-Spring-Damper Model

Figure 2.1 illustrates the anatomical structure of the (AV) placed at between the LV and the aorta. The AV consists of three leaflets that can open or close with respect to the difference between the LVP and AOP. These leaflets possess both mass and elastic properties, allowing them to elongate or contract in response to the applied pressure difference [41]. To capture this elastic behavior, a nonlinear spring coefficient will be employed in the modeling process. Moreover, during the opening-closing phase, the leaflets can experience acceleration or deceleration due to the forces exerted by the pressure difference. Additionally, since the leaflets are exposed to the blood flow, hydraulic friction and losses are inevitable. Consequently, incorporating a damping factor becomes crucial for enhancing the realism and fidelity of the model in mimicking the physiological response of the leaflets.

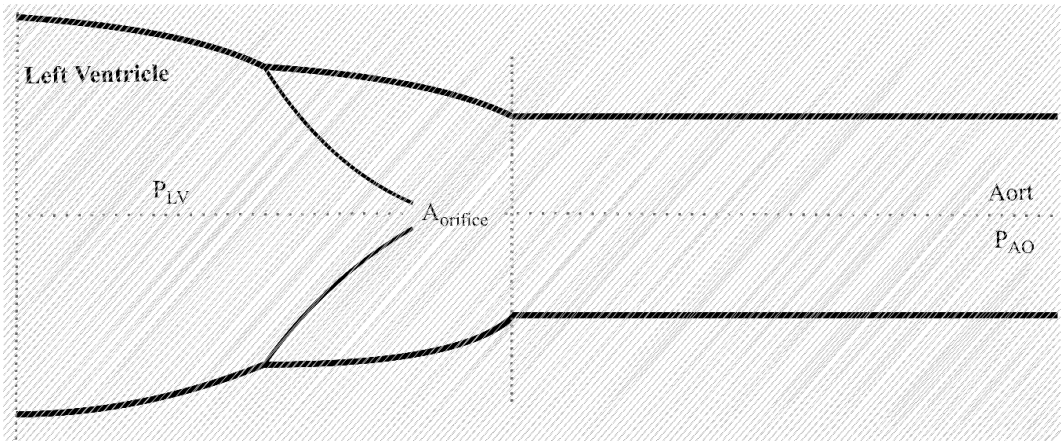


Figure 2.1 Anatomy of the AV

Figure 2.2 presents a representation of each leaflet as a mass-spring-damper system, where the mass coefficient corresponds to the leaflet's mass, and the spring factor reflects its flexibility, and the friction factor accounts for the damping ratio that characterizes energy losses within the blood pool. The following assumptions have been made:

- The aortic wall is considered to be completely rigid, or its influence on dynamics is deemed negligible.
- Significant hydraulic losses resulting from friction along a narrow pathway are deemed negligible.
- Compression effects within the blood are disregarded.
- There is no hydraulic storage or acceleration within the aortic section.
- The leaflets are assumed to possess symmetry.
- The AV is assumed to be closed at a nominal leaflet angle of 45°.
- The total length of the leaflets remains constant.

These assumptions are the basis for the model and provide a simplified representation of the AV dynamics, enabling a focused examination of key variables and behaviors while acknowledging certain limitations inherent in the system.

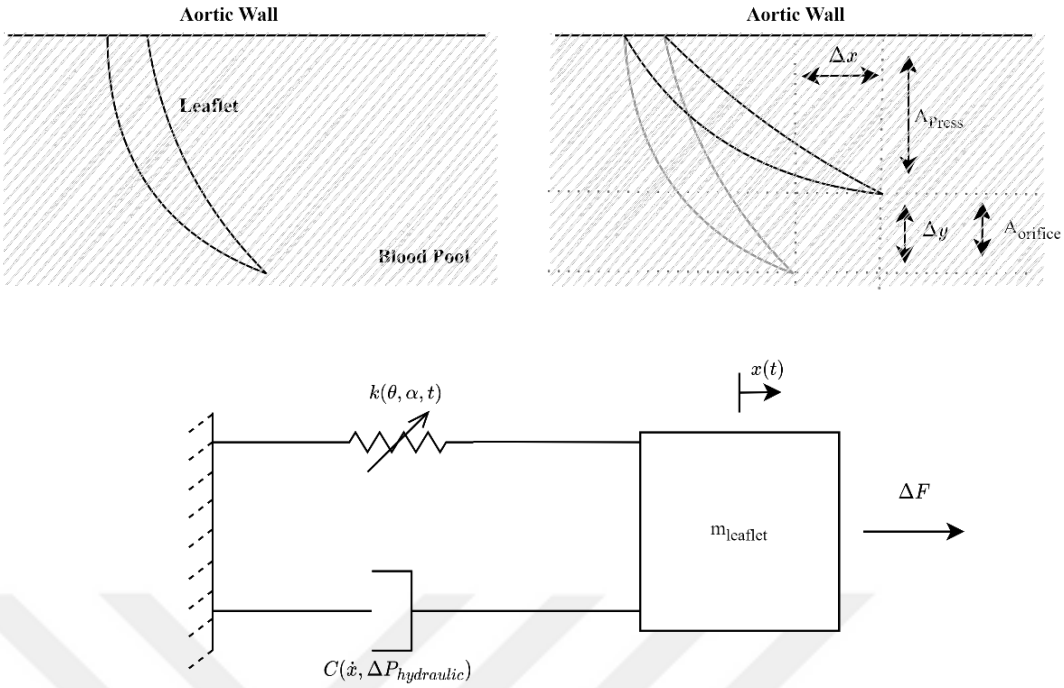


Figure 2.2 The nonlinear model of mass-spring-damper system

Under these assumptions, the general form of the nonlinear mass-spring-damper equation can be written as in (2.1).

$$m\ddot{x} + c\left(\dot{x},\ \Delta P_{hydraulic}\right)\dot{x} + k(x, \theta, \alpha)x = \Delta F \qquad (2.1)$$

where ΔF is the total force on leaflets; m, c, and k are mass, damping, and stiffness coefficients of leaflets respectively. The leaflet displacement is indicated with $x(t)$. In Figure 2.2, $A_{orifice}$ stands for the leaflet orifice area (blood flow area), while L is the distance between the peak point of the leaflet's intersection and the lateral tissue wall.

There are three leaflets in the AV; however, one mass-spring-damper model can be built to provide a physiological response since the symmetry rule combines the leaflet dynamics into one equation of motion. The total related force applied on leaflets is sourced by pressure balance between the LV (P_{lv}) and aorta (P_{ao}) which can be described by (2.2):

$$\Delta F = \Delta P \cdot A_{press}(x) = (P_{lv} - P_{ao}) \cdot A_{press}(x) \qquad (2.2)$$

where A_{press} is the area in which the fluid is exposed on. From the geometric perspective of the leaflets, A_{press} can be calculated as

$$A_{press}(x) = A_{total} - A_{orifice}(x) \tag{2.3}$$

where A_{total} is the total area of the aortic region, and $A_{orifice}$ is the orifice area which let the blood flow.

$A_{orifice}$ can easily be calculated using geometrical theorems with its graphical representation, illustrated in Figure 2.3.

In this case, the displacement $x(t)$ is assigned to the leaflet endpoint since the negative and positive pressure effect can now be obtained from the deflection feature using this variable. From the Pythagorean Theorem, we get,

$$\lambda^2 = \left(\frac{L}{\sin(\theta)}\right)^2 = (L-y)^2 + (L+x)^2 \tag{2.4}$$

with the initial condition of $x(0) = 0, y(0) = 0$. Right hand side of the triangle can be deflected by the effect of changing $y(x)$ which means that it is a function of deflection rate at $x(t)$. Therefore, deflection rate at vertical axis can be generated by

$$(L-y)^2 = \left(\frac{L}{\sin(\theta)}\right)^2 - (L+x)^2 \tag{2.5}$$

The result deflection rate can now be utilized to find area of leaflet which is given by (2.6).

$$A_{orifice}\,(x) = \pi \cdot \left(L - \sqrt{\left(\frac{L}{\sin(\theta)}\right)^2 - (L+x)^2}\right)^2 \tag{2.6}$$

and the total area is

$$A_{total} = \pi \cdot L^2 \tag{2.7}$$

where L and x are the vertical and horizontal displacement of the leaflets, respectively. When the left ventricle pressure (LVP) is higher than the AOP, these leaflets are moved through the aortic channel, resulting in the AV being open.

In order to obtain the opening angle, it is assumed that leaflets are closed when the leaflet angle is equal to $\gamma = 45^{\circ}$, which means that the heart valve can stretch in both forward and backward directions. Opening angle (θ) in degree can be obtained as:

$$\theta(x) = \cos^{-1}\left(\left(\frac{L+x}{L}\right)\sin(\gamma)\right) \tag{2.8}$$

Now, we have the geometrical interpretation of leaflet displacement based on the dynamic of mass-spring-damper in which leaflet displacements are changed with respect to the response of this dynamic. In order to calculate the hydraulic resistance of the AV, leaflet area can now be utilized by using both the effective area of the AV and displacement changes in leaflets since hydraulic resistance is a function of the effective orifice area and the pressure difference between LV and aorta.

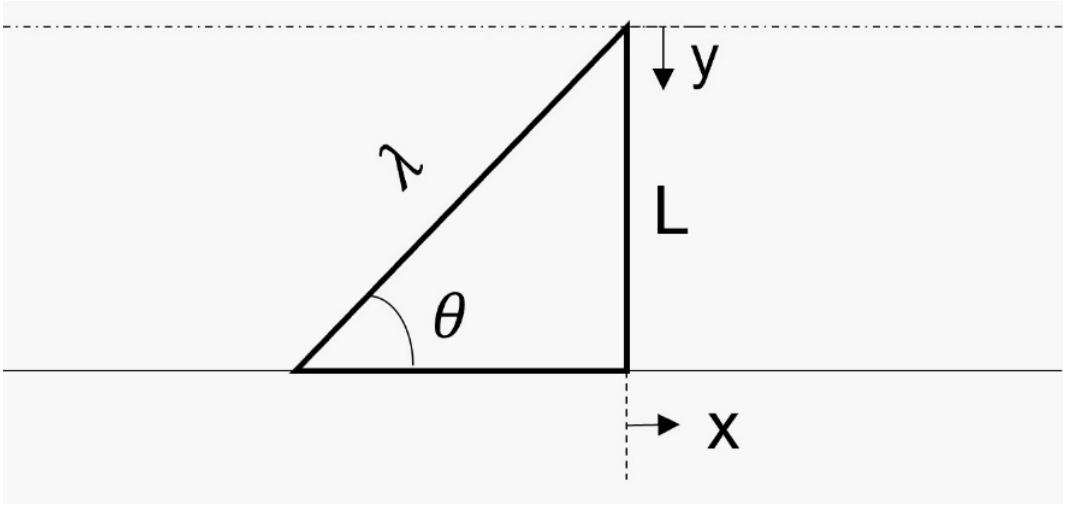


Figure 2.3 Simplified geometry of leaflets

2.3.2 Valve Blood Flow Resistance

In laminar flow, according to the fluid dynamics theory [41], the resistance equation can be stated as

$$R_{res}(x) = \frac{\Delta P}{Q_{lv}(t)} \tag{2.9}$$

where $Q_{lv}(t)$ is left ventricle flow rate, ΔP is pressure difference between LV and aorta. Using this equation, aortic flow can be given by

$$Q_{lv}(t) = \frac{P_{lv} - P_{ao}}{R_{res}(x)} \tag{2.10}$$

Now, the hydraulic resistance of the AV can be obtained from hydraulic losses in terms of major and minor losses. So, we need to involve the calculation of minor local losses given by [41].

$$\Delta P = K_l \frac{v_{lv}^2(t)}{2} \rho_{lv} \tag{2.11}$$

where K_l is the shape factor (unitless) which is equal to 1, v_{lv} represents the velocity of left ventricular fluid (m/sec) and ρ_{lv} is the density of blood ($kg/m\text{^}3$). Minor local losses are mainly caused by the expansion or narrowing of the pipe area, so in this case, it corresponds to the aim of the proposed design for the AV. (2.11) gives,

$$\frac{\Delta P}{Q_{lv}(t)} = R_{res}(x) = \frac{\Delta P}{v_{lv}(t)(\pi L^2)} = K_l \frac{v_{lv}(t) v_{lv}(t) \rho_{lv}}{2 v_{lv}(t) \pi L^2} \tag{2.12}$$

Then, we get the equivalent flow resistance as

$$R_{Res}(x) = K_l \frac{\rho_{lv}}{2\pi L^2} v_{lv}(t) \tag{2.13}$$

Hydraulic resistance of the pipe also contains major losses, which causes energy costs due to wall friction in the aorta. However, the leaflet structure only incorporates minor losses because of its open-close state. The reason is that the pathway exposed to friction is so small in the AV structure. Thus, we will continue with (2.13), representing the minor losses in the fluid dynamic characteristic of the aortic wall. Now, the left ventricular volumetric flow rate can be written on (2.14).

$$\dot{m}_{lv} = \rho_{blood} \cdot \dot{V}_{lv} \tag{2.14}$$

where $\dot{V}_{lv}$ is the volume flow rate of the fluid transferring LV to the aorta.

Reorganizing terms in (2.14), the flow rate can be rewritten in terms of the velocity of fluid such that

$$\rho_{blood} \cdot \dot{V}_{lv} = \rho_{blood} \cdot v_{lv} \cdot A_{orifice}(x) \tag{2.15}$$

Then, total resistance can be described combining (2.9) and (2.15) as:

$$R_{Res}(x) = K_l \frac{\rho_{blood} \dot{V}_{lv}}{A_{orifice}^2(x)} \tag{2.16}$$

and it is known as:

$$\dot{V}_{lv} = \frac{P_{lv} - P_{ao}}{R_{res}(x)} \tag{2.17}$$

The final expression related to aortic resistance can be given as following:

$$R_{Res}(x) = \sqrt{K_l \frac{\rho_{blood} \cdot |P_{lv}(t) - P_{ao}(t)|}{A^2_{orifice}(x)}} \tag{2.18}$$

In (18), the resistance can be described by the change in pressure balance and orifice area in the AV. So now, the leaflet dynamics can be included in this equation because of orifice area, which depends on leaflet displacement $x(t)$.

If substituting (2.3) and (2.18), then it becomes:

$$R_{Res}(x) = \sqrt{K_l \frac{\rho_{blood} \cdot |P_{lv}(t) - P_{ao}(t)|}{\left(\pi \cdot \left(L - \sqrt{\left(\frac{L}{\sin(\theta)}\right)^2 - (L+x)^2}\right)^2\right)^2}} \tag{2.19}$$

(2.19) gives the specific resistance led to the motion of leaflets as a function $x(t)$ and θ.

2.3.3 State Space Representation of Aortic Valve Dynamics

In order to combine the whole dynamics into one mathematical notation, state space representation form is built, including the mass-spring-damper-based leaflet and hydraulic pressure dynamics.

Let's assume that $z_1 = x$ and $z_2 = \dot{x}$, then

$$\frac{d}{dt}\begin{bmatrix} z_1 \\ z_2 \end{bmatrix} = \begin{bmatrix} 0 & 1 \\ -\frac{k(z_1,\theta,\alpha)}{m} & -\frac{c(z_2)}{m} \end{bmatrix}\begin{bmatrix} z_1 \\ z_2 \end{bmatrix} + \begin{bmatrix} 0 \\ \frac{1}{m} \end{bmatrix}\begin{bmatrix} 0 \\ \Delta F \end{bmatrix} \tag{2.20}$$

(2.20) gives the state space representation of leaflet dynamics and force balance related to the pressure difference at both sides of leaflets, as well. On the other hand, each pressure (left ventricular and aortic one) can be explained by lumped parameter model of the CVS including only three sections: LV, aorta, and venous given in Mulier's study [42]. Many studies concerning CVS modeling have been previously published [43]–[47]. Although beneficial results represent the pressure and flow characteristics of CVS in simulation, Mulier study is the best candidate to meet physiological criteria, especially in terms of pressure and flow [29]. The most

prominent model described in this study represents the main CVSs characteristics, including the hyper-activation and deactivation phase of the LV.

The specific problem addressed in the Mulier model is selected as the CVS, and its dynamics equations are improved with the aid of leaflet models. The leaflet model is extensively depicted in Figure 2.1 and Figure 2.2. The improved Mulier model can be given in Figure 2.4.

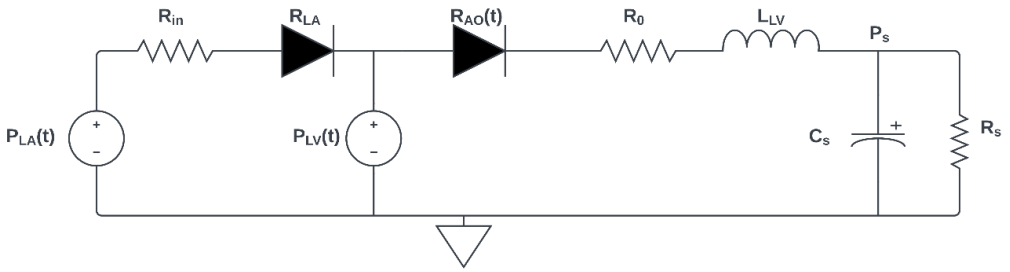


Figure 2.4 Improved Mulier model

In Figure 2.4, there are three chambers containing: the left atrium, LV, and systemic tank, respectively. Each of these sections represent its pressure value in terms of P_{la}, P_{lv} and P_s. The sections are indexing LAP, LV pressure, and systole pressure, respectively. AOP can be derived by using R_0 and $R_{ao}(t)$ resistance value with flow rate Q_{lv}.

Mathematical representations of these parameters are given in (2.21), (2.22) and (2.23).

$$Q_{la}(t) = \frac{P_{la} - P_{lv}}{R_{in}} \tag{2.21}$$

$$\frac{dQ_{lv}}{dt} = \frac{P_{lv} - P_s}{L_v} - \frac{R_0}{L_v} \cdot Q_{lv} - \frac{R_{ao}(x)}{L_v} \cdot Q_{lv} \tag{2.22}$$

$$\frac{dP_s}{dt} = \frac{Q_{lv}}{C_s} - \frac{P_s}{R_s C_s} \tag{2.23}$$

Flow rates sourced by the left atrium (venous return) and LV (aortic flow) are considered the primary feature to be investigated under changing valve resistance

due to open-close characteristics. In this study, time-varying resistances totally depend on the dynamics of the leaflet mechanism given in (2.19). Therefore, the proposed leaflet dynamics and improved Mulier model can be tested with a simulation program by adjusting parameters of spring, damping, and mass of leaflets with different values to represent both normal and abnormal conditions.

Table 2.1 Geometrical parameters of the heart model

Parameter	**Value**	**Units**
N_1	0.0007	mmHg/ml
N_2	2.75	ml
N_3	1.6	mmHg/ml
N_4	1	mmHg
τ_c	0.15	s
τ_r	0.175	s
t_p	0.3	s
Rs	0.08	mmHg.s/ml
R_{in}	0.001	mmHg.s/ml

In order to activate the CVS, the isovolumic ventricular pressure is driven by the elastance function. Table 2.1 shows CVS equation constants to emulate the physiological response of itself [29].

Time-varying elastance for the LV is represented with $g(t)$ function depending on the periodical time constants. To obtain this multiplication factor, the following equation set is used.

$$g(t) = \begin{cases} \left(1 - e^{-\left(\frac{t}{tc}\right)^{\beta}}\right) \ for\ 0 \le t \le t_b \\ \left(1 - e^{-\left(\frac{t}{tc}\right)^{\beta}}\right) e^{-\left(\frac{t-tb}{\tau r}\right)^{\beta}} \ for\ t_b < t < t_h \end{cases} \tag{2.24}$$

where τ_c is the time constant describing the contraction time, which is the pressure increase term, and τ_r indicates relaxation; therefore, the pressure decreases. As with the other parameters in this set, β is a metric for the overall pace of these procedures getting started. For the time interval of the function set, the constants t_h imply the heart period, and t_b is the time when the relaxation process begins to evolve, which is given in (2.25). It can be demonstrated as the following equation, with respect to t_p, which is the time duration of the peak generated pressure.

$$t_b = t_p \left\{ 1 - \left(\frac{\tau_r}{\tau_c}\right)^{\frac{\beta}{\beta-1}} \left(\frac{e^{-\left(\frac{t_p}{\tau_r}\right)^{\beta}}}{1 - e^{-\left(\frac{t_p}{\tau_c}\right)^{\beta}}} \right)^{\frac{1}{\beta-1}} \right\} \tag{2.25}$$

The stiffness parameter, (2.26), is derived by using the experimental data given [48]. Characterizing the radial form of the proposed leaflet model in terms of the opening angle (Θ) of the valve and radial area $A_{c,p}$ is proposed in order to improve the experimental data, α parameter is added to the model in which it is now adjustable in terms of condition of AV.

$$k(\theta, \alpha, x) = \frac{(\mathrm{v}_1 \cdot \Theta + \mathrm{v}_2) A_{c,p} \mathrm{v}_3}{\alpha} \tag{2.26}$$

In (2.26), coefficients of radial stiffness are obtained by using curve fitting in terms of $\mathrm{v}_1 = -4.2253, \mathrm{v}_2 = 235.323, \mathrm{v}_3 = 1000$. v_3 is only utilized to match the radial stiffness unit to N/m. α is utilized as an adjustable stiffness parameter which can be modeled in both normal and abnormal conditions when it is increased or decreased. $A_{c,p}$ represents the radial area of the leaflet section, which is given in (2.27).

$$A_{c,p} = \left(\frac{L}{\sin(\theta)}\right) \mathrm{v}_4 \tag{2.27}$$

where v_4 is the geometrical factor changing unit radial stiffness area with the value of 0.00001 [49]. Finally, the state space representation containing hydraulic and mechanical dynamics of the AV can be given as in (2.28).

$$\frac{d}{dt}\begin{bmatrix} x \\ \dot{x} \\ P_s \\ V_{lv} \end{bmatrix} = \begin{bmatrix} 0 & 1 & 0 & 0 \\ -\dfrac{k(x,\alpha,\theta)}{m} & -\dfrac{c(\dot{x})}{m} & 0 & 0 \\ 0 & 0 & -\left(\dfrac{1}{R_s C_s} + \dfrac{1}{C_s R_0}\right) & 0 \\ 0 & 0 & -\dfrac{1}{R_0} & 0 \end{bmatrix} \begin{bmatrix} x \\ \dot{x} \\ P_s \\ V_{lv} \end{bmatrix} + \begin{bmatrix} 0 & 0 & 0 \\ \dfrac{1}{m} & 0 & 0 \\ 0 & \dfrac{1}{C_s R_0} & 0 \\ 0 & \left(\dfrac{1}{R_0} - \dfrac{1}{R_{in}}\right) & \dfrac{1}{R_{in}} \end{bmatrix} \begin{bmatrix} \Delta F \\ P_{vt} \\ P_{la} \end{bmatrix} \tag{2.28}$$

where P_{vt} is the elastance-based pressure equation derived from the LVV like

$$P_{vt} = N_1(V_{lv} - N_2)^2 + (N_3 V_{lv} - N_4) f_t \tag{2.29}$$

with P_{la} is the LAP which is constant throughout this study. Here f_t is the activation level function that contracts and relaxes the heart muscle. This is obtained from the literature derived from g_t [29]. The related simulation results are given in the next section.

2.4 Experiments and Results

In the proposed approach, all experiments are conducted using the MATLAB SimulinkTM program to assess the effectiveness of the proposed method in comparison to physiological data obtained from existing literature. The experimental procedure consists of several steps. Firstly, the proposed leaflet dynamics are integrated into the enhanced Mulier model. Secondly, the aortic flow characteristics are analyzed by manipulating the spring and damping coefficients associated with the leaflets. Finally, the model is evaluated to determine its ability to replicate physiological conditions accurately. This comprehensive process is summarized in Figure 2.5, providing a visual overview of the entire experimental framework

The validation process comprises two main components. The first part involves acquiring the variables related to left ventricular pressure (LVP), aortic pressure (AOP), aortic flow, and the opening angle of the aortic valve (AV). These variables

are compared with physiological data obtained from existing literature. The second part involves assessing the disparity between the results generated by the proposed model and the physiological data. Additionally, a reference analog model is employed to evaluate the outcomes, allowing for a comprehensive evaluation of the proposed model's performance during the validation process.

.

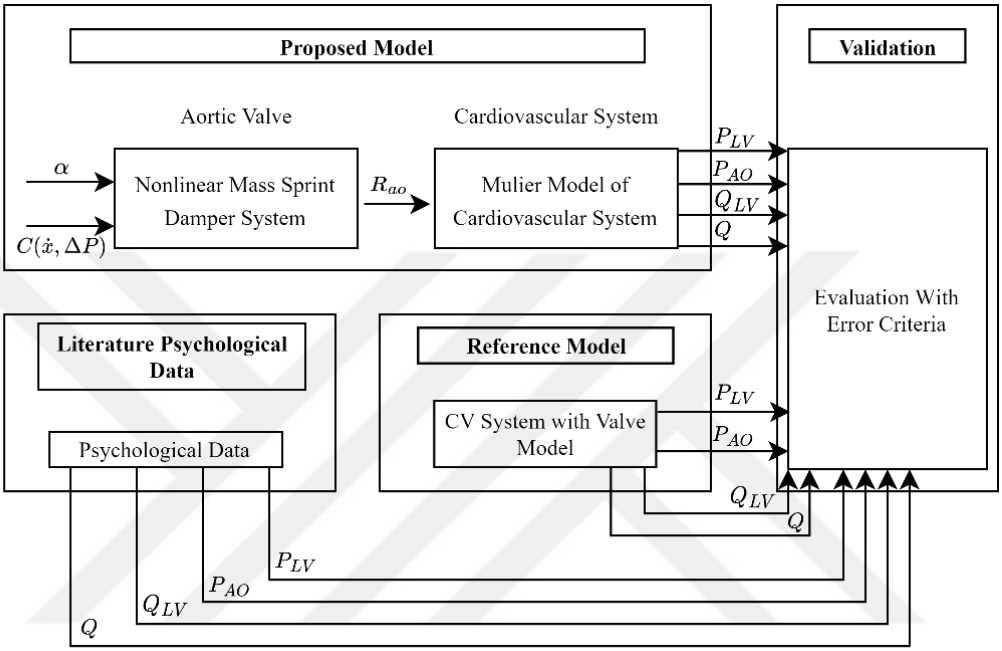


Figure 2.5 Validation process

2.4.1 The System Tests and Results

To assess the proposed model, variations in the spring coefficient and damping ratio of the leaflets are introduced. To determine the initial conditions of the opening angle $\alpha(0)$ and damping ratio $c(0)$, the nonlinear mass-spring-damper model is linearized at the nominal condition $\gamma = 45°, \theta = 45°, x = 0, \dot{x} = 0$ representing a closed AV.

Following the aforementioned procedure, the initial values of the spring and damping coefficients are determined through a nonlinear state-space estimation technique. The convergence of these coefficients is achieved by minimizing the error between the physiological output and the proposed model, specifically in terms of pressures, using the Simplex method [50]. The initial values are chosen for the spring and damping ratio as $\alpha(0) = 0.1$ and $c(0) = 2$, respectively. In the conducted tests, the α coefficient is varied within the range of 0.01 to 0.5, while the

c coefficient is varied within the range of 0.1 to 2. The initial results are illustrated in Figure 2.6.

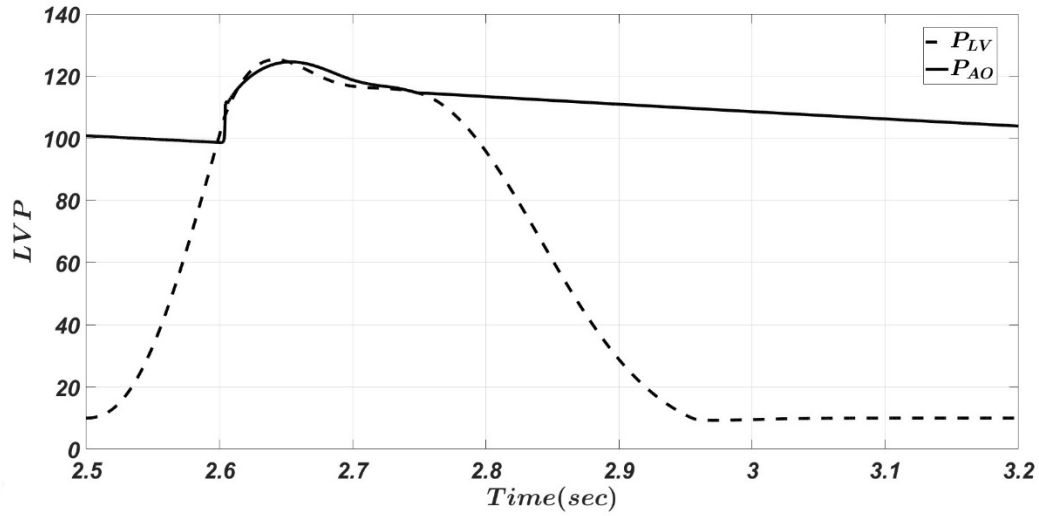


Figure 2.6 The LVP and AOP for **α** =0.1, **c**=2

The proposed model yields LVP values up to 140 mmHg, while the AOP remains within the range of 100 to 140 mmHg. This indicates that the time-varying resistance effectively emulates the opening/closing dynamics of the AV.

Subsequently, the system is simulated under different α values to investigate the impact of the spring coefficient on the recoil effect. For a constant damping ratio of $c = 0.1$, the following figure demonstrates the variations in AOP and LVP corresponding to different spring coefficients.

In Figure 2.7, it can be observed that increasing the spring factor coefficient leads to a rise in the overall pressure values. Furthermore, for smaller values of the coefficient, the presence of the dicrotic notch in the AOP becomes more pronounced and easier to detect. Similar trends are observed for the LVP values.

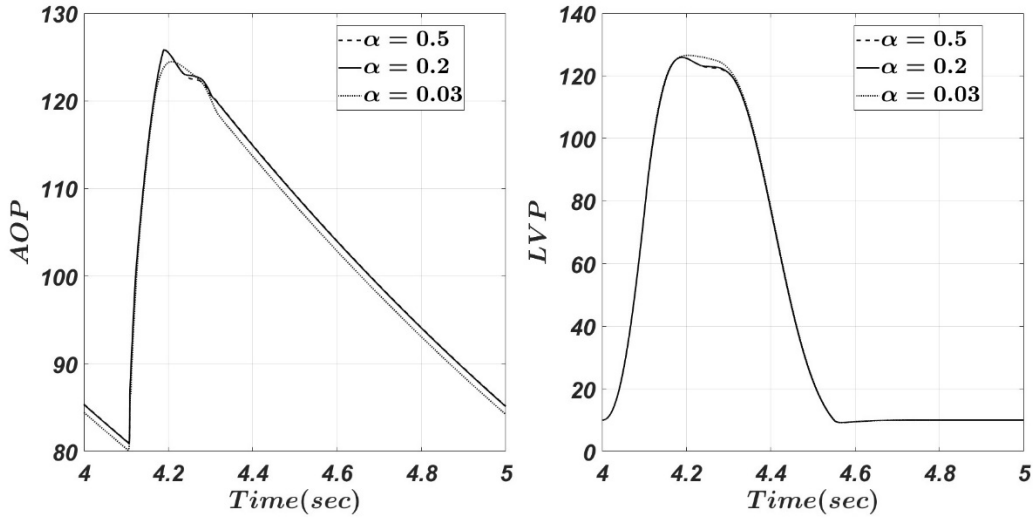


Figure 2.7 AOP and LVP variables for changing parameters

Moving forward, the assessment of aortic flow is performed during the simulation. During the systole phase, an active pressure drop between the inlet and outlet of the AV enables the flow of blood from the aorta to the systemic circulation. In this particular test, two scenarios are explored. Firstly, the damping ratio is held constant at $c = 0.1$ while the stiffness coefficient is varied. Secondly, the stiffness coefficient is kept constant while changing the damping ratio. The results are presented in Figure 2.8.

In Figure 2.8, it is evident that an increase in the α coefficient results in an elevated flow rate when the damping ratio (c) is held constant, as the spring factor (stiffness) decreases. Conversely, when the α coefficient decreases, the blood flow permitted across the valve decreases. Additionally, an increase in the damping ratio leads to a reduction in aortic flow, indicating a decrease in the backflow characteristic of the AV.

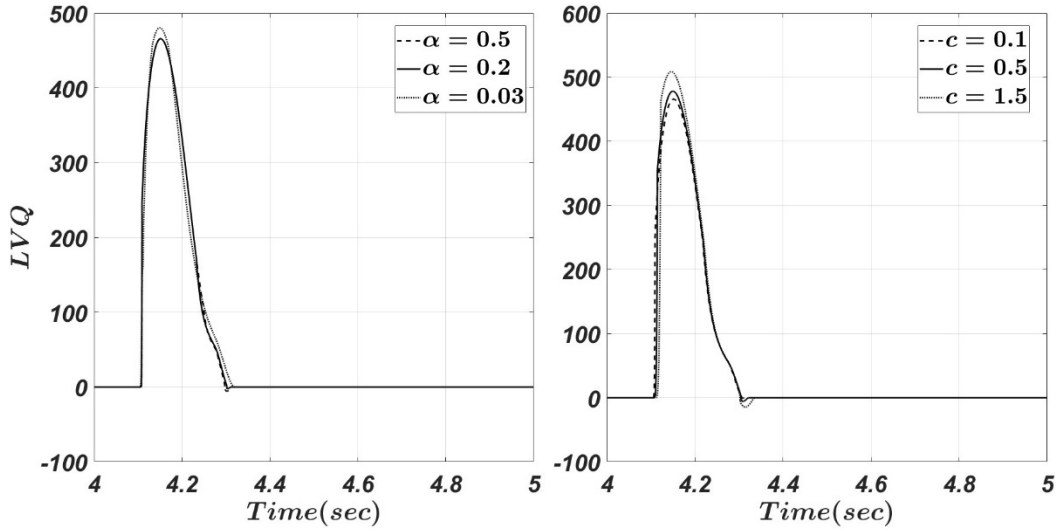


Figure 2.8. Blood flow rate (LVQ) for changing parameters

As mentioned previously, the occurrence of vortices is observed during the flow of blood from the LV to the systemic circulation. Particularly, in the sinuses of Valsalva, strong vortices are formed under steady or pulsatile flow conditions. [33]. These vortices persist throughout the systole in pulsatile flow, and the closure of the valve occurs gradually and uniformly. The formation of a vortex ring is observed at the exit of the valve during early systole. Therefore, the dynamics of the opening and closing phases of the valve leaflets significantly impact the sinus vortex vascular resistance and orifice area. A crucial aspect of achieving a successful AV model lies in accurately representing the opening and closing angle of the valve. The depiction of the modeled valve's opening angle for different radial stiffness values is presented in Figure 2.9.

In Figure 2.9, it can be observed that the aortic valve (AV) is considered closed when the opening angle is smaller than 45°, as per the design of the proposed model. This unique characteristic allows for the assessment of the back pressure effect on the AV when the aortic pressure (AOP) exceeds the left ventricular pressure

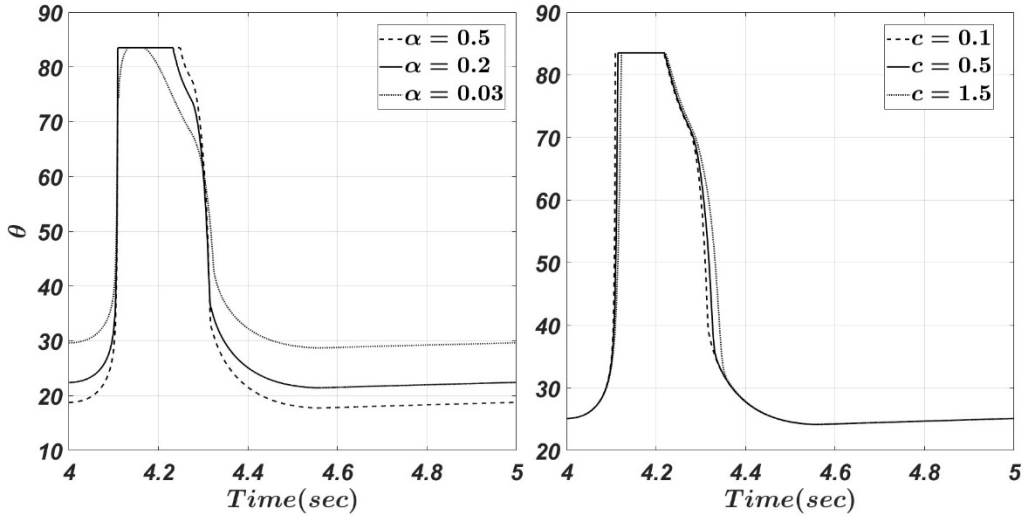


Figure 2.9. Opening angle variables for changing parameters

. The variability of the leaflets' spring parameter facilitates the evaluation of the AV's condition, encompassing both the open and closed states. In terms of physiological examination, the pattern depicted in the figure represents three distinct phases of the valve angle: fast opening, fully open plateau, and fast closing. These phases align with the physiological properties of the AV, providing further validation to the proposed model [50].

2.4.2 Pathophysiological Cases: The Aortic Valvular Stenosis and The Aortic Valve Regurgitation

The findings demonstrate that the proposed model effectively replicates both normal and abnormal conditions through its parameterization. To validate the system results, a comparison was made with a specific study by Korakianitis et al. [32]. In their study, they present a novel concentrated parameter model for cardiovascular (CV) dynamics, which incorporates a unique model of heart valve dynamics. This study explores variations observed in specific pathological cases. Figure 2.10 provides a visual comparison between the reference model and the proposed model. The simulations conducted in this study utilized the proposed model with $\alpha = 0.1$ and $c = 2$ as the configuration parameters.

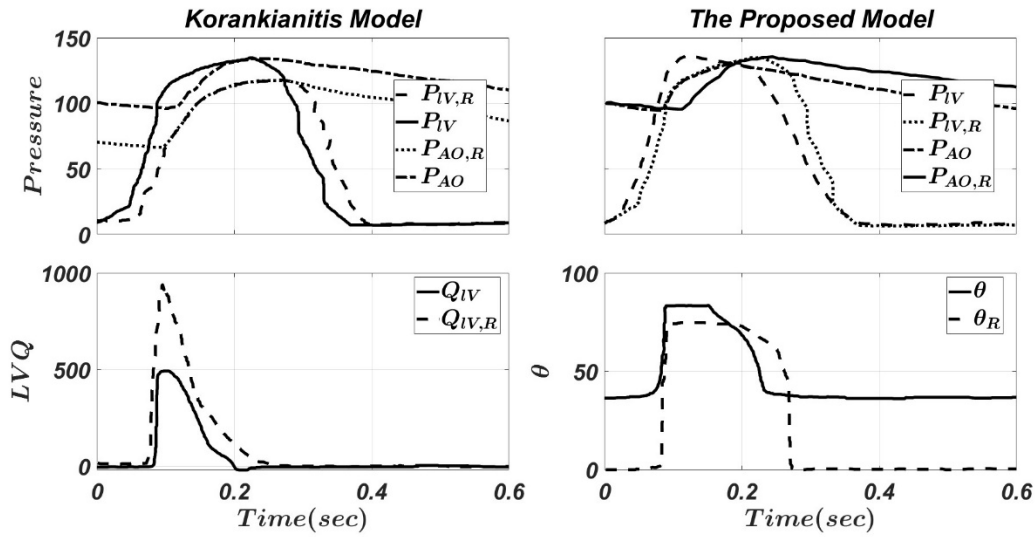


Figure 2.10. Comparisons of the reference model, the proposed model, and the physiological outcomes

One notable aspect of the Korakianitis model is the absence of direct correspondence between aortic and ventricular pressures. In contrast, the proposed model in this paper successfully captures the physiological constraints associated with this aspect. Additionally, the reference model exhibits excessively high CV LV flow values within the vortex case, surpassing realistic physiological limits. In contrast, the proposed model conforms to the expected pattern and maintains more realistic limits in terms of vortex formation and backflow occurrence. The last plot in the figure depicts the opening angle of the AV. A comparison of the opening angle outcomes reveals similar behavior between the two models, albeit with an approximate difference of 40 degrees. This discrepancy arises from the choice of starting angle. The reference model initiates with a leaflet-to-wall angle of zero, while the proposed model starts at 45 degrees to accurately represent the influence of back pressure on the heart valve.

2.4.3 Aortic Valvular Stenosis

The calcific deposits on the aortic side of the leaflets cause degenerative valvular AS characterized by stiff leaflets [51]. It is occurred in the case of the thickening of the valve walls [52]. This can be detected by the intracardiac pressure and volume flow rate deviations from its natural patterns [53]–[55]. Because of the stenosis, the pressure in the LV increases and becomes higher than in the aorta. As can be deduced, the valve's thickening plays a crucial role in modeling the disease. While

c=0.1, and the α value is 0.005, model output that overlaps with the disease value and has a low recoil effect parameter in Figure 2.11.

The incomplete opening of the AV, which leads to an increase in aortic resistance, causes AS (afterload). During the ejection, the left ventricular pressure rises abnormally due to the increased aortic resistance.

2.4.4 Aortic Regurgitation

Aortic valve insufficiency (aortic regurgitation) is a condition that is observed when the AV cannot close tightly. As a result, some of the blood pumped out of the main pumping chamber (left ventricle) leaks backwards [56]. In the pathophysiological AV with aortic regurgitation, the AOP drops faster due to the backflow, as a result the systolic pressure increases to maintain the normal mean pressure; therefore, an increased pressure amplitude is observed [57]. When the α value is 0.001 and the c value is 2, the dramatic decrease in the flow rate of the blood leaving the LV can be modeled as it has been shown in Figure 2.12.

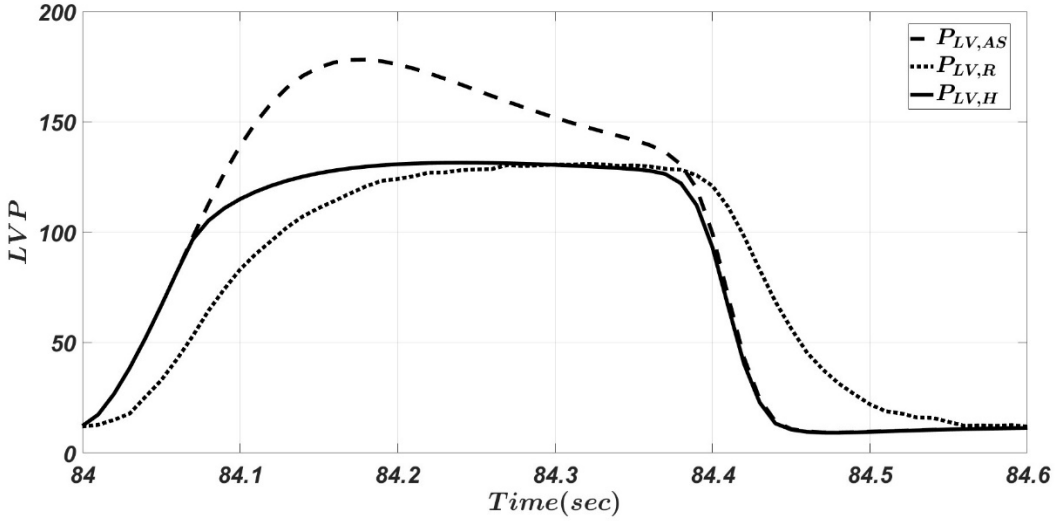


Figure 2.11. Comparison of the LVP under AS and healthy conditions

Figure 2.12 presents the effect of regurgitation, indicated by RGT, on the heart valve. In the first panel of the figure, a decrease in the AOP is observed under the pathophysiological regurgitation condition. The second panel shows a reduction in LVP. This decrease in LVP is attributed to the hindrance caused by regurgitation, which counteracts the forward blood flow during the ejection phase and leads to an increase in left ventricular pressure. Additionally, the opening angle of the AV is impeded by the opposing tissue wall, resulting in a reduction in the opening angle,

as shown in the third panel. Finally, the fourth panel demonstrates a significant decrease in blood flow rate compared to the healthy condition, indicating the adverse impact of regurgitation on the overall blood flow dynamics.

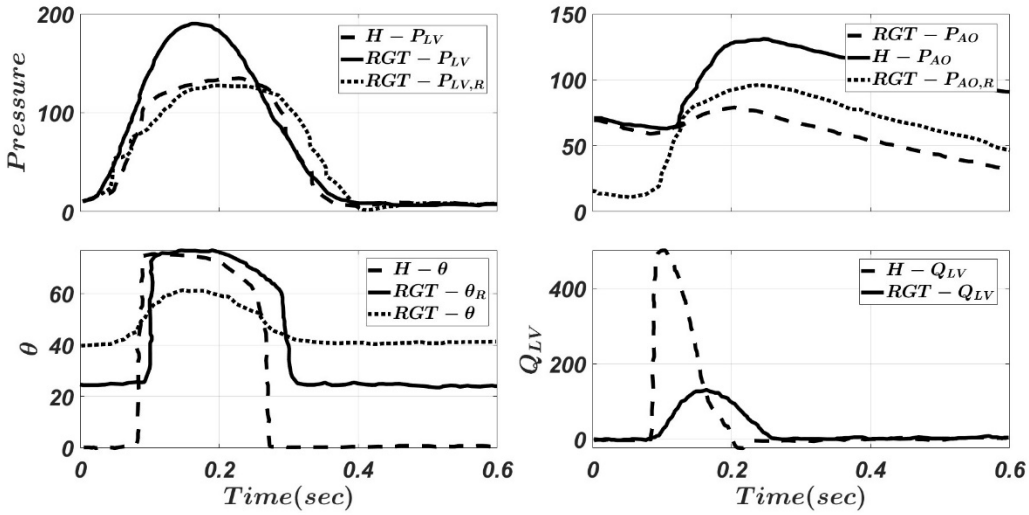


Figure 2.12. Comparisons of the physiological parameters under AV regurgitation and healthy conditions

2.5 Discussion and Conclusion

This study introduces a model for the AV leaflets based on a nonlinear spring-damper-mass analogy. By leveraging the displacement of the mass-spring-damper system, a time-varying aortic resistance is incorporated into the model.

Initially, a healthy physiological condition for the cardiovascular system (CVS) is established by setting α=0.1 and c=2 using the linearization method under specific initial conditions. It should be noted that selecting different initial conditions may not yield the desired physiological response of the AV. To address this issue, the spring and damping ratio values are estimated based on physiological data of LVP and AOP obtained from literature data. The simplex method is employed to converge on the correct initial values within the proposed model. The results demonstrate that decreasing α leads to increased LVP and AOP. Additionally, a smaller α value allows for a clearer detection of the dicrotic notch, which aligns with physiological conditions.

Subsequently, the findings reveal that decreasing α or increasing c results in a decrease in aortic flow. In both cases, LV pressure increases while the occurrence of backflow through the AV decreases. It is worth noting that an inadequate aortic

flow rate can impede the fulfillment of the Frank-Starling law, even if other physiological variables remain within the expected range of limits [58].

In the third step, the initial opening angle of the aortic valve (AV) is set to 45° to account for the influence of reverse pressure exerted by aortic pressure (AOP) during the diastolic phase. This novel addition allows for the assessment of the AV when it is completely closed and exposed to reverse pressure, which has not been previously considered in the literature. With the proposed method, it becomes possible to examine the behavior of the AV leaflets under high-pressure conditions even during the diastolic phase. Furthermore, a single time-varying continuous resistance can now be employed for both the diastolic and systolic phases. Moreover, the proposed model successfully captures the physiological states of AV opening angles during the fast opening, plateau, and fast closing phases.

In the fourth step, a comparison is made between the results obtained from the proposed model, a reference model, and physiological data from a previous study [32]. It is evident that the previous study exhibited smaller ventricular and AOP values, as well as flow rates, compared to the physiological range. In contrast, the proposed model aligns with the physiological conditions by generating ventricular and AOP values within the appropriate range. Notably, in the examination of flow rates, the study by Korakianitis et al. presented flow rates that exceeded physiological limits. In contrast, our proposed model produces flow rates within the physiological range, accurately capturing the backflow characteristics observed in physiological conditions.

In terms of abnormal conditions, such as AS and regurgitation, the proposed model allows for their simulation. For AS, a damping ratio (c) of 0.1 and a spring ratio (α) of 0.005 are chosen, indicating a decrease in damping ratio and an increase in spring ratio compared to the healthy condition. On the other hand, aortic regurgitation is emulated by selecting $c=2$ and $\alpha=0.001$. In this case, even if the damping ratio is kept constant, the flow rate is significantly decreased. Additionally, the left ventricular pressure is increased, which is consistent with the physiological condition, unlike the reference model [32] that did not capture this feature. Consequently, for both AS and regurgitation, the spring ratio needs to be increased, with a greater emphasis on the change in spring ratio for regurgitation rather than the damping ratio.

Table 2.2 Comparison of the proposed model with other works

CONDITION	P_{lv} *(mmHg)*	P_{ao} *(mmHg)*	Q_{lv}*(ml/sec)*
Our Healthy Case ($\alpha = 0.1, c = 2$)	20 - 140	90 - 130	0 – 600
Our Stenosis Case ($\alpha = 0.005, c = 0.1$)	20 - 180	80 - 140	0 – 400
Our Regurgitation Case ($\alpha = 0.001, c = 2$)	20 – 130	60 – 110	0 – 100
Korakianitis et.al. Model Regurgitation [32]	20 – 200	100 – 140	0 – 250
Laubsher et. Al. Healthy [34]	15 - 130	80 – 120	0 – 500
Laubsher et. Al. Severe Stenosis [36]	15 – 180	100 – 150	0 – 300

Another notable advantage of the proposed method is its ability to examine the occurrence of eddy flows in the sinuses, which may arise due to the variable opening speeds of the valve. Furthermore, the proposed model successfully mimics the spring-back movement of the valves in response to blood flow. To evaluate the performance of the model in terms of the selection of α and c, Table 2.2 illustrates the healthy and unhealthy conditions of the AV.

In Table 2.2, the physiological properties of the CVS are given in terms of P_{lv}, P_{ao} and Q_{lv} with the changes of α and c coefficients. The findings clearly demonstrate that AS can be effectively modeled by reducing both the spring ratio (α) and damping ratio (c). Conversely, aortic regurgitation can be successfully emulated by maintaining a constant damping ratio while further reducing the spring ratio, compared to the stenosis case. The proposed model shows similar changes in LVP and AOP to the existing models for both AS and regurgitation, except for the flow rates in aortic regurgitation [32], [34]–[36]. Specifically, the proposed model produces a reduced flow rate in aortic regurgitation, aligning with the physiological expectations presented in the works of Korakianitis et al. Moreover, the results obtained for AS in the proposed model are consistent with the findings reported in the referenced studies.

In this study, a unique heart valve model based on the nonlinear mass-spring-damper analogy to replicate physiological nature of time-varying resistance has been proposed. In order to set different conditions in AV, spring coefficient and damping ratio are changed by adjusting α and c values, respectively. The system has been validated in terms of AOP, left ventricular pressure, blood flow rate through LV to AV and opening angle of the valve. Finally, the system model has been used for emulating two pathophysiological cases such as AS and aorta regurgitation. By changing the state space parameters, the main indicators of such diseases could be shown clearly.

The results clearly showed that CV responses can be emulated under healthy, AS, and aortic regurgitation conditions. In addition, reverse pressure effect on aortic leaflets is observed with the aid of the proposed model. The physiological data and reference models are also assessed to validate the outcomes in terms of left ventricular and AOP, opening-closing angles and aortic flow rates. In the further studies, the real-time estimation of aortic resistance based on the proposed model and neural network will be studied to obtain more realistic physiological response. Besides, time-varying α and c coefficient will also be performed for the adaption on CVPs under changing SVR.

3
A NEW CARDIOVASCULAR MOCK LOOP DRIVEN BY ACTIVE CAPACITANCE IN NORMAL AND ABNORMAL CONDITIONS

3.1 Abstract

This paper presents a novel design and control approach for a hMCL used in hemodynamic simulations of critical CVDs. The stability proofs of the closed-loop hMCL demonstrate its ability to drive proportional valves using a discrete feedback linearization rule. Our study introduces a new LV volume-elastance equation that combines the autoregulation of the FSM with the contractility of the LV. In contrast to conventional approaches, the hMCL is primarily driven by the volume of the left ventricular gas chamber, while ensuring that other parameters align with human data. Notably, no prior functions or data are utilized to create the reference signal, except for the maximum and minimum values of LVV. Consequently, the maximum elastance of the LV (Emax) is not required to generate left ventricular pressure. To assess the performance of the hMCL, we obtained CVP from human data and conducted simulations and experiments to investigate scenarios such as AS, changes in SVR, and variations in heart rate. Through our hMCL, we demonstrate that increasing heart rate leads to enhanced left ventricular contractility while maintaining consistent physiological pressures. However, this increase in left ventricular contractility is accompanied by a decrease in LVV, supporting the findings from human data. Furthermore, our hMCL reveals that AS causes an increase in both left ventricular and AOPs. On the other hand, when SVR changes, it preserves the left ventricular pressure while elevating the AOP. It is important to highlight that the proposed hMCL offers high flexibility and reproducibility, enabling the testing of a wide spectrum of CV conditions.

3.2 Introduction

The CVS is the whole circulatory system for pumping blood across the body to sustain the gas and nutrients exchange through the tissues and cells [59]. Any dysfunction during the entire process is named CVD. CVDs are a major public

health concern, In Europe alone with a reported that 85 million people affected and 3.9 million deaths in 2015. CVDs are responsible for 45% of all deaths in Europe. This highlights the importance of research and efforts to prevent and treat CVDs in the region [60]. According to the WHO, CVDs are the leading cause of death globally. In 2019, approximately 17.9 million people died due to CVDs [21]. This emphasizes the ongoing need for research, prevention, and treatment efforts to address the global burden of CVDs. Therefore, modeling, diagnosis and curing of the CVDs have been one of the primary important research fields for medical and engineering applications nowadays.

The CVS tests can almost be conducted in vivo or in vitro. In vivo tests are performed within a living organism and provide realistic results, but they are restricted by regulatory foundations and can be difficult to repeat. In contrast, in vitro tests are performed outside of a living organism and offer greater control and reproducibility. Additionally, since the CVS can be affected by spurious effects, modeling and simulating them can be challenging. Therefore, in vitro tests and equipment have become increasingly important in CV research. Although in vivo examinations are giving high precision in terms of the results and physiological data match due to the fact that they are deal with the real time living organism responses, their process are generally high-restricted by the regulator foundations and institutions such as FDA and NCBI, etc [61], [62]. Besides, the repetition of the in vivo tests is challenging; testing different conditions is almost impossible or become high time consumed processes. However, when conducting experiments, in-vitro testing offers a superior level of control over the working environment than animal testing. Specifically for the CVS, hydraulic components are affected by spurious effects, making it impossible for hydraulic components to imitate mathematical models of the system. So, for the sake of the reproducibility and the studying different conditions, in vitro tests and equipment become prominent.

To assist the CVS in cases of partial or complete dysfunction, especially pertaining to the heart, various types of devices are available. These include FDA-approved equipment such as artificial heart valves, stents, and ventricular assisted devices [63]. Hybrid mock circulatory (hMCL) loop systems are commonly utilized for in vitro testing of blood circulation systems and validation processes for these devices [64]. These systems range in complexity, from simple pulse duplicators to

feedback-controlled systems that integrate the contractile activity of the heart [65]–[67]. The hMCL combine device and numerical circulatory models to enhance system flexibility and accuracy. Additionally, the FSM depicts the interaction between CV assist devices and the CVS. However, the hMCL lacking preload and afterload response fail to yield physiological results. Early researchers utilized the Suga et al. time-varying elastance model to incorporate the FSM, which remains frequently employed in the design of such hMCLs [68]. The time-varying elastance model of Suga et al. remains widely used for driving the heart contraction mechanism in mock loops. Therefore, the study by Suga et al. based on the elastance model within the LV continues to serve as a common reference for constructing these loop systems [69].

Various approaches have been proposed in the literature for the hMCL, with reference to the FSM [70]–[72]. It is indeed possible to assess ventricular systole using these approaches [73]. The elastance-based controller responds to changes in preload, afterload, and contractility in a manner similar to the normal heart, as demonstrated through simulations and tests conducted using MCL components. However, the maximum elastance value, which represents the ventricular contractility capability, remains constant. The utilization of elastance-based control in such loops has emerged as one of the most optimal approaches, as the elastance function is a time-dependent arbitrary function that allows for modifications in ventricular chamber contractility [74]. Furthermore, several studies have been reported in the literature on controlling elastance-based mock loops [74]–[79]. These studies employed the elastance function to derive pressure-volume diagrams for cardiac energetics. However, the elastance function solely generates the total LVP, without distinguishing between the passive and active contributions. This differentiation is crucial for capturing the realistic physiological features of the CVS. The contraction process of the LV involves the excitation of muscles in the active part only, and this aspect should be considered significant.

There have been numerous studies reported in the literature on the hMCL used to evaluate the properties of the CVS under different normal and abnormal conditions. Ferrari et al. investigated pathophysiological conditions by modifying E_{max} and E_{min} [65]. They generated reference left ventricle flow rate (LVQ) and LVP in software to drive the hMCL [75]. However, there was inconsistency with physiological data

in terms of arterial pressure drop. In their subsequent improvement, they incorporated a compliance formulation based on Young's modulus [80]. Although they achieved good results that matched physiological data, they did not assess the wave propagation of LVQ using this model. Colacino et al. enhanced the elastance model by incorporating the viscoelastic properties of ventricular tissue, as well as the inertial effects of walls and intraventricular blood [76]. They used LVV as a reference signal to implement the FSM with their controller technique. They extensively tested and validated preload, afterload, and the FSM using human data from Guyton's study. However, their controller design did not include ventricular contractility to fully satisfy both the autoregulation of the FSM and ventricular contractility. Additionally, they used a gear pump to supply appropriate LVV, but the mathematical stability of the controller structure was not proven. Gregory et al. designed mock circulation loops that replicated the left and right Frank-Starling responses and tested changes in preload using a controller that applied pressure references to a pneumatic actuator [81]. However, they did not demonstrate the stability of driving pneumatic actuators, and the utilization of the LVP reference did not entirely reflect the time response of the autoregulation of the FSM. Janse-Park et al. achieved preload sensitivity, regulation of SV with mean arterial pressure, and baroreflex mechanisms by varying ventricular contractility using E_{max} [82]. They did not define the FSM based on time-varying elastance but instead utilized an adaptive control approach without guaranteeing stability. Furthermore, the direct supply of LVQ using a gear pump was inconsistent with the physiological properties of the CVS. Mirzaei et al. developed a convergence technique to simulate stenosis in the CVS [83]. Although their results were promising, the convergence process did not allow for real-time control and application. Gregory et al. constructed systemic, pulmonary, cerebral, and coronary circulation with autoregulation responses by validating human data [84]. They introduced pneumatic control with the FSM responses of the ventricles, but stability was not guaranteed. However, repeatability was problematic for validating their results due to the absence of controlled dynamics. Salesch et al. developed a closed-circuit hMCL to replicate the physiological behavior of the CVS [85]. They controlled both aortic and left ventricular pressures but did not guarantee stability. They were the first to define the ESPVR and EDPVR of the LV to drive the system, especially for parameter estimation of the CVS. Vignali et al. included the aortic complex

using a 3D printed hMCL that simulated both aortic and mitral flows [86]. The aortic flow waveform was used as an input, and supra-aortic vessel flow was accurately represented based on the literature. However, compliance control was lacking in the chambers, and the LVP profile was used to drive the hMCL. The entire system was controlled, and there were no free parameters to describe the passivity of the CVS. Linear approximation of left ventricular elasticity was used to emulate the time responses of the CVS, and nonlinear approximation was performed to improve this feature [68]. However, the relationship between elasticity and volume had not been studied to satisfy both the autoregulation of the FSM and the physiological pressure range in the left ventricular section. Rocchi et al. reviewed personalized MCL designs to provide physiological properties of the heart, especially in 3D models [87] . They designed heart valves to represent aortic flow and pressure characteristics, but they did not incorporate the coupling of the contractility feature of the LV to provide the FSM. Furthermore, the stiffness of the left ventricular chamber was a vital key parameter for replicating more consistent results that matched physiological human data. Rapp et al. constructed an hMCL to simulate valvular stenosis and cardiac arrhythmia using a ventricular assisted device [88]. However, the inputs of the system, such as LVP, ventricle assisted device flow rate, and right atrium pressure, were not physiologically correct for the passive parameters. Packy et al. developed MCL to characterize normovolemia, cardiogenic shock, and hyperdynamic circulation [89]. Although the results were consistent with human data, the left ventricular viscoelastic behavior and other tanks were manually controlled by using a syringe to set the proper compliance value, which posed difficulties in real-time application. Bardi et al. proposed a hMCL to simulate hemodynamics in terms of 3D geometry and inlet/outlet conditions [90]. However, the tank pressures were controlled, and compliance and resistance values needed to be set when the system was closed rather than during operation. Additionally, a stability rule was not provided for the gas valve to control the pressure values of the chambers.

Furthermore, it is crucial to incorporate gas modeling in the hMCL to capture the electrical and mechanical feature of the elastance resulting from the electrical activation of the heart and the filling of blood into the LV. Vandenberghe et al. conducted a study highlighting that the intricate hemodynamic behavior of a

mechanically assisted LV cannot be adequately captured by the time-varying elastance theory alone. Therefore, the development of a new ventricular model is necessary to accurately represent the interaction between the heart and the assisting device [91]. Therefore, there is a prominent need for a novel approach to the design of such systems, particularly emphasizing the compression and expansion of system components to accurately replicate isovolumic relaxation and contraction. Although the utilization of maximum elastance value in models is not widely explored in the literature, it presents a promising avenue for achieving convergence within physiological limits and satisfying natural ranges during in vitro testing. The novelty of this propsed method lies in the incorporation of capacitance and volume control equations to simulate the gas tank dynamics, forming the foundation of the proposed system. In this study, a new design and control strategy for a hMCL are proposed. A novel volume-elastance equation is derived to mimic the FSM, aligning with physiological human data. Importantly, for the first time, left ventricular elastance is considered time-varying and obtained from the gas chamber, representing the active component of the left ventricular muscle. Additionally, a discrete feedback linearization controller is designed to ensure stability in the gas valves, which serve as the sole inputs to our proposed system. Furthermore, the pathological conditions are simulated by manipulating aortic and systemic resistance values and validated using human data and reference models. Various heart rates and their associated COs are demonstrated to verify the functionality of the FSM.

3.3 Material and Methods

In this section, we provide a comprehensive overview of the proposed hybrid mock loop. Firstly, we will present a general description of the system. Next, we will develop the state-space representation of the entire dynamics and provide a detailed derivation of the volume-elastance relationship. To ensure stability, we will establish a discrete feedback linearization control approach for the gas valve.

3.3.1 Proposed Hybrid Mock Circulatory Loop

The hMCL serves as a hydraulic test bench that facilitates the analysis of prosthetic functionality, design, and their interactions with the simulated CVS [69]. The key components of the CVS, including the LV, left atrium (LA), and aorta, are

represented by physical tanks comprising both gas and liquid components. While the complete CVS consists of various compartments such as arteries, right ventricle, atrium, and capillaries, for specific CVS tests, a simplified geometry is employed, focusing on the essential compartments. In the proposed design of the hMCL, the LA, LV, and aorta compartments are modeled using physical tanks, as illustrated in Figure 3.1.

Figure 3.1 illustrates the complete configuration of the hMCL, comprising the LV, aorta, and LA tanks, with the liquid components depicted in blue. The LV tank is equipped with two distinct liquid valves: the mitral valve, responsible for transferring the liquid from the LA to the LV during the diastole phase, and the AV, facilitating flow from the LV to the aorta tank during the systole phase. The construction of the entire platform involves three pipelines that connect each tank to specific adjustable resistances referred to as R_M, R_A and R_V . These resistances can be modified by increasing or decreasing their values to replicate pathophysiological scenarios in the hMCL.

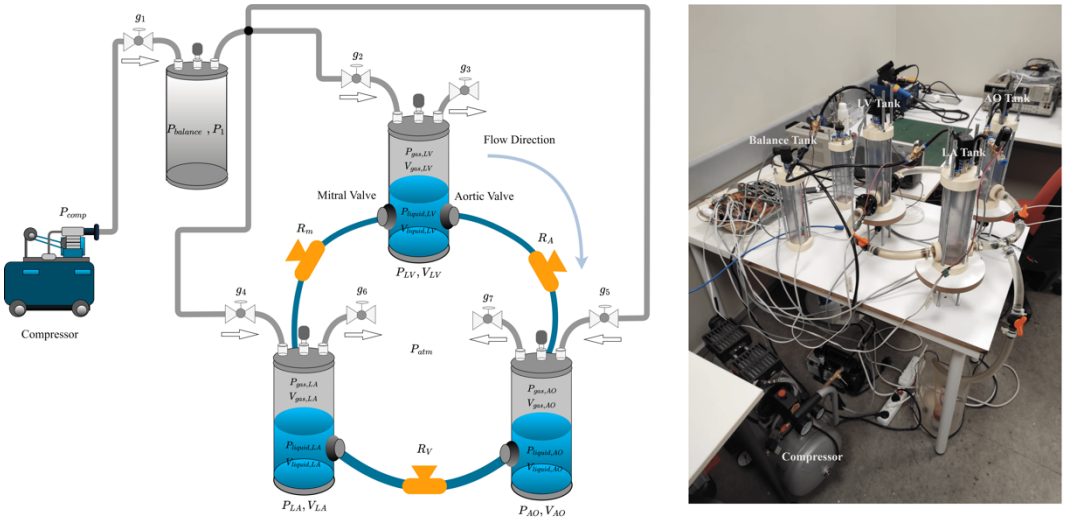


Figure 3.1. Mechanical structure of mock loop design

To account for the naturally low-pressure characteristics of the LV chamber, a balance tank ($Tank_1$) is employed to reduce the supplied gas pressure. Within the pipeline, a valve is included to decrease the pressure, as it is more convenient to apply control mechanisms at lower pressure levels. The hMCL incorporates proportional gas valves to regulate gas inlet and outlet, and these valves are

controlled by adjusting the electrical current based on the pressure difference balance between interconnected tanks.

To regulate the gas inlet and outlet, proportional gas valves have been incorporated into the hMCL system. These valves can be controlled by adjusting the electrical current in response to the pressure difference balance between interconnected tanks. The system consists of three valves: g_1, which is situated between the compressor and $Tank_1$; g_2, located between $Tank_1$ and the LV gas section; and g_3, which connects the LV gas section to the atmosphere.

In order to explain the whole processes, the functional block diagram is illustrated in Figure 3.2.

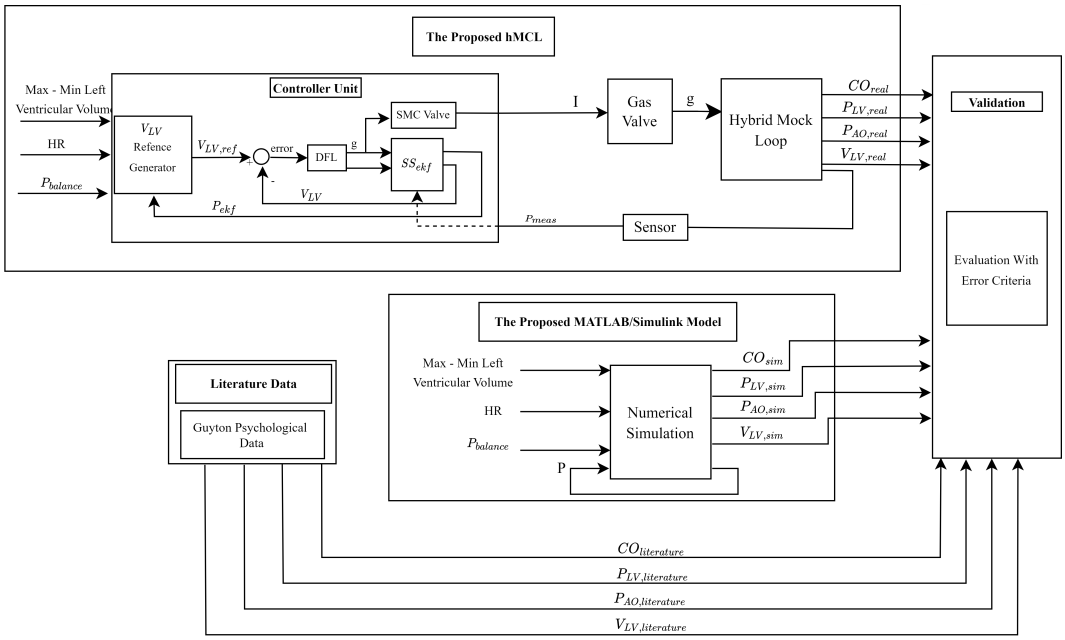


Figure 3.2. Functional block diagram of the proposed system

Figure 3.2 describes both the numerical and hMCL functional diagrams, illustrating the implementation of physical and numerical processes. The reference signals chosen for the system are heart rate and the maximum and minimum values of LVV. The hMCL and numerical simulations generate outputs such as CO, LVV, LVP (P_{lv}), and AOP (P_{ao}). Furthermore, physiological human data from the literature is used to validate the performance of the proposed hMCL. In the hMCL, the control algorithm is implemented on an STM32F746 microprocessor, incorporating both the system's dynamic representation of the numerical model and the discrete feedback linearization algorithm. To supress the measurement noise, an Extended

Kalman Filter (EKF) is employed in the controller unit, as described in the subsection of Figure 3.2. The driving current is calculated using the SMC valve flow-current pressure diagram, which converts the controller input (opening rate, g) into the appropriate current value.

In the controller design, the error is computed by subtracting the generated LVV reference from the measured one. This error value is then fed into the discrete feedback linearization equation to obtain the controller input. Additionally, an EKF is established by linearizing the total state-space representation. Noisy pressure measurements are inputted into this filter, and the filtered pressure values are used to calculate the appropriate controller input.

3.3.2 System Dynamic Representation

In this section, we establish the dynamic representation of the current hMCL system by deriving the equations of motion. These equations include the conservation of mass rule and the capacitance equation. Furthermore, we provide a comprehensive list of symbols related to the equations in Table 3.1.

3.3.2.1 Modeling of the hMCL

The mock loop representing the dynamics of the left ventricular of the CV loop consists of three tanks, LV, LA, and AO for the fluid motion and the balance tank to produce the required pressures as depicted in Figure 3.1. In order to account for variable capacitance, the dynamics of each tank need to be derived based on the inlet and outlet flows. The dynamics are expressed in compliance form, incorporating the mass rule for both gas and liquid flows. Additionally, the conversion of gas density into pressure is achieved by applying the Ideal Gas law to each tank.

Table 3.1 Symbols table

Parameter	*Name*	*Value*	*Unit*
$\boldsymbol{P_i}$	Total pressure for "i" tank		***mmHg***
$\boldsymbol{P_{i,g}}$	Gas Pressure for "i" tank		***mmHg***
$\boldsymbol{\Delta P_{i_{in}}}$	Inlet Pressure Difference		***mmHg***
$\boldsymbol{\Delta P_{i_{out}}}$	Outlet Pressure Difference		***mmHg***

Table 3.1 Symbols table (continued)

P_c	Compressor Pressure		***mmHg***
P_{atm}	Atmospheric Pressure		***mmHg***
$V_{i,l}$	Liquid Volume for "i" Tank		***ml***
$V_{i,g}$	Gas Volume for "i" Tank		***ml***
V_T	Tank Total Volume		***ml***
$m_{i,st}$	Tank Mass Storage for "i" tank		***kg***
$m_{i,g}$	Gas Mass for "i" tank		***kg***
m_i	Transferred Mass Between "i" and "i+1" tank		***kg***
ρ_i	Gas density for "i" tank		***kg/ml***
ρ_l	Liquid density for blood		***kg/ml***
$C_{i,g}(t)$	Gas Compliance Parameter for "i" tank		***kg/mmHg***
$C_g(t)$	Control Collective Compliance Parameter		***kg/mmHg***
$\alpha_i = 1 / C_i$	Elastance for "i" tank		***mmHg/kg***
g_i	Valve Conductance between "i" and "i+1" tank		***kg/(mmHg. sec)***
$A_{e,LV}$	Control Coefficient for Left Ventricular Volume		**-**
$A_{e,P1}$	Control Coefficient for Tank1 Pressure		**-**
R	Ideal Gas Constant		***(mmHg.ml)/ (kg.K)***
T	Temperature	**273+23**	***K***
D	Pipeline Diameter	**0.014**	***m***
L	Pipeline Length	**0.35**	***m***
μ	Liquid Viscosity	**$1.0016*10^{-3}$**	
A	Tank Area	**0.0020**	m^2
G	Gravity	**9.81**	m/sec^2
$g_M = \frac{128\,\mu\,L}{\pi\,\rho\,D^4}$	Physical Mitral Conductance Rate	**0.00027**	***m.sec***
$g_P = \frac{128\,\mu\,L}{\pi\,\rho\,D^4}$	Pipeline Conductance Rate	**0.00027**	***m.sec***

Table 3.1 Symbols table (continued)

$g_{AO} = \frac{128\,\mu\,L}{\pi\,\rho\,D^4}$	Physical Aortic Conductance Rate	**0.00027**	***m.sec***
$g_{SYS} = \frac{128\,\mu\,L}{\pi\,\rho\,D^4}$	Physical Systemic Conductance Rate	**0.00027**	***m.sec***
g_{ao}	Physical Aortic Valve Conductance Rate	**$0.1504*10^{-4}$**	***m.sec***
g_m	Physical Mitral Valve Conductance Rate	**$0.2506*10^{-4}$**	***m.sec***
$\theta_1(t)$	Time-varying Mitral Opening Rate	**-**	-
$\theta_2(t)$	Time-varying Aortic Opening Rate	**-**	-
$g_{TLI}(t) = [g_m + g_M + g_P]\theta_1(t)$	Generalized Input Conductance Rate	**-**	***m.sec***
$g_{TLO}(t) = [g_{ao} + g_{AO} + g_P]\theta_2(t)$	Generalized Output Conductance Rate	-	***m.sec***

The LV, aorta, and LA tanks are modeled considering the gas-liquid interaction and conservation of mass law, whereas the $Tank_1$ represents only the gas component of this dynamic system. The general conservation of the total mass in a tank is given as

$$\dot{m}_{st,i} = \dot{m}_{i_{gas\,in}} - \dot{m}_{i_{gas\,out}} + \dot{m}_{i_{liquid\,in}} - \dot{m}_{i_{liquid\,out}} \tag{3.1}$$

where *i = (LV,AO,LA)* the tank index and the fluid resistances are modeled as

$$\begin{aligned} \dot{m}_{i_{in}} &= g_{i_{in}}\,\Delta P_{i_{in}} \\ \dot{m}_{i_{out}} &= g_{i_{out}}\,\Delta P_{i_{out}} \end{aligned} \tag{3.2}$$

with m_i, ΔP_i, and $g_i = 1/R_i$ the mass, the pressure difference, and the conductance rates of the component i as shown in Table 3.1, respectively. On the other hand, the rate of change in the stored fluid mass is written in terms of its volume and density as

$$\dot{m}_{st,i} = \dot{\rho}_i V_i + \rho_i \dot{V}_i \tag{3.3}$$

with ρ_i fluid density for i as given in Table 3.1. Therefore, the rate of change in density, when exists, is driven by substituting (3.3) into (3.1) as

$$\dot{\rho}_i = \frac{1}{V_i}\left[\left(\dot{m}_{i_{gas\,in}} - \dot{m}_{i_{gas\,out}} + \dot{m}_{i_{liquid\,in}} - \dot{m}_{i_{liquid\,out}}\right) - \rho_i \dot{V}_i\right] \tag{3.4}$$

This enables us to express the variable capacitance phenomenon. For our system the following assumptions are made

- V_T is constant,
- The temperature is constant,
- The shape of tank is rigid.

the time derivative of the pressure, $P_i = \rho_i RT$, becomes

$$\dot{P}_i = \dot{\rho}_i RT \tag{3.5}$$

with R the specific gas constant, T temperature. Combining (3.4) and (3.5) represents the equation of motion for the tank "i".

Using (3.4) and Equation (3.5), the general pressure law for each tank can be written as

$$\dot{P}_i = \frac{RT}{V_i}\left[\left(\dot{m}_{i_{gas\,in}} - \dot{m}_{i_{gas\,out}} + \dot{m}_{i_{liquid\,in}} - \dot{m}_{i_{liquid\,out}}\right) - \frac{P_i}{RT}\dot{V}_i\right] \tag{3.6}$$

In the next sections, we will develop equations of motion for each tank, individually.

3.3.2.2 Modeling The Balance Tank

The mass flow rate of the balance tank defined by the difference between in/out gas flow rates is given in

$$\dot{m}_{st,1} = \dot{m}_1 - \dot{m}_2 \tag{3.7}$$

with $\dot{m}_i$ the rate of changes in in/out masses that may, further, be expressed as

$$\begin{aligned} \dot{m}_1 &= g_1\,(P_c - P_1) \\ \dot{m}_2 &= g_2\left(P_1 - P_{LV,g}\right) \end{aligned} \tag{3.8}$$

where the conductance rates, g_i, and the pressure differences, ΔP_i, for $i = 1, 2$. Since the stored gas mass is

$$m_{st,1} = \rho_1 V_1 \tag{3.9}$$

and taking its derivative yieldsS

$$\dot{m}_{st,1} = \dot{\rho}_1 V_1 \tag{3.10}$$

Notice that using (3.5), the mass flow rate can also be written as

$$\dot{m}_{st,1} = \frac{V_1}{RT}\dot{P}_i \tag{3.11}$$

where V_1/RT is the capacitance $C_1 = 1/\alpha_1$. Thus, the pressure dynamics becomes

$$\dot{P}_1 = \alpha_1\{g_1(P_c - P_1) - g_2(P_1 - P_{LV,g})\} \tag{3.12}$$

with the elastance α_1 as given in Table 3.1.

3.3.2.3 Modeling The Left Ventricle Tank

LV tank is composed of two parts: the gas and liquid sections in which the former pressurizes the LV tank and the latter is used to transfer liquid according to the CVS. The conservation of mass for the tank for gas section is used to define the equations of motion as

$$\dot{m}_{LV,g} = \dot{m}_2 - \dot{m}_3 \tag{3.13}$$

where the intake and outtake masses flow rates

$$\begin{aligned} \dot{m}_2 &= g_2\left(P_1 - P_{LV,g}\right) \\ \dot{m}_3 &= g_3\left(P_{LV,g} - P_{out}\right) \end{aligned} \tag{3.14}$$

with g_2 and g_3 are the inlet and outlet conductances of LV chamber given in Table 3.1. P_{out} is the atmosphere pressure. Similarly, the storage mass can be described using (3.3) yielding

$$\dot{m}_{LV,g} = \dot{C}_{LV,g}P_{LV,g} + C_{LV,g}\dot{P}_{LV,g} \tag{3.15}$$

or

$$\dot{m}_{LV,g} = \dot{\rho}_{LV,g} V_{LV,g} + \rho_{LV,g} \dot{V}_{LV,g} \tag{3.16}$$

with $C_{LV,g}$ and $\rho_{LV,g}$ are the gas capacitance and the gas density in the LV tank, respectively. In (3.15) and Equation (3.16), we can write the storage of mass in terms of either capacitance or density forms. Using (3.5) and (3.16), we get (3.17).

$$\dot{m}_{LV,g} = \dot{P}_{LV,g} \frac{V_{LV,g}}{RT} + P_{LV,g} \frac{\dot{V}_{LV,g}}{RT} \tag{3.17}$$

(3.17) is utilized to obtain specific compliance value on gas section since physiological LV model changes its capacitance value when contraction/relaxation happens. The gas capacitance of LV chamber is $C_{LV,g} = \frac{V_{LV,g}}{RT}$, then

$$\dot{C}_{LV,g} = \frac{\dot{V}_{LV,g}}{RT} \tag{3.18}$$

Using the proposed hMCL assumptions given above, the total tank volume (V_T) is expressed by (3.19).

$$V_T = V_{LV,g} + V_{LV,l} \rightarrow V_{LV,g} = V_T - V_{LV,l} \tag{3.19}$$

with $V_{LV,g}$ and $V_{LV,l}$ are gas and liquid volume of LV chamber. The liquid volume of LV is written using (3.19) like

$$V_{LV,l} = Ay \rightarrow V_{LV,l} = A\left(\frac{P_{LV} - P_{LV,g}}{\rho_l G}\right) \tag{3.20}$$

where y, A, P_{LV} and $P_{LV,g}$ are liquid head, area , the total and gas pressure of LV chamber, respectively. The $C_{LV,g}$ is written using (3.18) in terms of the pressures of LV chamber

$$C_{LV,g} = \frac{1}{RT}\left(V_T - A\left(\frac{P_{LV} - P_{LV,g}}{\rho_l G}\right)\right) \tag{3.21}$$

Taking the derivative of (3.19) yields

$$\dot{V}_T = \dot{V}_{LV,g} + \dot{V}_{LV,l} \rightarrow \dot{V}_{LV,g} = -\dot{V}_{LV,l} \tag{3.22}$$

with $V_{LV,g}$ and $V_{LV,l}$ are gas and liquid volume of LV chamber. From the conversation of the mass the volume dynamics is derived using (3.4) as

$$\dot{V}_{LV,l} = \frac{1}{\rho_l}[g_{TLI}(t)(P_{LA} - P_{LV}) - g_{TLO}(t)(P_{LV} - P_{AO})] \tag{3.23}$$

where ρ_l are the density of liquid, the time-varying mitral and aortic conductances of $g_{TLI}(t)$ and $g_{TLO}(t)$ as shown in [92]. The liquid mass flow rates is now be put into (3.23). The definition of those conductances are

$$\begin{aligned} g_{TLI}(t) &= \theta_m(t)[g_m + g_M + g_P] \\ g_{TLO}(t) &= \theta_{AO}(t)[g_{ao} + g_{AO} + g_P] \end{aligned} \tag{3.24}$$

where $\theta_m(t)$ and $\theta_{AO}(t)$ are the opening rate of the mitral and AVs, respectively. g_i are the pipeline and valve conductance rates given in Table 3.1. Using (3.18) and (3.23) gives us the time derivative of the LV gas capacitance formulation as

$$\dot{C}_{LV,g} = \frac{1}{\rho_l RT}[g_{TLO}(t)(P_{LV} - P_{AO}) - g_{TLI}(t)(P_{LA} - P_{LV})] \tag{3.25}$$

with $P_{LA}$and P_{AO} are total pressure of LA and Aorta chamber. Using (3.15), we obtain

$$\dot{P}_{LV,g} = -\frac{\dot{C}_{LV,g}}{C_{LV,g}} P_{LV,g} + \frac{1}{C_{LV,g}}\left[g_2\left(P_1 - P_{LV,g}\right) - g_3\left(P_{LV,g} - P_{out}\right)\right] \tag{3.26}$$

Now, the total pressure, LVP, is expressed with (3.27).

$$\dot{P}_{LV} = \dot{P}_{LV,g} + \rho_l G \frac{\dot{V}_{LV,l}}{A} \tag{3.27}$$

with G the gravity of the earth. Putting both (3.26) and (3.23) yields (3.28).

$$\begin{aligned} \dot{P}_{LV} = &-\frac{\dot{C}_{LV,g}}{C_{LV,g}} P_{LV,g} + \frac{1}{C_{LV,g}}\left[g_2\left(P_1 - P_{LV,g}\right) - g_3\left(P_{LV,g} - P_{out}\right)\right] + \\ &\frac{G}{A}[g_{TLI}(t)(P_{LA} - P_{LV}) - g_{TLO}(t)(P_{LV} - P_{AO})] \end{aligned} \tag{3.28}$$

It is important to note that $\theta_m(t)$ and $\theta_{AO}(t)$equal to ”0” when the opening angle is lower than 45° as stated in [92].

3.3.2.4 Modeling The Aorta Tank

In the aorta tank, we have total mass equation, $m_{AO,g} = C_{AO,g}P_{AO,g}$, and taking derivative of it yielding

$$\dot{m}_{AO,g} = \dot{C}_{AO,g}P_{AO,g} + C_{AO,g}\dot{P}_{AO,g} \tag{3.29}$$

where $C_{AO,g}$ and $P_{AO,g}$ are the gas capacitance and pressure of Aorta chamber. The inlet and outlet gas flow are defined by both (3.30) and (3.31).

$$\dot{m}_{AO,g} = \dot{m}_5 - \dot{m}_7 \tag{3.30}$$

where the intake and outtake masses flow rates

$$\begin{aligned} \dot{m}_5 &= g_5\left(P_1 - P_{AO,g}\right) \\ \dot{m}_7 &= g_7\left(P_{AO,g} - P_{out}\right) \end{aligned} \tag{3.31}$$

where g_5 and g_7 are the gas inlet and outlet conductance rate of Aorta chamber. Using $C_{AO,g} = V_{AO,g}/RT$ given in (3.18), we take the derivative of gas capacitacne of aorta tank like

$$\dot{C}_{AO,g} = \frac{\dot{V}_{AO,g}}{RT} \tag{3.32}$$

Then both aortic gas capacitance and derivative of it are given in (3.33) and (3.34).

$$C_{AO,g} = \frac{1}{RT}\left(V_T - A\left(\frac{P_{AO} - P_{AO,g}}{\rho_l G}\right)\right) \tag{3.33}$$

$$\dot{C}_{AO,g} = \frac{1}{\rho_l RT}\left[g_{SYS}(P_{AO} - P_{LA}) - g_{TLO}(t)(P_{LV} - P_{AO})\right] \tag{3.34}$$

with g_{SYS} is total systemic conductance rate and equals to $g_{SYS} = g_{sys} + g_P$ from Table 3.1. The aortic gas dynamic is now written like

$$\dot{P}_{AO,g} = -\frac{\dot{C}_{AO,g}}{C_{AO,g}}P_{AO,g} + \frac{1}{C_{AO,g}}\left[g_5\left(P_1 - P_{AO,g}\right) - g_7\left(P_{AO,g} - P_{out}\right)\right] \tag{3.35}$$

Now, $\dot{P}_{AO,l} = \rho_l G\frac{\dot{V}_{AO,l}}{A}$, then using (3.35) with $\dot{P}_{AO} = \dot{P}_{AO,g} + \dot{P}_{AO,l}$, we get

$$\dot{P}_{AO} = -\frac{\dot{C}_{AO,g}}{C_{AO,g}} P_{AO,g} + \frac{1}{C_{AO,g}} \left[g_5 \left(P_1 - P_{AO,g} \right) - g_7 \left(P_{AO,g} - P_{out} \right) \right] + \frac{G}{A} \left[g_{TLO}(t) (P_{LV} - P_{AO}) - g_{SYS} (P_{AO} - P_{LA}) \right] \tag{3.36}$$

3.3.2.5 Modeling The Left Atrium Tank

In the LA tank, the conversation of mass is written by, $m_{LA,g} = C_{LA,g} P_{LA,g}$, and taking derivative gives us

$$\dot{m}_{LA,g} = \dot{C}_{LA,g} P_{LA,g} + C_{LA,g} \dot{P}_{LA,g} \tag{3.37}$$

where $C_{LA,g}$ and $P_{LA,g}$ are the gas capacitance and pressure of LA chamber. The inlet and outlet gas flow are defined by both (3.38) and (3.39).

$$\dot{m}_{LA,g} = \dot{m}_4 - \dot{m}_6 \tag{3.38}$$

where

$$\begin{aligned} \dot{m}_4 &= g_4 \left(P_1 - P_{LA,g} \right) \\ \dot{m}_6 &= g_6 \left(P_{LA,g} - P_{out} \right) \end{aligned} \tag{3.39}$$

where g_4 and g_6 are the gas inlet and outlet conductance rate given in Table 3.1. Using $C_{LA,g} = V_{LA,g}/RT$, we obtain

$$\dot{C}_{LA,g} = \frac{\dot{V}_{LA,g}}{RT} \tag{3.40}$$

where $V_{LA,g}$ is the gas volume of LA chamber. Now both LA gas capacitance and derivative of it can be stated in (3.41) and (3.42).

$$C_{LA,g} = \frac{1}{RT} \left(V_T - A \left(\frac{P_{LA} - P_{LA,g}}{\rho_l G} \right) \right) \tag{3.41}$$

$$\dot{C}_{LA,g} = \frac{1}{\rho_l RT} \left[g_{TLI}(t) (P_{LA} - P_{LV}) - g_{SYS} (P_{AO} - P_{LA}) \right] \tag{3.42}$$

The LA gas dynamic is now expressed with

$$\dot{P}_{LA,g} = -\frac{\dot{C}_{LA,g}}{C_{LA,g}} P_{LA,g} + \frac{1}{C_{LA,g}} \left[g_4 \left(P_1 - P_{LA,g} \right) - g_6 \left(P_{LA,g} - P_{out} \right) \right] \tag{3.43}$$

Now, $\dot{P}_{LA,l} = \rho_l G \frac{\dot{V}_{LA,l}}{A}$, then using (3.43) with $\dot{P}_{LA} = \dot{P}_{LA,g} + \dot{P}_{LA,l}$, we obtain

$$\dot{P}_{LA} = -\frac{\dot{C}_{LA,g}}{C_{LA,g}} P_{LA,g} + \frac{1}{C_{LA,g}}\left[g_4\left(P_1 - P_{LA,g}\right) - g_6\left(P_{LA,g} - P_{out}\right)\right] + \frac{G}{A}\left[g_{SYS}(P_{AO} - P_{LA}) - g_{TLI}(t)(P_{LA} - P_{LV})\right] \tag{3.44}$$

After that, the equations of motion can be rewritten as a state-space representation form which is illustrated in (3.45).

$$\dot{x} = A(x,t)x + B(x)u \tag{3.45}$$

where the states are $x = \begin{bmatrix} P_1 & P_{LV,g} & P_{LV} & P_{AO,g} & P_{AO} & P_{LA,g} & P_{LA} \end{bmatrix}^T$. The input of the state space is represented by $u = [g_1 \;\; g_2 \;\; g_3 \;\; g_4 \;\; g_5 \;\; g_6 \;\; g_7]^T$. The state and input matrices are

$$A(x,t) = \begin{bmatrix} 0 & 0 & 0 & 0 \\ 0 & -\frac{\dot{C}_{LV,g}(x)}{C_{LV,g}(x)} & 0 & 0 \\ 0 & -\frac{\dot{C}_{LV,g}(x)}{C_{LV,g}(x)} & \frac{G}{A}\left(-g_{TLI}(t) - g_{TL0}(t)\right) & 0 \\ 0 & 0 & 0 & -\frac{\dot{C}_{AO,g}(x)}{C_{AO,g}(x)} \\ 0 & 0 & \frac{G}{A} g_{TL0}(t) & -\frac{\dot{C}_{AO,g}(x)}{C_{AO,g}(x)} \\ 0 & 0 & 0 & 0 \\ 0 & 0 & \frac{G}{A} g_{LTI}(t) & 0 \end{bmatrix} \tag{3.46a}$$

$$\begin{bmatrix} 0 & 0 & 0 \\ 0 & 0 & 0 \\ \frac{G}{A} g_{TL0}(t) & 0 & \frac{G}{A} g_{TLI}(t) \\ 0 & 0 & 0 \\ \frac{G}{A}\left(-g_{TLO}(t) - g_{SYS}(t)\right) & 0 & \frac{G}{A} g_{SYS} \\ 0 & -\frac{\dot{C}_{LA,g}(x)}{C_{LA,g}(x)} & 0 \\ \frac{G}{A} g_{SYS} & -\frac{\dot{C}_{LA,g}(x)}{C_{LA,g}(x)} & \frac{G}{A}\left(-g_{SYS} - g_{TLI}(t)\right) \end{bmatrix}_{7x7}$$

$$B(x) = \begin{bmatrix} (P_c - P_1)\alpha_1 & -(P_1 - P_{LV,g})\alpha_1 & 0 & 0 \\ 0 & \frac{1}{C_{LV,g}(x)}(P_1 - P_{LV,g}) & -\frac{1}{C_{LV,g}(x)}(P_{LV,g} - P_{out}) & 0 \\ 0 & \frac{1}{C_{LV,g}(x)}(P_1 - P_{LV,g}) & -\frac{1}{C_{LV,g(x)}}(P_{LV,g} - P_{out}) & 0 \\ 0 & 0 & 0 & \frac{1}{C_{AO,g}(x)}(P_1 - P_{AO,g}) \\ 0 & 0 & 0 & \frac{1}{C_{AO,g}(x)}(P_1 - P_{AO,g}) \\ 0 & 0 & 0 & 0 \\ 0 & 0 & 0 & 0 \end{bmatrix}^{\cdots}$$

$$\begin{bmatrix} 0 & 0 & 0 \\ 0 & 0 & 0 \\ 0 & 0 & 0 \\ 0 & -\frac{1}{C_{AO,g}(x)}(P_{AO,g} - P_{out}) & 0 \\ 0 & -\frac{1}{C_{AO,g}(x)}(P_{AO,g} - P_{out}) & 0 \\ \frac{1}{C_{LA,g}(x)}(P_1 - P_{LA,g}) & 0 & -\frac{1}{C_{LA,g}(x)}(P_{LA,g} - P_{out}) \\ \frac{1}{C_{LA,g}(x)}(P_1 - P_{LA,g}) & 0 & -\frac{1}{C_{LA,g}(x)}(P_{LA,g} - P_{out}) \end{bmatrix}_{7x7} \quad (3.46b)$$

3.3.3 A New Volume-Elastance Equation

In hMCL applications, achieving physiological LVV that matches both left ventricular pressure (LVP) and AOP characteristics presents a challenge due to the limited physiological capacitance range provided by hMCL designs. The mechanical tank used in the hMCL device does not adequately capture the low capacitance values observed in the human body. Consequently, the volume change of the fluid-filled silicone membrane (FSM) fails to track the reference LVP and AOP signals [85], [88]. To address this limitation, a new volume-elastance equation is proposed that incorporates both the LVV and the capacitance value of the LV gas chamber. In physiological terms, LV contractility represents the instantaneous change in elastance associated with its capacitance. Therefore, the hMCL LV chamber is modeled as a gas capacitance to accurately mimic the physiological behavior of the LV muscle during contraction and relaxation. The coupling between volume and elastance is derived based on this capacitance, faithfully replicating the physiological nature of the FSM. By adopting this approach, our proposed hMCL setup can modulate the LVP in response to the LV volume stored in the LV chamber. This novel volume-elastance equation allows the proposed hMCL to not only track the targeted LVV in line with the FSM but also dynamically adjust the LVP according to the LVV.

To ensure the physiological behavior of the CVS, the system is reduced to three dynamic equations while leaving other components free in the simulation process. In physiology, most elements of the CVS are passive, except for the heart muscle, which acts as the primary actuator generating sufficient pressure and flow rate. Thus, it is crucial in this context to ensure that only the LVV is controlled to achieve FSM-driven adjustments of the proper LV contractility rate, aligning with the physiological functioning of the CVS.

In order to obtain total capacitance equation, firstly, left ventricular gas chamber mass can be stated as

$$m_{LV,g} = \rho_{LV,g} V_{LV,g} \tag{3.47}$$

where $\rho_{LV,g}$ and $V_{LV,g}$ are the density and volume of LV chamber. Then, derivative of (3.47) gives us

$$\dot{m}_{LV,g} = \dot{\rho}_{LV,g} V_{LV,g} + \rho_{LV,g} \dot{V}_{LV,g} \tag{3.48}$$

Using (3.5), the chain rule is applied on (3.48) to derive the collective capacitance parameter like

$$\dot{m}_{LV,g} = \dot{P}_{LV,g} C_g \tag{3.49}$$

or

$$\dot{m}_{LV,g} = \dot{P}_{LV,g} \left(C_{LV,g} + \frac{dC_{LV,g}}{dP_{LV,g}} P_{LV,g} \right) \tag{3.50}$$

where $C_g(t)$ is collective parameter indicating $\left(C_{LV,g} + \frac{dC_{LV,g}}{dP_{LV,g}} P_{LV,g} \right)$ not only compliance value of gas but it incorporates the dynamics of the liquid and gas. Now, splitting the $\dot{V}_{LV,g}$ into differentiable parts as

$$\dot{V}_{LV,g} = \frac{dV_{LV,g}}{dP_{LV,g}} \frac{dP_{LV,g}}{dt} \tag{3.51}$$

Using (3.5) to turn the capacitance formula into the volume one, the last form equals to

$$\dot{m}_{LV,g} = \dot{P}_{LV,g}\left(\frac{V_{LV,g}}{RT} + \frac{dV_{LV,g}}{dP_{LV,g}}\frac{P_{LV,g}}{RT}\right) \tag{3.52}$$

Now, $C_g(t)$ can be obtained using (3.20) like

$$C_g(t) = \frac{1}{RT}\left[V_T + \frac{2AP_{LV,g}}{\rho_l G} - \frac{P_{LV}A}{\rho_l G}\right] \tag{3.53}$$

This calculation plays a vital role in controlling the proposed system as it enables the specific control of the LV gas section, analogous to controlling the heart muscle in physiological terms. Additionally, it is necessary to determine the dynamics of the LVV to establish the structure of the volume controller within the hMCL.

In the proposed hMCL, the numerical model is obtained using the state space representation given in (3.46). The equations of motion of the CVS is obtained using physiological signals $x(t)$ at the same equation. However, the CVS order must be reduced to three equations in order to implement the new volume-elastance formula given in (3.53).

The reduced order CVS model are now rewritten as

$$\begin{aligned}
\dot{P}_1 &= g_1(P_C - P_1)\alpha_1 - g_2\big(P_1 - P_{LV,g}\big)\alpha_1 \\
\dot{P}_{LV,g} &= g_2\big(P_1 - P_{LV,g}\big)\alpha_g - g_3\big(P_{LV,g} - P_{out}\big)\alpha_g \\
\dot{V}_{LV,l} &= -\frac{A}{\rho_l G}\left[g_2\big(P_1 - P_{LV,g}\big)\alpha_g - g_3\big(P_{LV,g} - P_{out}\big)\alpha_g\right]
\end{aligned} \tag{3.54}$$

where α_g is collective volume-elastance formula. This last form only includes heart muscle analogy of the present hMCL. It is important to note that the proposed hMCL should only be controlled using the reference LVV signal in order to satisfy the coupling both the FSM and LV contractility rate in a physiological manner. Therefore, it is sufficient to design discrete feedback linearization control guaranteeing stability for simulating the physiological CVS.

In order to drive the proposed hMCL, there are two reference signals needs to be defined as LVV (V_{ref}) and balance tank pressure one ($P_{1,ref}$). The V_{ref} is established using the maximum and minimum values of LVV required to provide the FSM. On the other hand, $P_{1,ref}$ is selected as unit step signal which can easily

be adjusted using a coefficient that shows the targeted pressure value in the balance tank.

3.3.4 Stability Analysis

The continuous model, (3.54), is discretized using Euler forward difference equation. In this study, discrete feedback linearization controller design is performed in order to track the reference LVV given within the range of physiological conditions using Lyapunov Stability Theorem similar to [93].

3.3.5 Error System Dynamics

The main objective of the hMCL device is to track a reference LV volume signal, $V_{ref}[k]$ defining physiological CVS. Thus, we define LVV error

$$e_{LV}[k] = V_{ref}[k] - V_{LV,l}[k] \tag{3.55}$$

and the pressure error

$$e_{P1}[k] = P_{1,ref}[k] - P_1[k] \tag{3.56}$$

with $V_{ref}[k]$ and $P_{1,ref}[k]$ the reference LVV and the pressure signals satisfying human CVS hemodynamics. Discretizing LVV from (3.54) yields

$$\begin{aligned} V_{LV,l}[k+1] &= V_{LV,l}[k] + f_{lv}(g_2[k]V_{11}[k] - g_3[k]V_{12}[k]) \\ with\ f_{lv} &= -\frac{A}{\rho_l G}\Delta t \\ V_{11}[k] &= \big(P_1[k] - P_{LV,g}[k]\big)\alpha_g[k] \\ V_{12}[k] &= \big(P_{LV,g}[k] - P_{out}[k]\big)\alpha_g[k] \end{aligned} \tag{3.57}$$

Substituting (3.57) into the LVV error equation yields the reference tracking error dynamics as

$$\begin{aligned} e_{LV}[k+1] &= V_{ref}[k+1] - V_{LV,l}[k] \\ &-\Delta t(f_{lv}g_2[k]V_{11}[k] - g_3[k]V_{12}[k]) \end{aligned} \tag{3.58}$$

Similarly steps are applied to the discrete pressure difference equation from (3.54) as

$$P_1[k+1] = P_1[k] + f_p(g_1[k]V_{21}[k] - g_2[k]V_{22}[k])$$
$$with\ f_p = \Delta t$$
$$V_{21}[k] = (P_c[k] - P_1[k])\alpha_1[k] \tag{3.59}$$
$$V_{22}[k] = \big(P_1[k] - P_{LV,g}[k]\big)\alpha_1[k]$$

Substituting (3.59), now, into the pressure error, the tracking error dynamics becomes

$$e_{p1}[k+1] = P_{1,ref}[k+1] - P_1[k]$$
$$-f_p(g_1[k]V_{21}[k] - g_2[k]V_{22}[k]) \tag{3.60}$$

We are, now, ready to state the controller to achieve the reference tracking of LV signals.

Theorem 3.1. *The pneumatic valve control signals*

$$g_1[k] = \frac{A_{e,P1}e_{P1}[k] - P_{1,ref}[k+1] + P_1[k] - f_pV_{22}[k]g_2[k]}{-f_pV_{21}[k]} \tag{3.61}$$

$$g_2[k] = \frac{C_1}{C_g[k]} \tag{3.62}$$

$$g_3[k] = \frac{A_{e,LV}e_{LV}[k] - V_{ref}[k+1] + V_{LV,l}[k] - f_{lv}V_{11}[k]g_2[k]}{-f_{lv}V_{12}[k]} \tag{3.63}$$

with $|A_{e,P1}| < 1$ and $|A_{e,LV}| < 1$ gains, applied to the hMCL system ensures the stability of the closed-loop system.

Proof. The quadratic tracking error is selected as the Lyapunov function candidate both for the pressure and LVV

$$L[k] = L_P[k] + L_{LV}[k] = e_{P1}[k]^2 + e_{LV}[k]^2 \tag{3.64}$$

with $L_P[k] = e_{P1}[k]^2$ and $L_{LV}[k] = e_{LV}[k]^2$. The difference equation for $L_i[k]$ for $i = \{P_1, LV\}$ is

$$L_i[k+1] - L_i[k] = e_i[k+1]^2 - e_i[k]^2 \tag{3.65}$$

By substituting the control signals (3.61-3.63) into the pressure and the LVV error dynamics given in (3.60) and (3.58), it can be shown by direct substitution that

$$e_i[k+1] = A_{e,i} e_i[k] \tag{3.66}$$

Thus,

$$L_i[k+1] - L_i[k] = \left(A_{e,i}^2 - 1\right) e_i[k]^2 \leq 0 \tag{3.67}$$

since $\left|A_{e,i}\right| < 1$.

Therefore, the non-increasing Lyapunov functions guarantee the boundedness of $e_i[k]$ reference tracking signals and observing the relationship between the gas pressure and liquid volume of $\dot{P}_{LV,g} = -\frac{\rho_l G}{A} \dot{V}_{LV,l}$ one can deduce the boundedness of PLV,g. This concludes the stability of the overall system

Remark. *We have used mainly the LVV reference signal to generate left ventricular pressure and mass flow rate signals from the hMCL device, satisfying the FSM.*

To match physiological response of CVS with the proposed hMCL, the capacitance values of aorta and LA must be satisfied. In order to control the capacitance of the aortic and left atrium tank, the same logic must be followed as given above. However, (3.54) must be rewritten representing both the aortic and left atrium capacitance formulation which are given in both (3.32) and (3.40).

3.4 Results

In this study, all experiments were conducted using both the Matlab 2022a Simulink Platform and the proposed hMCL. A comparison and validation of the results were then carried out to ensure their consistency with the physiological response of the CVS.

Firstly, the numerical and hMCL experiments were conducted to demonstrate the results, including healthy cases, in terms of pressure, volume, and both active and passive pressure of the LV. The physiological limits were assessed to determine the similarity between our model and the physiological model described in the literature. Secondly, the proposed hMCL was tested by varying the resistance values to simulate AS and systemic abnormalities, achieved by adjusting the orifice

area of the pipelines. This allowed for the evaluation of time response. Thirdly, the different heart rate references were applied to assess the CO, in comparison to physiological studies documented in the literature.

Figure 3.3 demonstrated a comparison between the proposed hMCL and numerical experiment results, focusing on the LVV, as well as the AOP and LVP.

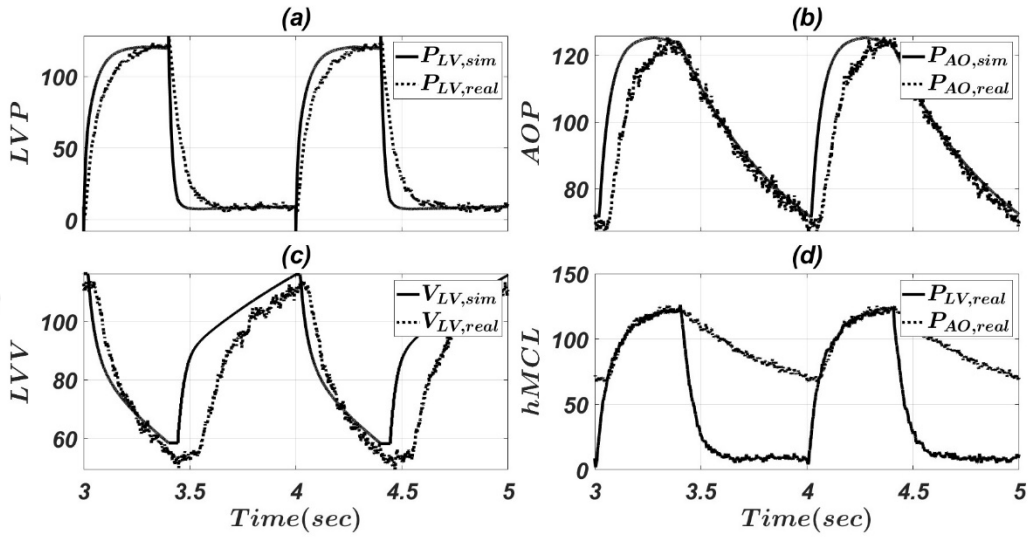


Figure 3.3. Results of the numerical and hMCL. a) LVP b) AOP c) LVV d) only hMCL

In Figure 3.3, Figure 3.3a and Figure 3.3b represented the hMCL measurement of LVP and AOP respectively. It is noteworthy that the numerical CVS responses closely matched the hMCL responses. However, there were some signal distortions due to sensor and electronic component limitations. The overall median error between the hMCL and numerical simulation was calculated as 3.01 ± 11.23mmHg. In Figure 3.3c, the LVV responses were presented to compare the hMCL and numerical data. Achieving control over the volume changes in the LV chamber led to more accurate results, with a standard deviation of 1.43±5.24mmHg, demonstrating a close resemblance between the numerical and hMCL data.

The active and passive pressures of LV were demonstrated in Figure 3.4.

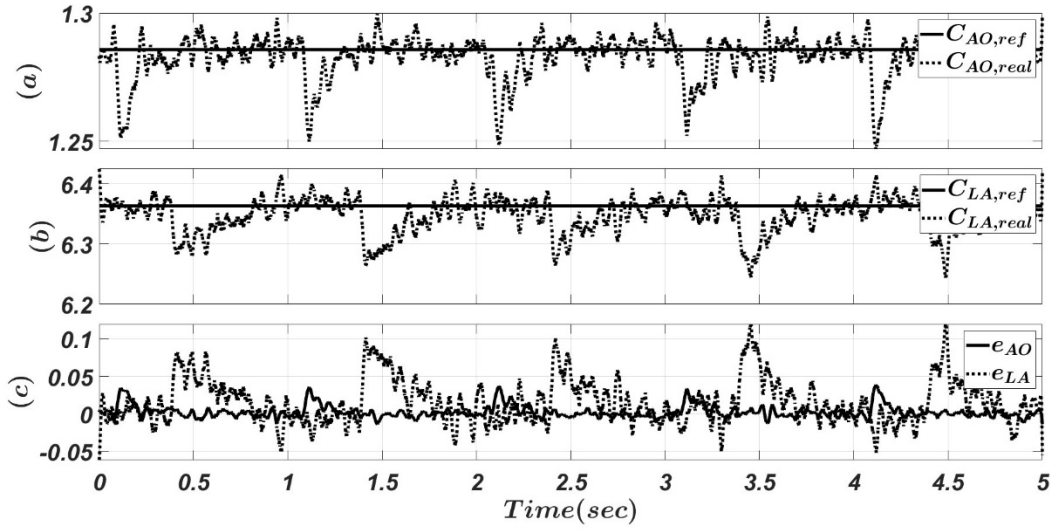


Figure 3.4. The tracking performance of capacitance. a) Left atrium b) Aorta

Figure 3.4 shows that numerical and hMCL results of both Aortic and LA capacitance obtained from the utilization of the proposed volume-elastance equations. The reference values were set to be in accordance with Simaan et al. model. The result clearly indicated that the capacitances could be matched by controlling only the gas capacitances. The error between both numerical and hMCL experiment were performed at the rate of 0.0137±0.0294 and 0.003±0.0083 ml/mmHg for left atrium and aortic capacitance values.

After these tests accomplished, CV dysfunctions were tried to observe on the numerical and hMCL experiments. Figure 3.5 demonstrated these results by changing resistance values corresponding with the AS and SVR.

In Figure 3.5, the pressure, resistance, and volume values were measured from numerical and hMCL. Figure 3.5a and Figure 3.5b represented the pressure response under the AS condition which means that aortic resistance increased while constant heart rate and reference volume in LV chamber. After passing 6 seconds, the SVR was increased in order to obtain the time response of the proposed hMCL. The pressure value increased when flow rate of LV decreased. At the hMCL experiment, it gaves the correlation at the rate of 14.15 ± 22.12mmHg, 4.29 ± 13.22mm, and 1.04 ± 1.43mmHgsec /ml. The same test with systemic performance also caused differences at the rate of 12.41±18.03mmHg, 4.91±7.54mm milliliter, and 0.11 ± 0.23mmHgsec /ml.

The last test to prove the physiological imitation with hMCL was performed at the different heart rate conditions in the range of 30 to 120 bpm. The results were illustrated in Figure 3.6.

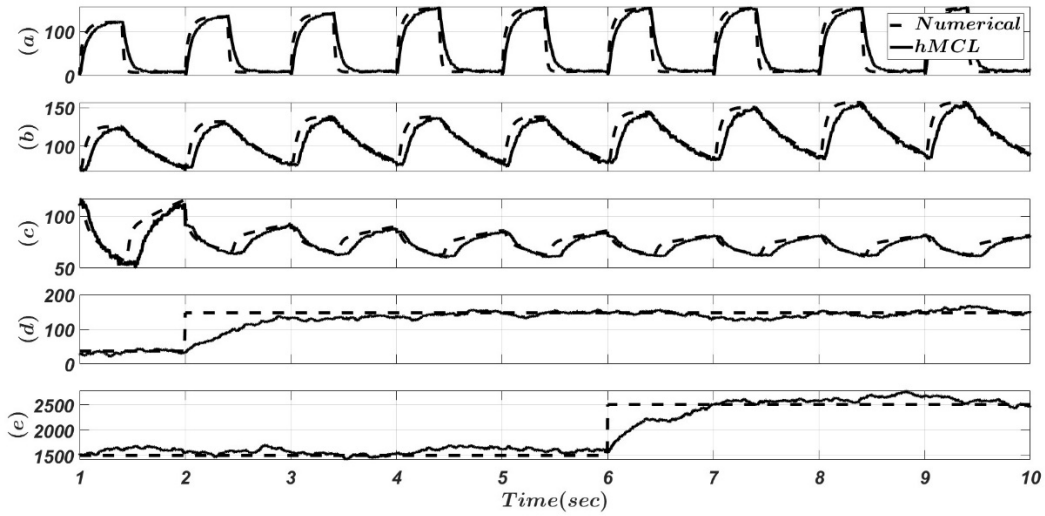


Figure 3.5 The results of AS and SVR response: a) LVP b) AOP c) LVV d) Aorticr Resistance e) SVR

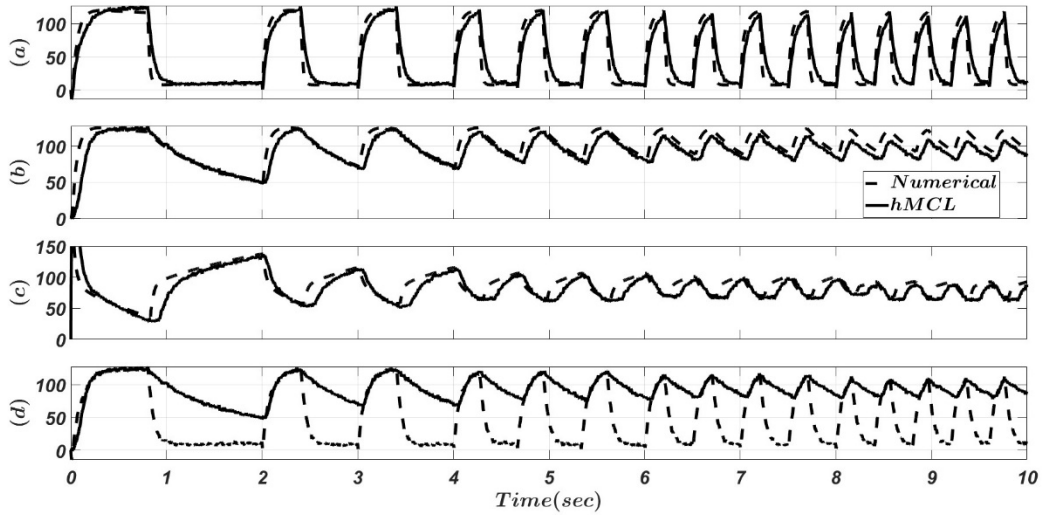


Figure 3.6 The results of different heart rate. a) LVP b) AOP c) LVV d) hMCL LVP and AOP

In Figure 3.6, the numerical and hMCL results were given containing the different heart rates and their corresponding volume change in left ventricular chamber. It was noteworthy that the numerical results were consistent at every heart rate for both volume and pressure values of LV. However, hMCL experiments clearly showed that the volume change of LV decreased when heart rate increased. At the

same time, the pressure values were not significantly affected by heart rate deviation in real time experiment.

3.5 Discussion

This paper presents a novel design and control approach for hMCL, incorporating a new volume/ elastance equation to simulate the FSM in the CVS. The methodology is subject to both mathematical and physiological considerations.

From a mathematical standpoint, we propose a discrete nonlinear system dynamic model along with its corresponding controller structure. To the best of our knowledge, there is currently no established controller rule that guarantees stability for gas valve dynamics in the discrete time domain. In contrast to previous studies, our discretized feedback linearization controller design focuses exclusively on the gas section of the LV model. The proposed volume-elastance dynamics play a crucial role in providing physiological relevance to the hMCL, as they enable control over only the gas chamber of the LV, thereby activating the left ventricular muscle. The remaining state variables of the hMCL are left unconstrained, aligning with physiological conditions.

Numerical and hMCL simulations were performed to assess the reliability of the volumeelastance dynamics. Table 3.2 presents the performance comparison between the numerical and hMCL results, offering insights into the effectiveness of our approach.

Table 3.2 demonstrates a close correspondence between the numerical and hMCL results. Various factors contribute to the observed discrepancies, including the discretization process applied to the mathematical model, parameters of the Kalman filter, sensor noise, noise introduced by the microcontroller's ADC module, and limitations in the mechanical structure. It is particularly important to assess the performance of the hMCL in light of these mechanical limitations, as the resistance and capacitance values may deviate from their real counterparts due to the threedimensional shape of the device. Although the Kalman filter helps mitigate these issues within the controller algorithm and nonlinear model, achieving a one-to-one match in such systems is not always feasible.

Table 3.2 Numerical and hMCL results

@60 bpm	***Physiological Ventricle (PV)***		***Aortic Stenosis (AS)***		***Systemic Vascular Resistance (SVR)***	
The proposed	*Numerical*	*hMCL*	*Numerical*	*hMCL*	*Numerical*	*hMCL*
$P_{lv,max}$ (mmHg)	**131.22**	**133.78**	**153.52**	**156.08**	**156.14**	**157.13**
$P_{lv,min}$(mmHg)	**10.23**	**7.61**	**13.87**	**10.42**	**12.58**	**14.27**
$P_{ao,max}$(mmHg)	**129.11**	**130.27**	**141.19**	**139.37**	**153.18**	**151.35**
$P_{ao,min}$(mmHg)	**74.64**	**72.48**	**78.33**	**75.17**	**89.77**	**87.41**
$V_{lv,max}$ (ml)	**118.56**	**116.23**	**97.44**	**99.76**	**91.06**	**92.32**
$V_{lv,min}$ (ml)	**50.04**	**46.41**	**54.24**	**51.14**	**56.61**	**56.13**
SV_{mean} (ml)	**64.52**	**67.82**	**38.19**	**41.66**	**31.89**	**34.65**
CO_{mean} (l/min)	**4.64**	**4.86**	**2.74**	**2.99**	**2.29**	**2.49**
$R_{ao,mean}$ (dyn.sec/cm^5)	**34**	**30.14**	**144**	**140.53**	**144**	**140.53**
$R_{sys,mean}$ (dyn.sec/cm^5)	**1500**	**1703.38**	**1500**	**1703.38**	**2500**	**2919.1**

In Table 3.3, the proposed hMCL results are illustrated under three cases: physiological LV, AS and systemic vascular change compared to other studies in the literature.

Table 3.3 Comparison table under (PV), AS and SVR change

		$P_{lv,mean}$	$P_{ao,mean}$	$V_{lv,max}$	$V_{lv,min}$	SV_{mean}	CO_{mean}	$R_{ao,mean}$	$R_{sys,mean}$
Physiological LV	The proposed hMCL	**60.28**	**83.13**	**116.23**	**46.41**	**67.82**	**4.86**	**30.14**	**1703.38**
	Packy et al. [89]	**53.9**	**73.4**	**-**	**-**	**67.00**	**5.03**	**-**	**1346.2**
	Bardi et al. [90]	**-**	**94.13**	**-**	**-**	**-**	**4.47**	**-**	**-**
	Vignali et al. [86]	**-**	**-**	**-**	**-**	**-**	**4.71**	**-**	**-**
	Salesch et al. [85]	**-**	**-**	**-**	**-**	**-**	**-**	**40.32**	**1333.2**

Table 3.3 Comparison table under (PV), AS and SVR change (continued)

	Gregory et al. [84]	**62.5**	**96**	**135**	**52**	**83**	**4.98**	**-**	**1400**
	Jansen-Park et al. [82]	**-**	**91**	**-**	**-**	**50**	**3.816**	**-**	**1728**
	Gregory et al. [81]	**-**	**110**	**-**	**-**	**72.2**	**5.2**	**-**	**-**
	The proposed hMCL	**74.87**	**118.13**	**99.76**	**51.14**	**41.66**	**2.99**	**140.53**	**1703.38**
	Rapp et al. [88]	**54.13**	**61.65**	**-**	**-**	**-**	**-**	**28.8**	**1548**
AS	Iscan and Yesildirek [92]	**78.44**	**112.47**	**92.18**	**47.13**	**34.11**	**2.45**	**115.2**	**1598.73**
	The proposed hMCL	**80.45**	**125.48**	**92.32**	**56.13**	**34.65**	**2.49**	**140.53**	**2919.1**
SVR	Colacino et al. [76]	**-**	**160**	**150**	**70**	**80**	**4.8**	**-**	**2773.44**

In Table 3.3, the proposed hMCL results are compared to other studies. Especially in the evaluation of CO, our results have correlation with 4.86 ± 1.04 l/min except Jansen-park et al. study due to utilization of Left Ventricle Assisted Device (LVAD) [82]. Mean left ventricular pressure happens 60.28±6.38 mmHg since Packy et. al set heart rate as 75 bpm unlike we have 60 bpm test condition [89]. Mean AOP has the standard deviation of 83.13 ± 12.38mmHg. In Gregory et al. study, AOP is higher than the proposed one because the pneumatic actuator of their study is directly taken pressure reference control, unlike our study utilizes only LVV reference [81]. SVR is achieved in close to the other studies with the standard deviation of 1703.3±370.18 dyn sec/cm5 dyn.sec/cm5. For the mean aortic resistance, only Salech et al. reported scalar value with the difference of 10.18 dyn sec/cm5 [85]. Systemic and aortic resistance depend on mechanical component and

manual valve which may change system to system, so, they are acceptable to meet the criteria of the proposed hMCL.

For the AS case, only Rapp et al. gave the some graphical results [88]. However, their device structure different from our one, so, resistance and left and AOP values are changed compared to our study. Besides, the time response of AS in their study corresponds to our results especially in terms of aortic and left ventricular pressure one. On the other hand, our previous work has strong correlation with the present study due to the utilization of the same AV model [92].

In the case of increasing SVR mean SVR value is matched with Colacino et al. result [76]. The mean error rate equals to 145.66 dyn sec/cm5 and is caused by different pipeline resistance and squeeze points. The other parameters are higher than our ones that we have obtained. Several reasons may cause these differences. Colacino et al. study utilize LVV generated by pressure references of LV. Also, mechanical pump generates the volumetric flow rate to supply the system in their study. Capacitance values of the tanks are different which means that they have different pressurizing range in their setup. Besides, AS is present with systemic vascular increment in our study, therefore, we may have different results compared to the other studies.

Finally, heart rate change is important matter to discuss about the imitation performance of the proposed hMCL with its discrete nonlinear system dynamic modelling. LVV is decreased when the heart rate increase since FSM dictates the transfer rate depending on preload values of the heart [94]. In hMCL results, although this constraint is not broken when increasing heart rate, real-time experiments showed that LVV is decreased with increasing heart rate. SV error value happens with the rate of 9.25 ml at the heart rate between 60 to 120 bpm with respect to Guyton's data [94].

3.6 Conclusion

In this study, we have introduced a novel design for a CV mock loop (hMCL) that incorporates a nonlinear discrete equation of motion and discrete feedback linearization control. A key contribution of this research is the proposal of a new capacitance formula, which allows for a more realistic representation of the

electrical excitation of the LV compared to conventional methods. As a result, the hMCL is capable of accurately emulating the FSM by controlling the volumetric rate of the LV across a range of heart rates (30 to 120 bpm), volumetric flow rates (0 to 5 l/min), and pressures (70-150 mmHg).

The conducted experiments have provided validation of the hMCL's capability to simulate critical CV conditions, including AS, changes in systemic resistance, and variations in heart rate. Remarkably, the hMCL achieves these simulations solely based on the LVV reference, demonstrating its effectiveness in replicating both normal and abnormal CV conditions.

Moving forward, our future studies will focus on addressing the mechanical limitations associated with the hMCL, particularly the dynamics of opening and closing valves (aortic and mitral) that impact resistance. To overcome this challenge, we will develop an estimation algo rithm that employs a neural network controller structure to predict real-time resistance values in the mock system. Furthermore, we aim to enhance the ECG-driven volume reference trajectory by incorporating additional parameters such as heart rate, contraction/relaxation periods, and the strength of contraction and relaxation, leveraging the interpretation of ECG signals.

In conclusion, the proposed hMCL system has demonstrated high performance in accurately simulating the physiological properties of the CVS, with a particular focus on the FSM, under both normal and abnormal conditions. Its ability to replicate a wide range of CV scenarios makes it a valuable tool for further understanding and investigating CV dynamics.

4
AN IMRPOVED INSTANTANEOUS AORTIC VALVE RESISTANCE ESTIMATION DURING THE ENTIRE CARDIAC CYCLE USING AI

4.1 Abstract

The aortic valve (AV) plays an important role in cardiovascular system (CV). The paper describes an improved model for the dynamic resistance of AV using a 2D convolutional neural network (CNN). In this study, the AV is considered as a periodic time-varying resistance and modeled with some parameters reflecting healthy and aortic stenosis (AS) conditions during the complete cardiac cycle. This resistance model is further enhanced by a 2D CNN correction term fitting the model to in-vitro measurements. The 2D input to the CNN is constructed by a set of critical CV signals producing rich excitations for the deep learning process. There is no labeled dataset and training process, the CNN learns its parameters in real-time using the residue between the AV model and the EKF estimation derived through in-vitro measurements. When compared to simpler diode models of AV with a constant resistance in ejection phase, the proposed model offers more realistic hemodynamic transients. To illustrate the validity of the proposed estimator in a more realistic "in-vitro" testing environment, a hybrid mock circulatory loop (hMCL), configured by a single controlled parameter while letting the others vary freely to satisfy the Frank-Starling mechanism is employed. Those noninvasive measurements of both the fluid mass flow rate though the left ventricle (LVQ) and AV resistance during the ejection phase observed with high accuracy. We have shown that the LVQ measurements obtained from the hMCL align closely with the reference data, with an error rate of less than 3.41±4.84% for the cardiac output in healthy condition and 2.83±1.35% in AS case. These results indicate that the proposed approach modeling the AV resistance can effectively estimate LVQ under various AV conditions.

4.2 Introduction

Cardiovascular diseases (CVDs) have been considered as a significant global concern, posing life-threatening risks to individuals [95]. Among these CVDs, aortic stenosis (AS) and regurgitation engage a critical position due to their detrimental effects on overall cardiovascular function [96]. The investigation of the complex interplay between cardiac output (CO) and aortic flow, with particular emphasis on the role of the aortic valve (AV) in maintaining optimal cardiovascular performance, has gained increasing importance [97]. However, the presence of AV diseases, such as stenosis, disrupts this delicate equilibrium [98]. Understanding the underlying mechanisms of AV function is crucial for accurate diagnosis and effective treatment. Nevertheless, conventional approaches have primarily relied on invasive procedures or mathematical models to achieve this understanding.

The current state-of-the-art in mathematical methods for estimating CO has relied on various approaches such as computational fluid dynamics (CFD) [99], thermodilution CO measurements [100], pulsed Doppler ultrasound-based pulse wave analysis [101], heart rate examination [102], and the implementation of the standard Windkessel Model with dynamic physiological processes [103]. While these mathematical models provide valuable tools for investigating hemodynamic quantities, they have limitations in terms of assumptions and simplifications of physiological models, particularly when dealing with complex scenarios. Moreover, their effectiveness is limited in capturing the intricate complexities observed in individual-specific cases, primarily due to the presence of nonlinear dynamics and interactions. As a result, researchers have turned their attention to exploring the potential of deep learning techniques, which have emerged as a promising avenue for incorporating a wide range of features, including demographic information and medical history, thereby enhancing their ability to estimate the CO [104]–[106]. However, these studies often overlook the importance of model-based integration for generalizing physiological outcomes. The accuracy and predictive performance of these algorithms heavily rely on training and validation tests using both invasive and noninvasive measurements obtained from patients [107], [108]. Furthermore, these studies frequently overlook model-based physiological principles, which can provide a broader coverage of physiological features relevant to the cardiovascular system.

The current state-of-the-art in the deep learning methods have been focused on estimating critical parameters, including peripheral resistance and capacitance, maximum elastance, pressure and flow rates of the left ventricle [34], [109]–[114]. These investigations have become apparent to the significance of incorporating these critical parameters, as they contribute to a more comprehensive understanding of the underlying mechanisms governing physiological processes [34], [112], [115], [116]. Particularly, when estimating the states of the physiological system using the Extended Kalman Filter (EKF), integrating model-based approaches becomes essential for addressing unknown dynamics. The incorporation of dynamic resistance or capacitance in the cardiovascular system (CVS) model is important to improve the estimation of pressure and flow rates, given that these parameters play an important role in accurately capturing the true physiological responses.

To address the aforementioned challenges, our previous study introduced a novel approach that incorporates an instantaneous aortic valve resistance (I-AVR) model within the CVS, integrating the left ventricular flow rate (LVQ), left ventricular pressure (LVP), and aortic pressure (AOP) [92]. This innovative approach enables accurate estimation of LVQ and provides insights into the underlying mechanisms of I-AVR under various CVS conditions, including healthy, AS and regurgitation cases. The incorporation of such an I-AVR model directly impacts the overall transient response, leading to a better understanding of the CVS dynamics.

This paper presents a novel methodology aimed at improving the EKF-based estimation of I-AVR introduced in [92]. The proposed approach utilizes a convolutional neural network (CNN) correction mechanism to match the model estimation with in-vitro measurements. Time-domain cardiovascular signals are transformed into a 2D representation and fed into the CNN, which computes the residue between the AV model and the in-vitro measurements. Unlike many existing methods that focus solely on steady-state AV resistance estimation under specific conditions, our approach offers a powerful I-AVR model. To validate the proposed estimator in a more realistic "in-vitro" testing scenario, we employ a hybrid mock circulatory loop (hMCL) that allows for the controlled variation of parameters while maintaining the Frank-Starling mechanism, which is relevant to the CO.

The main contributions of this study can be summarized as follows: 1) Estimation of nonlinear I-AVR instead of a constant value, 2) Investigation of the transient response of LVQ, aortic resistance, AV orifice area, and opening/closing angle in the CVS, 3) Prediction of instantaneous CO, 4) Development of an easily adaptable framework for incorporating noninvasive measurements through the proposed model-based CVS, and 5) Introduction of an adjustable I-AVR using a combination of EKF and CNN algorithms. By integrating noninvasive measurements into the CNN, we can observe the transient behavior of LVQ and I-AVR values. The subsequent section provides a detailed description of the model-based estimation algorithm, which utilizes the proposed CNN and integrates mathematical modeling with a deep learning approach. This novel approach offers valuable insights into the dynamic behavior of cardiovascular parameters and enhances the accuracy of I-AVR estimation.

4.3 Model Based Approach

The primary aim of this study is to develop a hemodynamic model-based framework for estimating instantaneous AV resistance in both normal and abnormal AV conditions. In this section, we will introduce the I-AVR model within the CVS and provide detailed descriptions of the mathematical model concerning the CVPs and physiological signals. Our previous study serves as the foundation for the model-based approach to the I-AVR [92].

To facilitate a better understanding of the proposed method, we'll present a functional block diagram illustrating the integration of the CNN with the conditioned AV models. We will elaborate on the stages involved in preparing the training and test datasets, which will include representations of both normal and AS cases. Emphasis is placed on the use of the hMCL for in-vitro measurements to condition the CV states. Lastly, we will depict the optimal CNN architecture, achieved through hyper-parameter optimization that accurately estimates the residue of the I-AVR.

4.3.1 The Proposed I-AVR Estimator Design

In our previous research, we have presented a leaflet dynamic model based on a nonlinear second order system, which allows for the computation of the I-AVR

using the parameters listed in Table 4.1. However, it is important to note that the resulting calculated CPs obtained through in vitro testing may exhibit variations due to the presence of nonlinearities. These inconsistencies can arise from differences in the mechanical resistance and capacitance of tanks or pipelines [117]. Furthermore, the physiology of the CVS can vary among individuals, even within the same person, leading to differences in physiological signals. To address these challenges and minimize any residual discrepancies between the real and estimated I-AVR, we propose a novel methodology which is depicted in Figure 4.1.

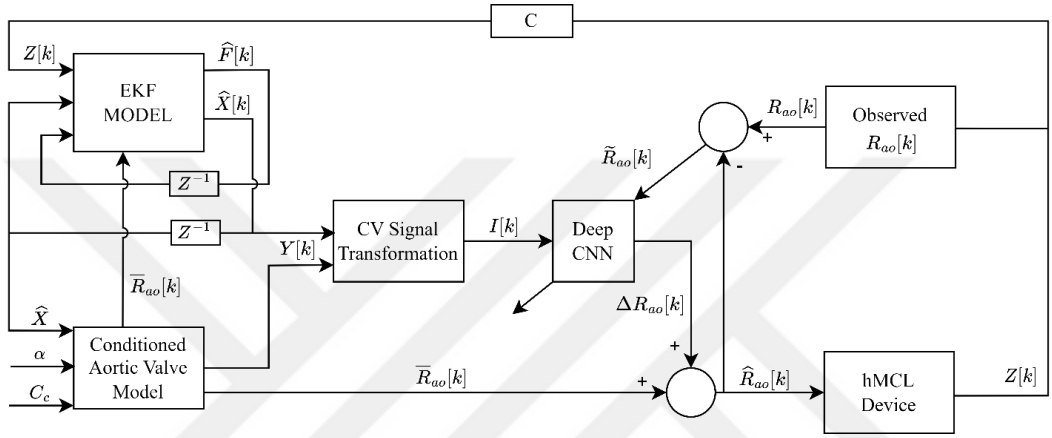


Figure 4.1 The proposed estimation algorithm

The proposed estimation algorithm comprises two main components: the computation of the conditioned AV-induced resistance ($\bar{R}_{ao}[k]$) and the deep CNN based resistance residue rate ($\Delta R_{ao}[k]$). These two resistances together form the estimated I-AVR to determine the correct resistance value through the use of the hMCL device. The proposed EKF model generates the physiological signals ($\hat{X}[k]$) using $\bar{R}_{ao}[k]$ and feeds these signals into the CV Signals Transformation unit (CVST). The conditioned AV model produces critical parameters $Y[k]$ related to the conditioned AV model. The outputs from both the conditioned AV and the EKF model are inputted into the CVST to enhance the training dataset. The deep CNN computes the residue rate ($\Delta R_{ao}[k]$), which is added to (($\bar{R}_{ao}[k]$). The resulting sum represents the estimated I-AVR ($\hat{R}_{ao}[k]$), which is then utilized in conjunction with the hMCL device.

4.3.2 The Instantaneous Aortic Valve Resistance Integrated Cardiovascular Model

In our prior study, we developed an instantaneous aortic valve model coupling both diastole and systole phase of the heart cycle [92]. Figure 4.2 illustrates a visual depiction of the anatomical structure and analogue model of our AV.

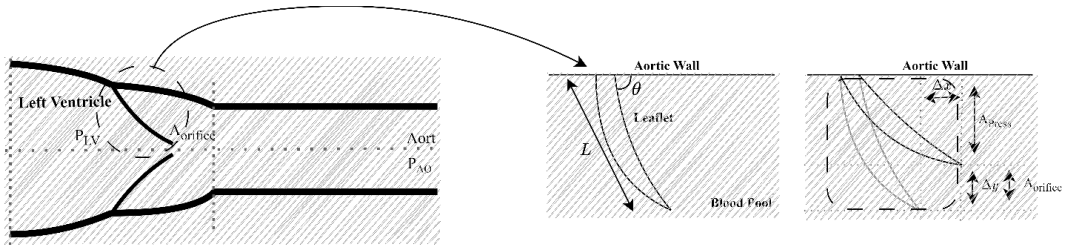


Figure 4.2 Aortic valve model [92]

The anatomy of the AV structure is depicted between the left ventricle and the aorta. The leaflets is assumed to be constant length L and $\theta(\zeta)$ is the opening angle which equals to 45° at initial condition ($\gamma = 45°$). The instantaneous aortic valve resistance (I-AVR) is generated from the translation motion of the leaflets which is given by

$$\ddot{\zeta} = \zeta \left[\frac{-s(\zeta, \alpha, \theta)}{m}\right] - \dot{\zeta} \left[\frac{c_c}{m}\right] + \Delta F \frac{1}{m} \tag{4.1}$$

where $s(\zeta, \alpha, \theta)$ and c_c are the dynamic leaflet stiffness and damper ratio, respectively. m, ζ and $\dot{\zeta}$ are the mass, translation deflection and rate of the leaflet, respectively. The dynamic leaflet stiffness is calculated as $s(\zeta, \alpha, \theta) = ([v_1\theta + v_2]Lv_a)/(\alpha \sin(\theta))$ with the coefficients of v_1, v_2, v_a satisfying physiological hemodynamics. Besides, α is the adjustable stiffness ratio which is utilized to condition AV states such as healthy, aortic stenosis and regurgitation. Let's assume that $\zeta' = \zeta/L$, ΔF is the acting force on the leaflets as follows:

$$\Delta F = \Delta P \, A_{press}(\zeta') \tag{4.2}$$

where $A_{total} = \pi L^2$ is the total translational area of the AV, $A_{press}(\zeta')$ is the translational area of the leaflet defined by $A_{press}(\zeta') = A_{total} - A_{orifice}(\zeta')$. The orifice area is computed as

$$A_{orifice}(\zeta') = \pi\left[\left(L - L\sqrt{\frac{1}{1-(1+\zeta')^2\sin^2(\gamma)} - (1+\zeta')^2}\right)\right]^2 \tag{4.3}$$

Using (4.2) and (4.3), we get

$$\Delta F = (P_{LV} - P_{AO})\,\pi L^2\left[\left(\frac{1}{1-(1+\zeta')^2\sin^2(\gamma)} - (1+\zeta')^2 - 2\sqrt{\frac{1}{1-(1+\zeta')^2\sin^2(\gamma)} - (1+\zeta')^2}\right)\right] \tag{4.4}$$

Using (4.4), the translational equation of motion of the leaflets is completed. In our prior study, the I-AVR formula has been established with the definition of

$$\bar{R}_{AO}(\zeta') = \sqrt{K_L\frac{\rho_b|P_{LV} - P_{AO}|}{A_{orifice}(\zeta')^2}} \tag{4.5}$$

where K_L leaflet's minor loss factor which equals to 1, ρ_b the blood density, P_{LV} and P_{AO} are the pressures across the valve in terms of LVP and AOP, respectively. Using (4.3) and (4.5), the instantaneous AV conductance (I-AVC) formula can be rewritten as

$$\bar{G}_{AO}(\zeta') = \frac{L\sqrt{\pi}\left(1 - \sqrt{\frac{1}{1-(1+\zeta')^2\sin^2(\gamma)} - (1+\zeta')^2}\right)}{\sqrt{|P_{LV} - P_{AO}|}\sqrt{K_L\rho_b}} \tag{4.6}$$

With $\bar{G}_{AO}(\zeta')$ is the conductance rate of AV satisfying $\bar{G}_{AO}(\zeta') = 1/\bar{R}_{AO}(\zeta')$. The proposed I-AVC is employed to construct the phase states of the cardiac cycle, encompassing both systole and diastole, through the utilization of (1).

Figure 4.3 depicts the in-silico CVS model that is based on the improved Mulier method enhanced by the substitution of the diode with the I-AVR [42].

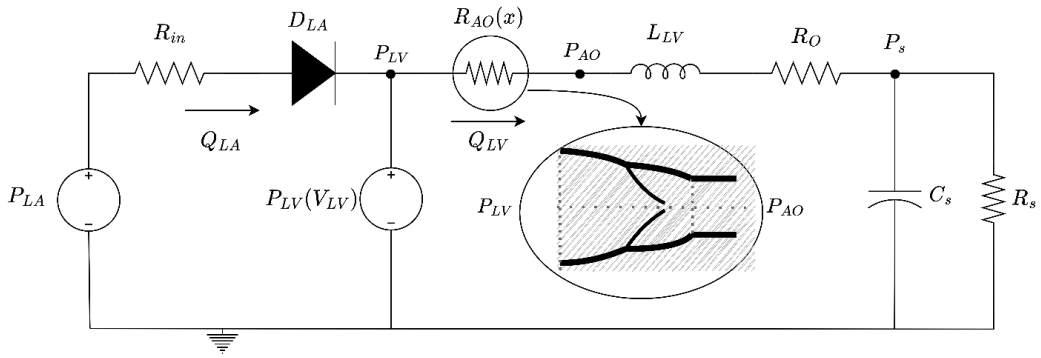


Figure 4.3 Instantaneous aortic resistance integrated cardiovascular analogue model

In Figure 4.3, P_{LA}, $P_{LV}(V_{LV})$ and $P_s(t)$ are the pressure generator of the left atrium (preload), left ventricle and total peripheral, respectively. D_{LA} is the diode when it is only opened at which P_{LA} is greater than P_{LV}, otherwise it is closed. R_{in}, R_0 and R_s are the constant mitral, aortic and total peripheral resistance. L_{LV} and C_s are the left ventricular inertia and total peripheral capacitance, respectively. The LVV induced generator ($P_{LV}(V_{LV})$) can be written as

$$P_{LV}(V_{LV}) = P_p(V_{LV}) + P_A(V_{LV}) \tag{4.7}$$

where $P_p(V_{LV}) = a(V_{LV}(t) - b)^2$ and $P_A(V_{LV}) = (cV_{LV}(t) - d)u(t)$ are passive and active pressure which are defined using some constants a, b, c, d satifying hemodynamic conditions. $u(t)$ is activation based normalized contractile function to be activated [42]. $u(t)$ is utilized to perform the periodical contraction with respect to the time duration of the systole and diastole phases. Incorporating volume-pressure relation using (4.7) gives us the left ventricular generator formula depending on LVV such as

$$P_{LV}(V_{LV}) = aV_{LV}^2 + V_{LV}(c\,f(t) - 2ab) + ab^2 - d\,u(t) \tag{4.8}$$

On the other hand, the AOP is defined from CVS analogue model as

$$P_{AO} = P_s + R_0 Q_{LV} \tag{4.9}$$

where Q_{LV} is the left ventricular flow rate. In order to define LAP, we utilize the following equation during diastole phase such as

$$P_{LA} = P_{LV} + R_{in}Q_{LA} \tag{4.10}$$

In (4.10), only Q_{LA} exists when P_{LA} is greater than P_{LV}. Now, the dynamic of the total stored LVV is written using (4.10) like

$$\dot{V}_{LV} = Q_{LV} \tag{4.11}$$

The LVV can now be reachable using (4.11). In order to obtain the equation of motion concerning $\dot{Q}_{LV}$, the conversation of mass law gives us

$$\begin{aligned}\dot{Q}_{LV} = V_{LV}\left[\frac{a\,V_{LV} - 2\,b\,a + c\,u(t)}{L_{LV}} + \frac{ab^2}{L_{LV}V_{LV}}\right] + Q_{LV}\left[\frac{-R_0}{L_{LV}} + \frac{-\bar{R}_{AO}(\zeta')}{L_{LV}}\right] \\ +P_s\left[\frac{-1}{L_{LV}}\right] + u(t)\left[\frac{-d}{L_{LV}}\right]\end{aligned} \tag{4.12}$$

It is vital to say that $P_{LV}(V_{LV})$ is rewritten using (4.8) in the first term of (4.12). The total peripheral dynamic can be written as

$$\dot{P}_s = P_s\left[\frac{-1}{R_sC_s}\right] + Q_{LV}\left[\frac{1}{C_s}\right] \tag{4.13}$$

4.3.3 The Discretization of the Cardiovascular System and Extended Kalman Filter Design

Let $x(t)$ be the state vector represented by

$$x(t) = [V_{LV}\ \ Q_{LV}\ \ P_s]^T \tag{4.14}$$

Then, the state space representation can be given by

$$\begin{aligned}\dot{x}(t) = A\big(\,x(t)\big)\,\zeta(t) + B\big(x(t)\big)\,u(t) + \eta_p \\ z = Cx(t) + \eta_m\end{aligned} \tag{4.15}$$

where η_p and η_m are process and measurement noise, respectively. The state matrices are

$$A(x(t)) = \begin{bmatrix} 0 & 1 & 0 \\ \left(\frac{ax_1(t) - 2\,b\,a + c\,u(t)}{L_{LV}} + \frac{ab^2}{L_{LV}x_1(t)}\right) & \left(\frac{-R_0}{L_{LV}} + \frac{-\bar{R}_{AO}(\zeta')}{L_{LV}}\right) & \left(\frac{-1}{L_{LV}}\right) \\ 0 & \left(\frac{1}{C_s}\right) & \left(\frac{-1}{R_s C_s}\right) \end{bmatrix} \tag{4.16}$$

$$B(x(t)) = \begin{bmatrix} 0 \\ \left(\frac{cx_1(t)}{L_{LV}} + \frac{-d}{L_{LV}}\right) \\ 0 \end{bmatrix} \tag{4.17}$$

In order to design the extended kalman filter, the state space representation is discretized using forward Euler approximation like

$$x(k+1) = x(k) + T\left[A(\,x(k))\,x(k) + B(x(k))u(k) + \eta_p\right] \tag{4.18}$$

Where T and k are the sampling period and discrete indice, respectively. Using (4.14-4.18), we get

$$\begin{gathered} x(k+1) = A_d(k)x(k) + B_d(k)u(k) + W_p \\ Z(k) = C\zeta + V_m \end{gathered} \tag{4.19}$$

where W_p and V_m are the discrete process and measurement noises, respectively. The discrete state space representation can be given by

$$A_d(k) = \begin{bmatrix} 1 & T & 0 \\ T\left(\frac{ax_1(k) - 2\,b\,a}{L_{LV}} + \frac{ab^2}{L_{LV}x_1(k)}\right) & 1 - T\left(\frac{-R_0}{L_{LV}} + \frac{-\bar{R}_{AO}(\zeta')}{L_{LV}}\right) & T\left(\frac{-1}{L_{LV}}\right) \\ 0 & T\left(\frac{1}{C_s}\right) & 1 - T\left(\frac{-1}{R_s C_s}\right) \end{bmatrix} \tag{4.20}$$

$$B_d(k) = \begin{bmatrix} 0 \\ T\left(\frac{x_1(k)c}{L_{LV}} - \frac{d}{L_{LV}}\right) \\ 0 \end{bmatrix} \tag{4.21}$$

Taking the linearization points at $x_1(0) = 80\,ml,\ x_2(0) = 0\frac{ml}{sec}, x_3(0) = 100\,mmHg$ satisfying physiological hemodynamic conditions. Then, the Jacobian matrices are computed yielding

$$A_d = \begin{bmatrix} 1 & T & 0 \\ T\left(\frac{2x_1(0)a - 2\,b\,a}{L_{LV}}\right) & 1 - T\left(\frac{-R_0}{L_{LV}} + \frac{-\bar{R}_{AO}(\zeta')}{L_{LV}}\right) & T\left(\frac{-1}{L_{LV}}\right) \\ 0 & T\left(\frac{1}{C_s}\right) & 1 - T\left(\frac{1}{R_s C_s}\right) \end{bmatrix} \tag{4.22}$$

$$B_d = \begin{bmatrix} 0 \\ T\left(\frac{x_1(0)c}{L_{LV}} - \frac{d}{L_{LV}}\right) \\ 0 \end{bmatrix} \tag{4.23}$$

Then, the Kalman configuration of the state variables in linearized form can be stated as

$$\begin{aligned} x(k+1) &= A_d x(k) + B_d u(k) + W_p \\ Z(k) &= Cx + V_m \end{aligned} \tag{4.24}$$

Now, let the covariance matrix of process noise be $Q = E\left[\eta_p \eta_p^T\right]$, then discrete noise can be written as

$$w_k = \int_0^T A_d \eta_p d\lambda_1 \tag{4.25}$$

Then, computing the discrete covariance matrix give us

$$\begin{aligned} E[w_k w_k^T] &= \int_0^T \int_0^T A_d E\left[\eta_p(\lambda_1)\eta_p(\lambda_1)^T\right] A_d^T d\lambda_1 d\lambda_2 \\ &= \int_0^T \int_0^T A_d Q \delta(\lambda_1 - \lambda_2) A_d^T \, d\lambda_1 d\lambda_2 \end{aligned} \tag{4.26}$$

Therefore, we can approximate the process noise into

$$Q_d = E[w_k w_k^T] = \int_0^T A_d Q A_d^T d\lambda_1 \tag{4.27}$$

The unknown noise signals are assumed to have zero mean with some covariance matrix estimates,

$$E\langle V_k\rangle = 0 \qquad var(V_k, V_l) = R_{dk}\delta_{kl}$$
$$E\langle W_k\rangle = 0 \qquad var(W_k, W_l) = Q_{dk}\delta_{kl} \tag{4.28}$$

where δ_{kl} is the delta dirac, i.e. zero for all $k \neq l$ and the cross covariance of V_k and W_k are zero. Then, the measurement vector can be defined by

$$z(k) = \left[P_{LV,h}(k)\ P_{AO,h}(k)\ P_{LA,h}(k)\ \ Q_{LV,h}(k)\right]^T \tag{4.29}$$

Where h is the hMCL measurement indice. For the extended kalman filter measurement vector, we get

$$Z(k) = \begin{bmatrix} 0 & 0 & 0 & 0 \\ 0 & 0 & 0 & 1 \\ 0 & 1 & 0 & \dfrac{-1}{R_0} \end{bmatrix} z(k) \tag{4.30}$$

It is noteworthy that we cannot directly reach the left ventricular chamber volume. Now, we can design prediction and updating sessions for the extended kalman filter. The prediction equations are

$$\hat{X}_k^- = A_d\hat{X}_{k-1}^+ + B_d u_{k-1}$$
$$F_k^- = A_d F_{k-1}^- A_d^T + Q_d \tag{4.31}$$

The update equations are

$$y_k = Z_k - H\hat{X}_k^-$$
$$K_k = F_k^- H^T(R_d + HP_k^- H^T)^{-1}$$
$$\hat{X}_k^+ = \hat{X}_k - K_k y_k \tag{4.32}$$
$$F_k^+ = (I - K_k H)F_k^-$$

Where H is the measurement matrix, F_k is the predicted error covariance, y_k is the measurement residual, K_k is kalman gain, Q_d and R_d are tuning parameters. We, now, have an EKF based CVS model for both the diastolic and systolic phases of the cardiac cycle. Subsequently, numerical simulations are conducted using the EKF as described in [118].

4.3.4 Input Transformation

The conditioned AV model, as illustrated in Figure 4.2, is constructed based on equations (4.1-4.6). This model incorporates various parameters including C_c α and $\hat{X}[k]$, which represent the damping ratio, adjustable stiffness factor, and physiological signals of the EKF model, respectively. By appropriately configuring these AV parameters, the model can simulate both healthy CV conditions and cases of AS, as detailed in the previous study [92].

By employing (4.30) with the stiffness and damping factor, the conditioned (AV) model produces the $\bar{R}_{ao}[k]$, which is subsequently incorporated into the EKF model. Additionally, the measurements obtained from the hMCL device are fed into the EKF model to generate estimation results. To enhance the comprehensiveness of the physiological data, the critical parameters are derived from the conditioned AV model by employing the following approach:

$$Y[k] = \left[\zeta[k]\ \dot{\zeta}[k]\ A[k]\ \theta[k]\ \bar{R}_{ao}[k]\right]^T \tag{4.33}$$

where $\zeta[k]$, $\dot{\zeta}[k]$, $A[k]$ and $\theta[k]$ are translation displacement of the leaflets, translation velocity of the leaflets, orifice area and opening angle of the AV, respectively.

In order to train the proposed deep CNN, a new input transformation is employed using (4.14) and (4.33). Then, the enriched form to feed the deep CNN is represented in (4.34).

$$I = \begin{bmatrix} \bar{R}_{AO} & \zeta & \dot{\zeta} & A & \theta & \hat{P}_{LV} & \hat{P}_{LA} & \hat{Q}_{LA} & (\hat{P}_{LV} - \hat{P}_{AO}) \\ \bar{R}_{AO} & \zeta^2 & \dot{\zeta}^2 & A & \theta^2 & \hat{P}_{LV}^2 & \hat{P}_{LA}^2 & \hat{Q}_{LA}^2 & (\hat{P}_{LV} - \hat{P}_{AO})^2 \\ \sqrt{\bar{R}_{AO}} & \sqrt{|\zeta|} & \sqrt{|\dot{\zeta}|} & \sqrt{|A|} & \cos(\theta) & \sqrt{\hat{P}_{LV}} & \sqrt{\hat{P}_{LA}} & \sqrt{|\hat{Q}_{LA}|} & \sqrt{|\hat{P}_{LV} - \hat{P}_{AO}|} \\ \frac{\bar{R}_{AO}}{\theta} & \zeta\,\theta & \dot{\zeta}\,\theta & A\,\theta & \sin(\theta) & \hat{P}_{LV}\,\hat{P}_{AO} & \hat{P}_{LV}\,\hat{P}_{LA} & \zeta\,\hat{Q}_{LA} & |\hat{P}_{LV} - \hat{P}_{AO}| \end{bmatrix} \tag{4.34}$$

In (4.34), the all parameters that affect the I-AVR are considered containing square root and square forms, in accordance with the LVQ equation [32]. The final row is constituted based on our prior approach presented in [92]. The opening angle is incorporated with specific input parameters that are the state variables of model based I-AVR representation.

4.3.5 Training and Test Dataset Preparation

The training and test datasets used in this study consist of results obtained from in-silico and in-vitro (hMCL) tests. The input data for training are generated using a hardware-in-the-loop structure implemented within the hMCL device, while the output data are directly obtained from hMCL measurements.

In the training dataset, the input variables are expressed by (4.34). These input data are collected from a STM32F746 microchip, where the EKF model is implemented. Real-time experiments are conducted on this chip for a duration of 10 seconds, enabling the entire algorithm to be contained on a single platform. Consequently, the training input and output feature sets can be simultaneously gathered. The sampling rate is set at 1000 Hz for the 10-second duration, resulting in 10,000 x 4 x 8 matrices to be used for training within the deep CNN.

For the test dataset, the hMCL device is operated for a 10-second period to collect validation data. Additionally, the Guyton reference data and the conditioned AV induced resistance are also employed to gather corresponding data that aligns with the real-time experiments.

4.3.6 Convolutional Neural Network

The proposed deep CNN is designed at eight layers. In the first place, we have added to convolutional layer with 10 units. Then, max pooling is used by following relu layer with the drop out ratio of 0.25. After that, we have added to convolutional layer with 20 units. Also, max pooling layer is applied on the outputs of these convolutional layers. Finally, relu and max pooling stages involved to feed every data to the fully connected layer. The fully connected layer includes two hidden layers with 10 neurons. In each stage, batch normalization layer is also used. The outcome of the proposed deep CNN is set to be the residue of the I-AVR ($\Delta R_{ao}(t)$).

4.3.6.1 Training Phase and Settings

To train the proposed deep CNN, we employ stochastic gradient descent with momentum and the ADAM optimizer to establish an appropriate relationship between the input and output variables [119], [120]. We set the maximum number of epochs to 1000 and fix the batch size at 16. This configuration is motivated by covering the present and past input data, which leverage the two set of 4x8 input matrix. The initial learning rate is set to 0.01, and validation is performed every 50

updates. The training of the proposed network is carried out using parallel processing, utilizing 16 processor cores. The cost function is minimized using these configurations.

Let the error be

$$\tilde{R}_{ao}[k] = R_{ao}[k] - \hat{R}_{ao}[k] \tag{4.35}$$

where $\tilde{R}_{ao}[k]$ is the error between observed $R_{ao}[k]$ and estimated $\hat{R}_{ao}[k]$. The observed I-AVR is calculated by

$$R_{ao}[k] = \frac{P_{LV}[k] - P_{AO}[k]}{Q_{LV}[k]} \tag{4.36}$$

Then, the cost function can be written using (4.35) and (4.36) like

$$J[k] = \frac{1}{2}\,\tilde{R}_{ao}[k]^2 \tag{4.37}$$

The deep CNN is trained to be minimized the error rate given in (4.35).

4.3.6.2 Test Phase

The entire experimentation process is conducted using a numerical hMCL platform build in Matlab 2022a and the hMCL device. For the numerical platform, Table 4.1 provides a comprehensive list of the constants and variables utilized, along with their respective values.

Table 4.1 Symbols table

Parameter	*Name*	*Value*	*Unit*
$\boldsymbol{m_{leaflet}}$	*Mass of leaflets*	$0.085*10^{-3}$	*kg*
$\boldsymbol{K_l}$	*Obstacle factor*	1	-
$\boldsymbol{L}$	*Leaflet Length*	0.011	*M*
$\boldsymbol{R_{in}}$	*Mitral Valve Resistance*	0.001	*mmHg.sec/ml*
$\boldsymbol{R_0}$	*Aortic Section Resistance*	0.04	*mmHg.sec/ml*

Table 4.1 Symbols table (continued)

R_s	*Systemic Resistance*	2	*mmHg.sec/ml*
C_s	*Systemic Capacitance*	1	*ml/mmHg*
L_{LV}	*Left Ventricular İnertia*	0.000416	*mmHg.sec²/ml*
ρ_l	*Liquid density for blood*	1005	*kg/m³*
v_1	*Spring fitting factor*	-4.2253	-
v_2	*Spring fitting factor*	235.323	-
v_3	*Spring fitting factor*	1000	-
v_4	*Spring fitting factor*	0.00001	-

The hMCL device, developed by the authors, serves as a means to validate the proposed estimator in a realistic "in-vitro" testing environment. The hMCL device allows for the manipulation of one controlled parameter while enabling the other parameters to vary freely, thus adhering to the principles of the FSM. This mechanism establishes the relationship between preload and CO, whereby an increase in the LVP due to increased blood volume influences ventricular contractility. In our hMCL device, we verify both ventricular contractility and the FSM by utilizing maximum and minimum reference signals for LVV. This approach ensures more accurate and realistic time responses of the CVS.

The trained deep CNN is implemented on a computer, and numerical results are tested using this network. For the in-vitro testing phase using the hMCL, all the coefficients associated with the deep CNN layers are reconstructed on an STM32F746 microprocessor. Figure 4.4 illustrates the validation and testing phases of the proposed estimator.

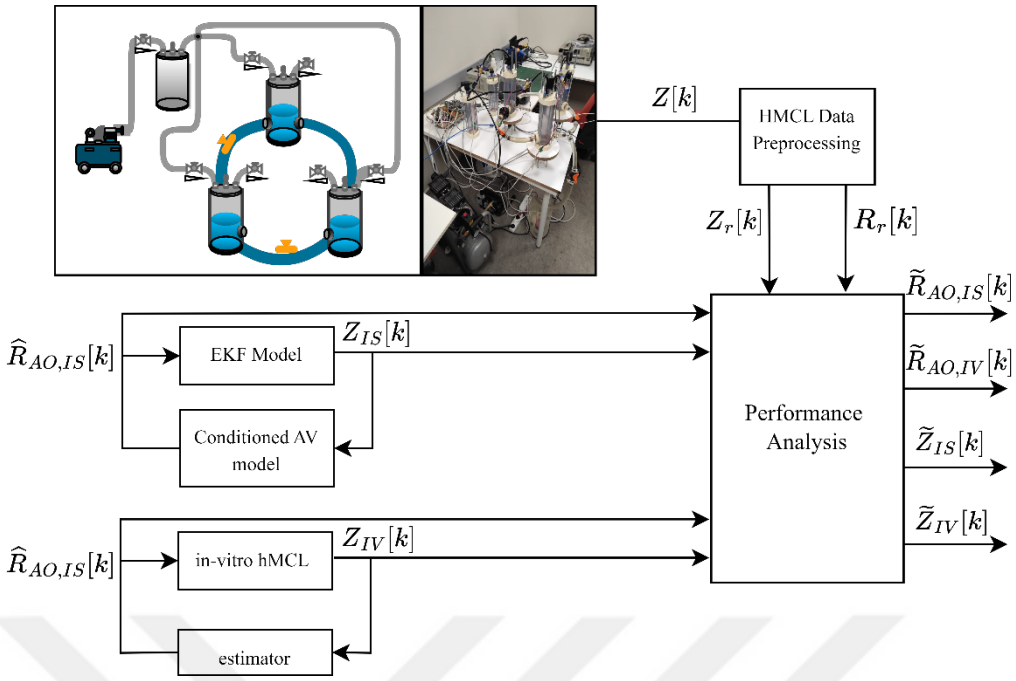


Figure 4.4 The validation procedures for the proposed estimator

At the beginning of the validation process, the hMCL device is run to generate through in vitro testing data $Z[k]$. Using preprocessing though these data, we get the reference measurements for physiological signals ($Z_r[k]$) and I-AVR ($R_r[k]$) values which are considered as golden standard for this study. There are two test results obtained from both the real hMCL experiments and the numerical hMCL setup built in Matlab 2022a. Both phases are employed to generate the physiological signals ($Z_{iv}[k]$ *and* $Z_{is}[k]$) and I-AVR ($\hat{R}_{AO,iv}[k]$ *and* $\hat{R}_{AO,is}[k]$) values. The root mean square results contains physiological signal ($\tilde{Z}_j$) and resistance ($\tilde{R}_{AO,j}$) one where j is either in silico or in vitro testing error.

4.4 Results

In this study, we conduct experiments using both the Matlab 2022a Simulink Platform and the hMCL device. The obtained results from numerical simulations and real-time experiments are compared and validated, considering both the I-AVR and the numerical outputs obtained using the proposed deep CNN.

Firstly, we perform numerical simulations and hMCL experiments to demonstrate the results for the pressures, flow rate, and aortic resistance of the CVS in healthy cases. Specifically, we evaluate the physiological behavior of the LVQ to validate

both the numerical simulations and the real-time experiments conducted using the hMCL device.

Secondly, we assess the proposed method under AS conditions to investigate the residue in the I-AVR in relation to AOP, LVP, and LVQ. Additionally, we conduct an analysis of the parameters of the model-based I-AVR to elucidate its internal characteristics in both healthy and AS cases.

Figure 4.5 illustrates the results of the physiological signals, such as LVP, LVQ, AOP, and I-AVC values, for the normal case.

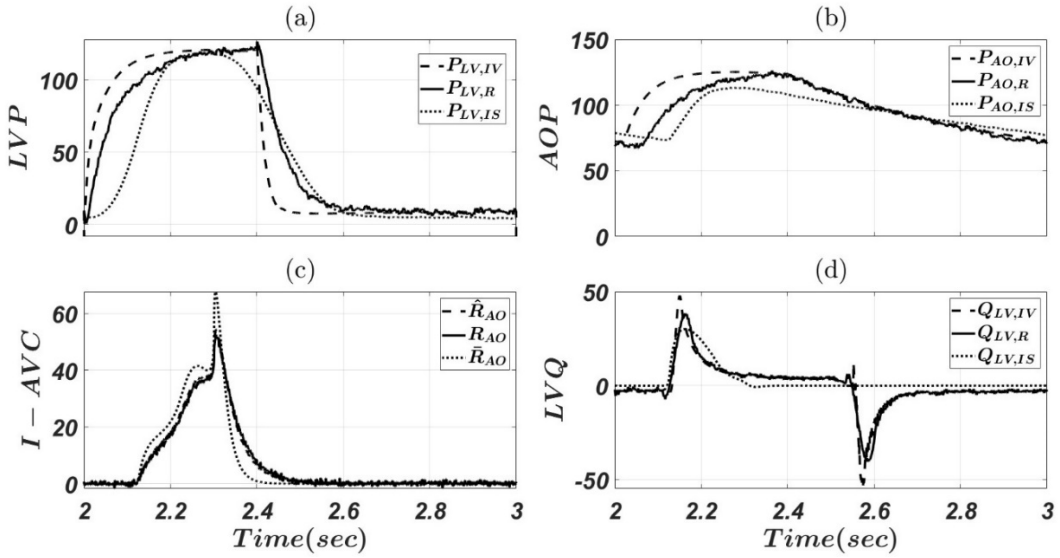


Figure 4.5 The results of LVP, AOP, I-AVC and LVQ in healthy case

Figure 4.5 provides a comprehensive analysis of the results, showcasing a comparison of various measurements and models. Figure 4.5a and 4.5b present the comparisons of LVP and AOP, respectively. The measurements include in-silico (IS), in-vitro (IV), and reference in-vitro (R-IV) results.

For LVP, the IV and R-IV measurements exhibit the closest agreement, with an error rate of 4.45±2.95%. The IS and R-IV show a slightly higher error rate of 6.02±3.72%. Similar patterns are observed for AOP, with error rates of 9.8±6.76% and 3.41±4.84% between the IS and R-IV, and between the IV and R-IV, respectively.

In Figure 4.5c, the comparison of the I-AVC is presented between $\hat{G}_{ao}$, G_{ao}, and $\bar{G}_{ao}$. The $\bar{G}_{ao}$ values demonstrate smooth patterns with the lowest value at the end of the systole phase. However, the $\hat{G}_{ao}$ and G_{ao} results indicate slightly lower I-

AVC compared to the $\bar{G}_{ao}$. The error rates are 0.2±0.83% and 0.06±0.21% between $\bar{G}_{ao}$ and G_{ao}, and between G_{ao} and $\hat{G}_{ao}$, respectively.

In Figure 4.5d, the LVQ is depicted in terms of real-time and numerical results. The IV and R-IV measurements show the closest results, with an error rate of 4.24±2.94%. The IS results align well with the IV and R-IV measurements, showing an error rate of 8.38±4.37%. However, the IV results deviate from the Guyton reference data for LVQ, resulting in an error rate of 9.25±6.16%.

The results obtained from the AS case are demonstrated in Figure 4.6.

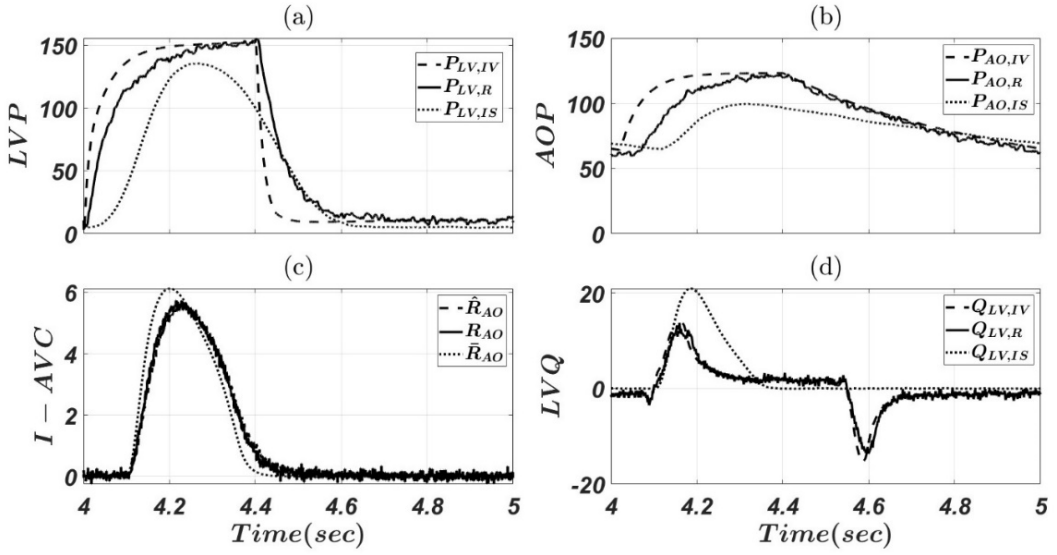


Figure 4.6 The results of LVP and AOP, I-AVC and LVQ in aortic stenosis case

Figure 4.6 illustrates the results obtained for AS case, using the same parameters as in Figure 4.5. In Figure 4.6a, Figure 4.6b, and Figure 4.6c, the LVP and PAO exhibit an increase, while the LVQ and I-AVC decreases compared to the healthy case.

For the LVP, the error rate between the IV and R-IV measurements is 6.63±4.81%, whereas for the IS and R-IV measurements, it is 9.07±5.81%. In Figure 4.6b, the error rate between the IV and R-IV measurements is computed as 4.19±2.41%, while for the IS and R-IV measurements, it is 8.22±3.97%.

The results of the $\bar{G}_{ao}$ show a decrease to 6, but the G_{ao} and $\hat{G}_{ao}$ measurements are lower than the $\bar{G}_{ao}$ one. The error rate between the G_{ao} and $\hat{G}_{ao}$ measurements is 0.12±0.05%.

In Figure 4.6d, the LVQ measurements obtained from the IV is closer to the healthy case. The IS and R-IV measurements also exhibit similarity to each other compared

to the healthy case, with an error value of 2.83±1.35%. However, a comparison with the Guyton reference LVQ is not included as there is no specific criteria available in the literature for aortic stenosis-induced LVQ.

After these tasks are performed, the critical parameters of the conditioned AV model are further analyzed to investigate the difference between the healthy and AS case. Figure 4.7 demonstrates the results in terms of ζ, $\dot{\zeta}$, θ and A signals.

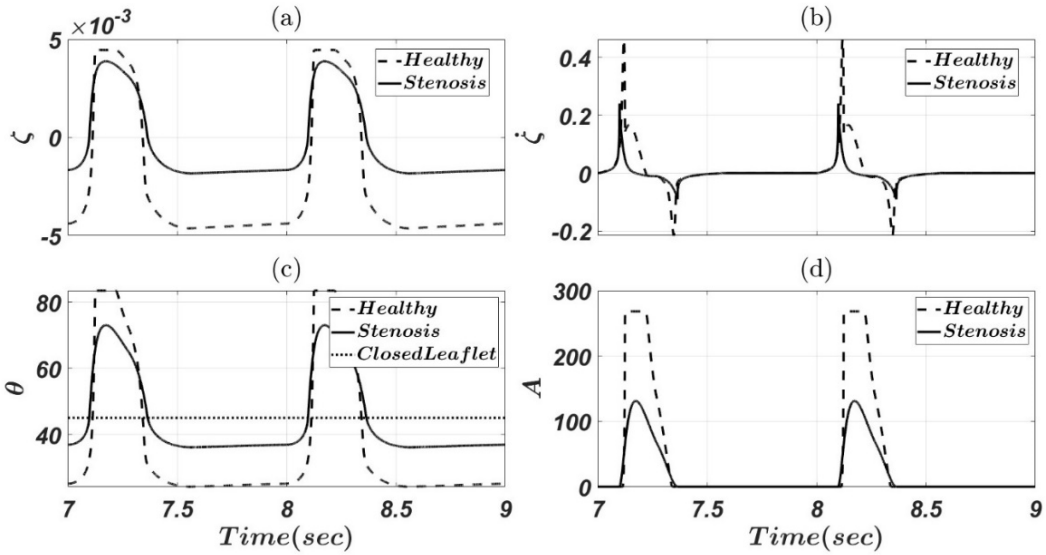


Figure 4.7 The results of $x, \zeta, \dot{\zeta}, \theta$ and A on both the healthy and AS case

Figure 4.7 provides a visual comparison of the time responses between the conditioned AV model for the healthy and AS cases. The translational displacement (Figure 4.7a), velocity (Figure 4.7b), opening angle (Figure 4.7c), and orifice area (Figure 4.7d) are analyzed to elucidate the observed differences.

In both cases, the amplitude of the time responses is reduced due to the decreased I-AVC. Specifically, for the translational displacement, the healthy case exhibits a range of -4.84 to 4.67 millimeters, while the AS case shows a range of -1.97 to 3.88 millimeters, as the LVP and AOP are increased to maintain the LVQ.

In Figure 4.7b, the leaflet velocity shows a single peak in the AS case, while it is uniformly distributed in the healthy case, with a significant reduction observed in the AS case. Similarly, the opening angle and orifice area also experience a decrease of more than half of their total amplitude values in the AS case compared to the healthy case.

The performance of the proposed estimator is also analyzed incorporating the pressure-volume diagram of the left ventricle which is given in Figure 4.8.

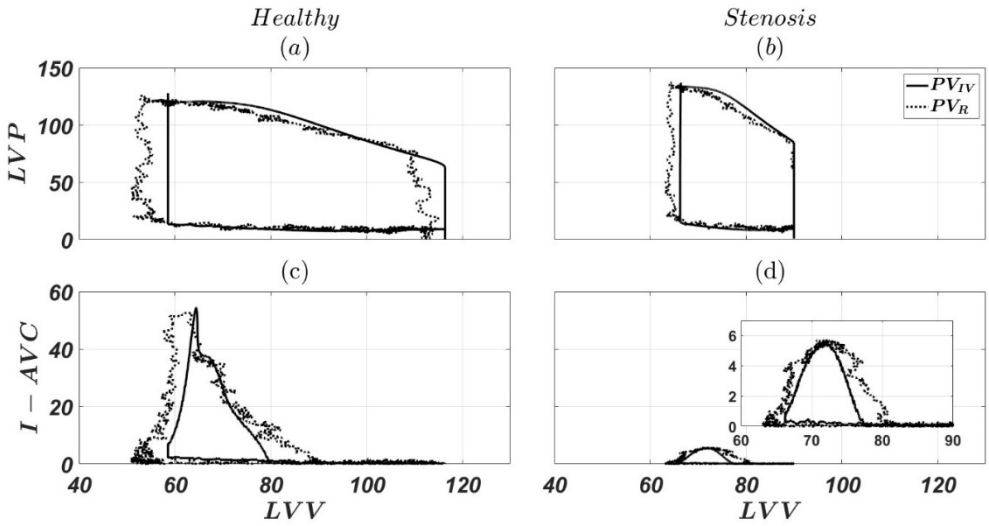


Figure 4.8 The results of pressure-volume relation on both healthy and aortic stenosis case

Figure 4.8 presents a comparison of the pressure-volume diagram and I-AVC responses between the healthy and aortic stenosis (AS) conditions. Consistent with physiological principles, AS results in an increase in the LVP and a decrease in the LVV. Furthermore, AS causes an elevation in the maximum elastance of the left ventricle, as evidenced by the decreased I-AVC values. Specifically, in the healthy condition, I-AVCs are observed to reach a maximum value of 57.51 *ml/(mmHg.sec)*, whereas in the AS case, they are reduced to 5.82 *ml/(mmHg.sec)*. Both the reference (PV_R) and proposed estimator (PV_{IV}) yield similar results in both the healthy and AS conditions.

4.5 Discussion

This study presents a novel approach for estimating I-AVR by integrating a conditioned AV model with the D-CNN which is optimized using hyper parameter tuning. To achieve this objective, we enhance our previous work by developing a comprehensive framework capable of capturing the personalized and nonlinear intricacies derived from both noninvasive and invasive measurements. The proposed algorithm is employed to obtain the transient response of LVQ and I-

AVR, and its validity is assessed through in vitro experiments. Nevertheless, there remain several aspects that warrant further investigation and discussion.

The proposed CNN estimator is based on the conditioned AV model, which enables the generation of a model-based I-AVR. By focusing on minimizing the residue between noninvasive measurements and the model, the CNN estimator aims to improve its performance and reduce the discrepancy between the estimated and real I-AVR values. In contrast to existing literature, the input for the CNN is transformed from a 1D vector to a 2D representation by incorporating excitation inputs derived from the conditioned AV model using the EKF. This transformation enhances the suitability of the input vector for capturing the physiological characteristics of CVPs, including I-AVR. Our previous study has unveiled previously unreported but significant features of the AV, such as the opening/closing angle (θ), leaflet translation displacement (ζ), and its rate ($\dot{\zeta}$). Incorporating these dynamic physiological features improves the estimation outcomes, particularly in the transient response of CVPs, which is valuable for predicting CV conditions like AS and regurgitation. The proposed CNN configuration enhances the conditioned AV dynamics and establishes a framework for a generalized prediction algorithm, as the model-based AV already encompasses the primary physiological components. The proposed CNN is solely utilized for extracting the underlying mechanism of CVS, including the generation of patient-specific data.

The estimation of CO involves a strong correlation between Guyton reference data, yielding an error rate of 0.23±0.52% for the healthy case, obtained by varying the heart rate from 60 to 120 bpm [94]. However, when conducting in vitro tests using only the conditioned AV model, the error rate increases to 5.62±4.71%, indicating insufficient generalizability for I-AVR estimation. Nevertheless, the proposed CNN estimator demonstrates improved performance by reducing the residue, resulting in an error rate of 3.41±4.84% between the real and estimated I-AVR in the healthy case. In the AS case, the proposed CNN estimator achieves an error rate of 2.83±1.35%, while the sole use of the conditioned AV algorithm results in an error rate of 3.51±4.66%. It is important to note that meaningful outcomes are not solely achieved through in vitro testing using the conditioned AV model from our previous

study. However, the proposed CNN estimator algorithm exhibits high performance, particularly in predicting and estimating CO values.

The proposed method makes an important contribution by incorporating not only physiological signals such as LVP, AOP, and LVQ, but also the I-AVR in order to estimate the transient responses of the CVS such as LVQ and CO. It should be emphasized that the dynamic behavior of the CVS is determined by critical CV parameters, specifically resistance and capacitance values, which influence the generation of physiological signals within the CVS. Relying solely on CVS signals for estimation may not yield reliable results due to individual variations. Previous studies have overlooked this interdependence due to the absence of the AV model. However, in this study, we propose the integration of both the conditioned AV model and the deep CNN architecture to obtain more realistic and comprehensive results related to the estimation of vital cardiovascular signals such as CO and LVQ.

An important aspect of discussion regarding the performance of the proposed CNN estimator is the inclusion of an adjustable parameter feeding mechanism. In Figure 4.1, the EKF model is executed using real measurements of LVP, AOP, and LAP obtained from in vitro testing. Consequently, the EKF generates physiological signals that are utilized for input transformation. In this in silico setup, it is possible to substitute any model-based signal with the corresponding real physiological signal, potentially leading to improved performance in the estimation and prediction of CO and I-AVR. Previous studies have relied on noninvasive measurements such as AOP or end-systole pressure of the LV, which can be easily integrated into the proposed CNN estimator algorithm by bypassing the EKF signal pathways [107], [108], [113], [114]. Thus, the proposed methodology not only offers enhanced estimation of I-AVR but also provides adjustable pathways for physiological signals, allowing validation of different scenarios or patient-specific conditions.

4.6 Conclusion

This paper proposed a hybrid approach for estimating the I-AVR using a CNN based on a model-based framework. The proposed method combined "in-silico" and "in-vitro" measurements to capture the dynamic response of cardiovascular parameters during the entire cardiac cycle. The input of the network was transformed from 1D into 2D using both "in-silico" and noninvasive measurements,

which produced rich excitation input for an efficient deep learning. The I-AVR was generated using a conditioned AV model, which extracts CVPs that could not be measured noninvasively. The CNN predicted the complete the I-AVR to minimize the residue between the I-AVR obtained from the conditioned AV model and the "in-vitro" measurements. To validate the measured the I-AVR in a more realistic condition, a hybrid mock circulatory loop (hMCL) was utilized in an "in-vitro" test, simulating both healthy and AS conditions by incorporating human, "in-silico," and "in-vitro" data.

Initially, the I-AVR values from the conditioned AV model were lower than those measured by the hMCL. However, the proposed CNN corrected this residue with an error rate of 0.3±0.12%. The left ventricular flow rate (LVQ) measured by the hMCL aligned with the Guyton reference data. In AS cases, an increased I-AVR led to elevated left ventricular pressure (LVP), decreased aortic pressure, and reduced LVQ. The validation rates for LVQ achieved error rates of 3.41±4.84% and 2.83±1.35% for healthy and AS cases, respectively. For CO estimation, there existed a strong correlation between Guyton reference data with an error rate of 0.23±0.52% for the healthy case, obtained by different the heart rate from 60 to 120 bpm.

By integrating noninvasive measurements into the proposed CNN estimator, we can now observe the LVQ, which enables us to gain valuable insights into its transient response. The estimation of the I-AVR provides significant opportunities for assessing and guiding the development of effective treatment strategies for patients. Especially for the generalization on the physiological condition, the proposed CNN estimator is the best candidate to evaluate the any other physiological conditions in CVS. These findings present new possibilities for enhancing diagnostic accuracy and optimizing patient care.

5
A NOVEL FRAMEWORK TO DIAGNOSE CARDIOVASCULAR DISEASES USING PHYSIOLOGICAL CONSCIOUS DEEP NEURAL NETWORKS

5.1 Abstract

This paper introduces a framework combining "in vitro" and "in silico" measurements to estimate cardiovascular (CV) parameters and diagnose CV conditions. The framework incorporates a modified autoencoder with a partially guided latent space, allowing for the inclusion of physiological consciousness into the deep neural network. The input to the net is driven by time-delayed CV signals, including pressures, flow rates, and CVP that cannot be directly measured used to learn the augmented latent space connectivity. The "critical" parameters include aortic resistance, mitral resistance, systemic resistance, and LV elastance to focus on tracking LV elastance deviation, MS, AS, and changes in SVR. The standard loss function of the autoencoder is constructed to predict the input signals and CVS parameters that are believed to play key roles in the studied cases. The labeled training datasets are generated from "in-silico" data obtained from a common CVS model. To validate the proposed models, a hybrid mock loop device is employed to collect corresponding CVS critical parameters and principal variables through in-vitro tests. The results of the in-vitro tests demonstrate reproduction of CVS signals with an error of less than 5.7%. When the net is used in closed-loop and critical parameters are externally perturbed, convergence of the CVS variables to those of the new condition is demonstrated. A diagnostics model exhibits the capability to classify the severity level of CVDs, with an overall F1 score of 94.76% over the wide range of cases studied.

5.2 Introducition

The CVS plays a crucial role in the human body, and the prevalence of CVDs, has increased due to lifestyle changes in the modern world. CVDs are responsible for appnsroximately one-third of all deaths globally [21]. To address this issue, extensive research has been conducted to develop models for diagnosing, treating,

and preventing CV abnormalities [60]. However, one of the challenges in analyzing, diagnosing, and treating CVD is the difficulty of non-invasively measuring CV signals from a live subject in real-time. The need to preserve the normal functioning of the CVS and comply with strict regulations imposed by authorities such as the FDA (Food and Drug Administration) and NCBI (National Center for Biotechnology Information) further complicates the process [61], [62]. Therefore, the development and utilization of effective CVS models are essential in addressing these challenges. These models can provide valuable insights into the functioning of the CVS, help in early detection of abnormalities, guide treatment strategies, and aid in the development of preventive measures.

Model-based simulations and experiments are conducted to generate synthetic CVS signals, which can be used for analyzing the CVS or emulating certain conditions for diagnostics and treatment of live subjects, such as AS, heart failure, and more [64], [78], [92], [121]. Although, “in-silico” tests offer complete knowledge of hemodynamic variables and parameters to interpret the nature of CVS, they are highly sensitive to assumptions made in mathematical modeling. That restricts model validity in a wide range of operation. To overcome such limitations of “in-silico” test, the “in-vitro” studies are conducted on physical analogous platforms for validation in silico models [73]. The mock loops (MCL) are an example of such devices filling the gap between clinical and engineering approaches. On the other hand, the hybrid mock loops (hMCL) enable us to access a richer set of CVS variables and parameters using either direct measurements or state estimation [73], [117]. This approach provides valuable insights into the behavior of the CVS and helps validate the assumptions made in mathematical models used for simulations. The combination of "in-silico" and "in-vitro" tests enhances our understanding of the CVS and aids in the development of more reliable diagnostic and treatment strategies.

The LV pumping oxygenated blood to the body is a very critical section of CVS. Any deviation of its operation may have significant effects on the heart and other organs. Its characteristics are modeled by the pressure, the flow rate variables, and its elastance parameter. Together with resistances of aortic and mitral valves, they play a critical role in understanding the conditions of the CVS [67]. The modeling of the overall systemic cycle is completed with basic elements of fluid resistances,

elastances and inertances in the closed-loop hemodynamic system. Although those signals coming from cyclic autonomous operation are periodic, they show dependency to a wide range of factors such as age, time, person to person, and other physiological conditions [88]. To accommodate such variations, different simplistic yet powerful models are suggested in various details, e.g., [78]. Experimental setups reproducing cardiac functions and in-vitro data are essential for clinical studies. Such a system validating the dynamic behavior using in vivo data obtained from MRA is given in [86].

Data-driven models utilize machine learning and statistical techniques to learn patterns and relationships from CV data. These models can be trained on large datasets and used to make predictions, classify diseases, or estimate physiological parameters. They offer flexibility in capturing complex dynamics and individual variations in the CVS provided thar a rich dataset is available. They have used data coming from both “in-silico” and “in-vitro” tests during the last couple of decades [18], [122], [123]. Such algorithms are utilized for the identification and prediction of the CVD and their treatment options to the experts [124].

In recent years, there have been many studies published related to estimation of CVS parameters especially for end-systolic left ventricular elastance (E_{LV}) and vascular resistance (R_{SYS}) which are the basic indicators watched for heart failure and systemic problems [114], [125]. Most of the studies focus on the estimation of the (E_{LV}) using the physiological data that can be measured invasively or noninvasively [34], [112], [126]. In general, the principal pressure and/or flow rate variables of CVS are considered in model development for heart failure or deprecated contractility, e.g [109]. When a complete state-space is not measurable, EKF methods are utilized for the measurement from real patients, some devices such as LVAD, or an artificial heart [111], [112], [116].

In this paper, the authors propose a novel framework based on a deep neural network (deepnet) for modeling, estimating key parameters of the CVS, and diagnosing certain CVDs. The deepnet is constructed by a novel autoencoder called the PCAE is trained on a dataset generated by a five-state "principal" variable CVS model. The dataset used for training the deepnet is produced from different operations, including a healthy heart condition with varying left ventricular elastance values, AS simulated by manipulating the aortic resistance, MS mimicked

by adjusting the mitral resistance, and varying SVR. By training the deepnet on this dataset, the authors aim to generalize the relationships between the CVS signals and these conditions. The autoencoder, which is a type of neural network architecture frequently used for dimensionality reduction and feature extraction, is modified to incorporate additional physiological signals into the latent space. These additional signals, referred to as "critical parameters," represent key CVS parameters. By including these critical parameters in the PCAE model, the authors not only create a model for the CVS but also estimate these important parameters. In addition to modeling and parameter estimation, the authors employ another deepnet model for the classification of healthy hearts and different severities of CVDs, including AS, MS, and SVR. This classification model utilizes the learned features from the PCAE model to classify the different CV conditions. Furthermore, the authors demonstrate that perturbing a critical parameter in the PCAE model results in the corresponding adjustments in the CVS principal variables. This indicates that the PCAE model is able to reproduce the behavior of the CVS based on the variation of critical parameters. Finally, all signals from the proposed framework: the principal variables, the critical parameters, the diagnostics, have been compared to “in-vitro” data obtained from the hMCL that authors developed [117].

5.3 Framework of the Artificial Cardiologist Assistant

The main objective of this research is to lay ground of a framework to analyze and predict the health condition of human CV system. In this section, we’ll start with analogous reference model with lumped parameters of CVS. Then, preparation of the training and the test datasets are discussed with some explanations of CV degradation of some structural and functional impairment of left ventricular. At the same time an hMCL device is utilized to regenerate relevant physiological signals and parameters for validation purposes. We propose an autoencoder enhanced by some CV physiological parameters for a better CVS modeling. A cost function is derived to enable learning of both CV pressure-volume signals and some critical parameters playing roles in CVD diagnostics.

5.3.1 Modelling CVS and Morbidity

There have been numerous models at varying degrees of complexity showing the internal hemodynamics in the heart. For the purpose of left ventricular, that is

considered to be the main driving part, study a reduce order lumped CVS model [78] has been taken as a reference model in this paper.

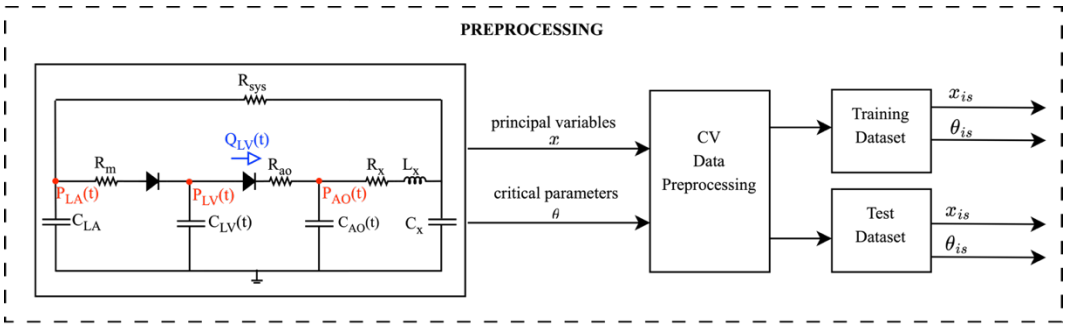


Figure 5.1. Dataset generation of CVS model development

The analogous electrical circuit shown in Figure 5.1 is written in state space as,

$$\dot{z} = A_c(t)z + B_c(t)p(z) \tag{5.1}$$

where $z = [P_{LV}(t) \quad P_{LA}(t) \quad P_{AP}(t) \quad P_{AO}(t) \quad Q_T(t)]^T$

$$A_c(t) = \begin{bmatrix} \frac{\dot{C}_{LV}(t)}{C_{LV}} & 0 & 0 & 0 & 0 \\ 0 & \frac{-1}{R_{sys}C_{LA}} & \frac{1}{R_{sys}C_{LA}} & 0 & 0 \\ 0 & \frac{1}{R_{sys}C_x} & \frac{-1}{R_{sys}C_x} & 0 & \frac{1}{C_x} \\ 0 & 0 & 0 & 0 & \frac{-1}{C_{AO}} \\ 0 & 0 & \frac{-1}{L_x} & \frac{1}{L_x} & \frac{-R_x}{L_x} \end{bmatrix} \tag{5.2}$$

$$B_c(t) = \begin{bmatrix} \frac{1}{C_{LV}(t)} & \frac{-1}{C_{LV}(t)} \\ \frac{-1}{C_{LA}} & 0 \\ 0 & 0 \\ 0 & \frac{1}{C_{LA}} \\ 0 & 0 \end{bmatrix}$$

$$p(z) = \begin{bmatrix} \frac{1}{R_M} r(z_2 - z_1) \\ \frac{1}{R_{AO}} r(z_1 - z_4) \end{bmatrix} \tag{5.3}$$

With the ramp signal modeling the switching functionality of diodes,

$$r(\eta) = \begin{cases} \eta, & if\ \eta \geq 0 \\ \eta, & if\ \eta < 0 \end{cases} \tag{5.4}$$

The four phases, isovolumic relaxation and contraction, ejection, and filling, of the left ventricular response can now be represented by this model (5.1) using the lumped parameters.

Table 5.1 CV health condition parameterization

	Name	**Value**					**Unit**
		N	**S1**	**S2**	**S3**	**S4**	
$\boldsymbol{R_{SYS}}$	Systemic Resistance	1.4	**1.7**	**2.0**	**2.3**	**2.5**	*mmHg.s/ml*
$\boldsymbol{R_{AO}}$	Aortic Section Resistance	0.0005	**0.001**	**0.01**	**0.1**	**0.6**	*mmHg.s/ml*
$\boldsymbol{R_M}$	Mitral Resistance	0.0003	**0.003**	**0.03**	**0.07**	**0.1**	*mmHg.s/ml*
$\boldsymbol{E_{max}}$	Maximum End-Systole Elastance	2.5	**2.2**	**1.9**	**1.7**	**1.4**	*ml/mmHg*
$\boldsymbol{R_C}$	Characteristic Resistance	0.04	0.04	0.04	0.04	0.04	*mmHg.s/ml*
$\boldsymbol{C_{LA}}$	Left Atrium Compliance	4.4	4.4	4.4	4.4	4.4	*ml/mmHg*
$\boldsymbol{C_{AO}}$	Aortic Compliance	0.08	0.08	0.08	0.08	0.08	*ml/mmHg*
$\boldsymbol{C_S}$	Systemic Compliance	1.33	1.33	1.33	1.33	1.33	*ml/mmHg*
$\boldsymbol{L_S}$	Inertance of blood in Aorta	0.0005	0.0005	0.0005	0.0005	0.0005	*ml/mmHg*

The emulation of healthy and morbidity conditions is accomplished by reflecting structural deformations on the lumped aortic, mitral, systemic resistances and contractility of the left ventricular elastance in four severity levels, named S1

through S4. The parametric ranges of these conditions that are defined by our study are shown in Table 5.1.

In Table 5.1, CVS principal variables of a person in healthy and different stages of disease conditions are parameterized. In healthy condition, the E_{max} parameter range is shown to be between 1-5 mmHg/ml interval [110]. In our study, the proposed in-silico model is tested between 1.4-2.5 mmHg/ml as in [78]. The ranges of abnormal cases of R_m and R_{sys} are selected according to the same study as well [78]. The R_{AO} values are taken from Iscan et al. studies [92] in which the time-varying aortic resistance is modeled in their study to represent the aortic regurgitation and stenosis cases. The last stage of the CVD demonstrates worst case condition (S4) for a given CV condition.

Therefore, the healthy condition is labeled as H_i when E_{max} value is taken from S_i^{th} column for $i = 1,2,3,4$ and the remaining parameters kept at their nominal values as shown in column N in Table 5.1. The AS severity level is labeled as AS_i when R_{AO} value is taken from the column S_i while the others kept at nominal values. Similarly, for MS and systemic resistance chance (SRC) conditions severity levels are labeled as MS_i and VSR_i by changing R_M and R_{SYS} from S_i^{th} column, respectively.

5.3.2 Generation of CV Physiological Dataset for Deep-Learning

In Figure 5.1, the CV dataset generation process using reference CVS models is shown. To obtain the reference time series of the principal signals and critical parameters with the labeled healthy and disease conditions of the aortic and MS SVR change and maximum elastance variation, the model is run with different parameter. A representative latent space variables during the dataset generation is depicted in Figure 5.2. These signals and the associated CV conditions are split into 30% test and 70% training datasets and stored during the preprocessing phase

The training data is produced by using these resistances and maximum elastance values in which each of them is changed at different times and time responses of CVS are obtained to identify mitral and AS, systemic vascular change and maximum elastance effect on CVP Each training set related to N, S1, S2, S3 and S4 for each condition is run within the period of 180 second with the sampling rate of 10Khz. After that, each condition is assigned to specific states defining the

diseases type of CVS. After that, the normalization process is applied to the whole data to improve autoencoder results. Due to time dependency of CVS, the best beats are selected to represent the specific disease and its levels by using state variables which is assigned to both healthy and disease conditions. Then, the whole generated data is split into test and training one at the rate of %30 and %70, respectively. The total training and test data indicating disease and healthy conditions are depicted in Table 5.2.

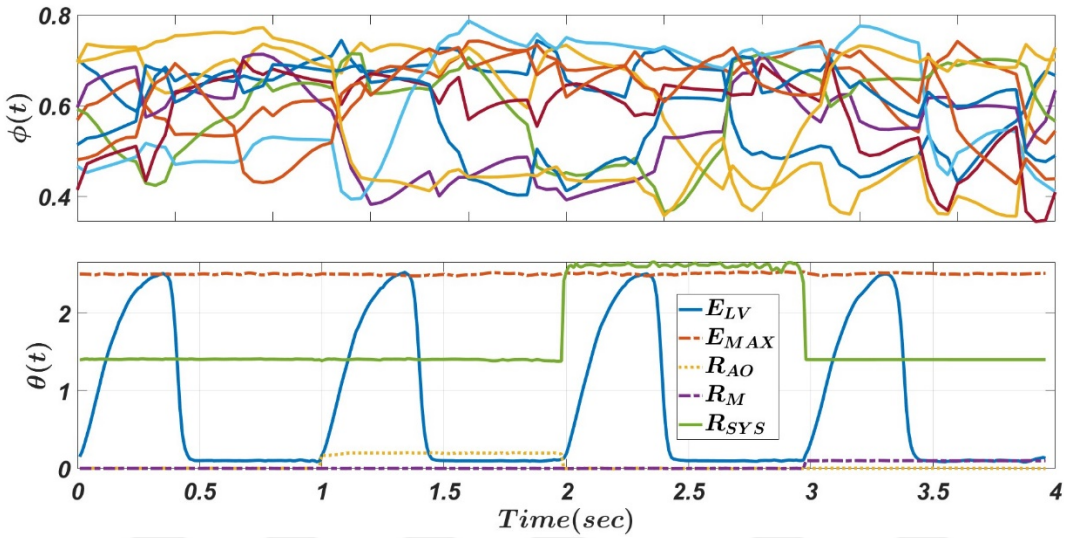


Figure 5.2. Latent variables during dataset generation

In Table 5.2, CV data is generated in beats, each representing one time history of heart circulation including complete systole and diastole phases. The hMCL device is set to a specific resistance and elastance values to simulate the targeted abnormalities. The in vitro data is collected at 1 kHz on the platform developed by authors [117]. It is important to notice that only the "in-silico" data is utilized during the training phase. Each of the training dataset is set to be 2,300 beats for each disease levels. The "in-silico" tests are performed for 1,000 synthetic beats for each case. Additionally, hMCL measurements are only used to validate the proposed PCAE model.

Each feature vector related to the principal variables and the critical parameter values are normalized between 0 and 1 by using physiological maximum and minimum values (e.g., P_{LV} is ranged between 0 and 200 mmHg, etc.).

Table 5.2 PCAE data slicing for training and valiadation

All Level	In Silico (PV)	In Silico (CP)	In Vitro (PV)	In Vitro (CP)	Total
Training Data	11,500 beats	11,500 beats	-	-	23,500 beats
Test Data	5,000 beats	5,000 beats			10,000 beats
Validation Data	-	-	1,200 beats	1,200 beats	2,400 beats
Total	16,500	16,500	1,200	1,200	35,400

Validation Tests	In Vitro (PV)	In Vitro (CP)	Total
Healthy Test	398 beats	398 beats	796 beats
Mitral Stenosis Test	154 beats	154 beats	308 beats
Aortic Stenosis Test	227 beats	227 beats	454 beats
E_{max} Change Test	168 beats	168 beats	336 beats
Systemic-Vascular Change Test	253 beats	253 beats	506 beats

The training and testing features contain both principal variables $x = (P_{lv}, P_{ao}, P_{la}, V_{lv}, Q_{lv})^T$ and critical parameter $\theta = \left(E_{lv}, E_{max}\ , R_{ao}, R_m, R_{sys}\right)^T$ sets in order to represent the targeted physiological properties related to normal and abnormal cases. The calculation of the critical parameter sets is done by using principal variables values at both "in-silico" and "in-vitro" experiments. In both experiments, normal and abnormal conditions are constructed by using Table 5.1 with the change of resistance and maximum elastance values. After that, the measurements of "in-silico" and "in-vitro" are achieved and assigned to specific cases for healthy and mitral, AS, vascular resistance and elastance changes abnormalities.

5.3.3 The PCAE Architecture for CVS

The backbone of the proposed framework is PCAE as shown in Figure 5.3. The PCAE is constructed by feedforward neural networks (NN) mapping the recurrent principal variables input space to the latent space in the encoder block and then

back to a prediction of the principal variables in the decoder block. The latent space is modified by the CVPs that cannot be measured non-invasively, including aortic (AR), mitral (MR) and systemic (SR) resistances, end systole (Emax) and time-varying elastance of left ventricle (TV-LVE). The latent space vector is used for analysis and diagnostics of targeted CVD conditions with an additional feedforward NN, called diagnostics model. The CVS abnormalities considered are the TV-LVE deviation, mitral (MS) and aortic (AS) stenosis and vascular resistance change (VRC). DL is achieved using "in-silico" generated dataset based on the models given in [78]. The mathematical model is conditioned in both healthy and abnormal cases.

The PCAE is shown, processing the principal variable vector,

$$x = (P_{lv}, P_{ao}, P_{la}, V_{lv}, Q_{lv})^T \tag{5.5}$$

with P_{lv}, P_{ao}, P_{la} the left ventricular, the aorta, the LAPs, V_{lv}, Q_{lv} the LVV and flow rate, respectively. at the input stage and generates the latent space internal $\phi(k) \in \mathbb{R}^{N_1}$ and external $\theta(k) \in \mathbb{R}^{N_2}$ vectors at its output. The external $\theta(k)$ vector enables injection of external physiologically conscious into the PCAE. The decoder block maps the latent space back to predictions of the principal CV variables.

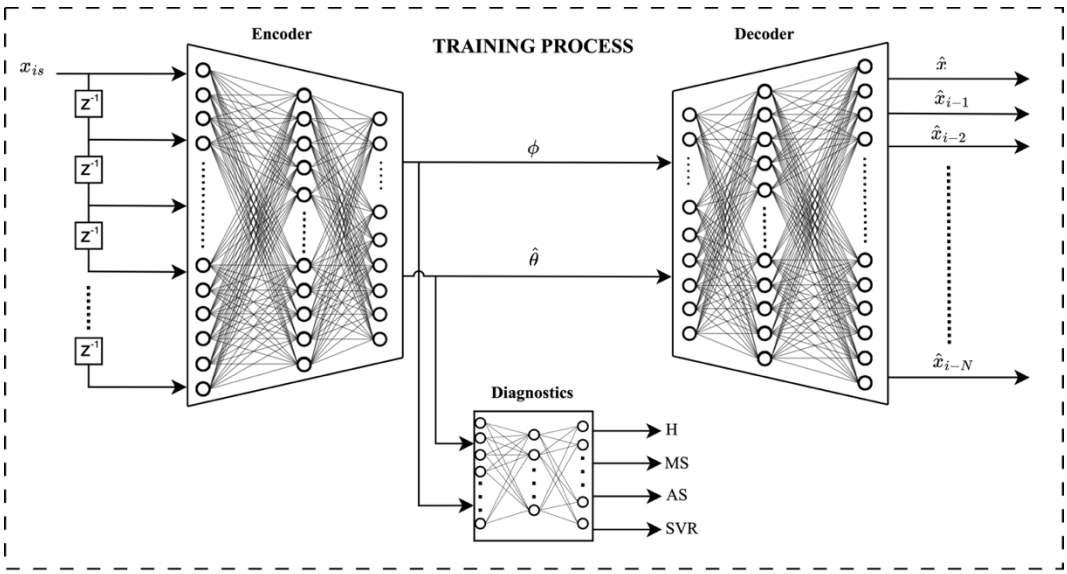


Figure 5.3. PCAE based CVD classification

Since both principal variables and critical CVS parameters are time-dependent a recurrent autoencoder is used in our modeling. According to physiological information, the average heart rate in a healthy person is in the range of 60 to 120

bpm which means that the proposed method includes 1000 to 2000 samples collected at 1 kHz [127] . So, the input vector should be increased by using delay operation like

$$X = \begin{bmatrix} x_{is}(k) \\ x_{is}(k-1) \\ \vdots \\ x_{is}(k-N) \end{bmatrix} \tag{5.6}$$

with N picked large enough to form a window to enable learning in time series.

After completing the preprocessing and data collection phase extended PCAE input vector X and focused parameters θ_{is} are made available for physiologically conscious learning process. The input X is predicted by autoencoder, θ_{is} injected into the loss function to steer some of the latent space neurons to select physiological parameters simultaneously.

Let error vectors be,

$$e_x = X - \hat{X}, \qquad e_\theta = \theta_{is} - \hat{\theta} \tag{5.7}$$

with e_x and e_θ the autoencoder prediction and critical parameter error vectors, respectively. In this study, we target critical parameters of interest.

$$\hat{\theta} = \left[\hat{E}_{LV}, \hat{E}_{MAX}, \hat{R}_{AO}, \hat{R}_{SYS}, \hat{R}_M\right]^T \tag{5.8}$$

to be estimated within the latent space.

The proposed augmented autoencoder model consists of two phases: encoder and decoder sections. The encoder maps the input vector to another one by using (5.9-5.11):

$$z^{(1)} = h^{(1)}\left(W^{(1)} X + b^{(1)}\right) \tag{5.9}$$

$$z^{(2)} = h^{(2)}\left(W^{(2)} z^{(1)} + b^{(2)}\right) \tag{5.10}$$

$$\gamma = h^{(3)}\left(W^{(3)} z^{(2)} + b^{(3)}\right) \triangleq f(X, \Theta_e) \tag{5.11}$$

where the superscript indicates the layer number, $W^{(i)}$ is the weight matrices and $b^{(i)}$ is the bias vector, $h^{(i)}$ is the activation function of i^{th} layer, Θ_e all learnable

encoder parameters. The encoder is constructed by a three hidden layer multi layer perceptron. The encoder output layer is split into internal $\boldsymbol{\phi}$ and external $\widehat{\boldsymbol{\theta}}$ fields.

$$\gamma = [\boldsymbol{\phi}^T \quad \widehat{\boldsymbol{\theta}}^T]^T \tag{5.12}$$

where $\boldsymbol{\phi}^T = [\phi_1 \ \phi_2 \dots \phi_m]$,$\widehat{\boldsymbol{\theta}}^T = [\hat{E}_{LV}\ \hat{E}_{max}\ \hat{R}_{AO}\ \hat{R}_{SYS}\ \hat{R}_M]$. The following decoder block is organized as,

$$z^{(4)} = h^{(4)}\left(W^{(4)}\,\gamma + b^{(4)}\right) \tag{5.13}$$

$$z^{(5)} = h^{(5)}\left(W^{(5)} z^{(4)} + b^{(5)}\right) \tag{5.14}$$

$$\hat{X} = h^{(6)}\left(W^{(6)}\, z^{(5)} + b^{(6)}\right) \triangleq g(\gamma, \Theta_d) = g \circ f(X, \Theta) \tag{5.15}$$

where $\hat{X}$ is the predicted principal variables, $z^{(i)}$ hidden layer output, $W^{(i)}$ and $b^{(i)}$ are i^{th} layer tunable weight and bias matrices, Θ_d all learnable decoder parameters and $\Theta = \{\Theta_e, \Theta_d\}$.

The cost function to train the autoencoder while guiding a subset of the latent space is defined as

$$J = \alpha_1 \frac{1}{N}\sum_{n=1}^{N} e_x^T e_x + \alpha_2 \frac{1}{N}\sum_{n=1}^{N} e_\theta^T e_\theta + \lambda * \ \Omega_{weights} + \beta * \ \Omega_{sparsity} \tag{5.16}$$

where N is the total number of training samples, α_1 and α_2 are the weights of variable prediction and parameter estimation processes, λ is the L2 regularization term and β is the sparsity regularization term, respectively. For the L2 regularization, we have,

$$\Omega_{weights} = \frac{1}{2}\sum_{l=1}^{L}\sum_{j=1}^{n_l}\sum_{i=1}^{k_l}\left(w_{ji}^{(l)}\right)^2 \tag{5.17}$$

with L, n_l, n_k the number of hidden layers, the number of neurons in the layer l, and the following layer, respectively. For the sparsity rate, the Kullback-Leibler divergence formula is used as in [128]:

$$\Omega_{sparsity} = \sum_{i=1}^{D^{(1,\ldots,6)}} \rho \, log\left(\frac{\rho}{\hat{\rho}}\right) + (1-\rho) \, log\left(\frac{1-\rho}{1-\hat{\rho}}\right) \tag{5.18}$$

where ρ is sparsity proportion rate value and $\hat{\rho}$ is the estimated average output function value. The $\hat{\rho}$ is calculated as

$$\hat{\rho}_i^{(l)} = \frac{1}{N}\sum_{j=1}^{N} z_i^{(l)} z_j^{(l-1)} \tag{5.19}$$

The cost function given in (5.16) is optimized using the scaled conjugate gradient method [73]. The total error value is also calculated by using the mean square error.

5.3.4 Diagnostics Model

The proposed framework includes another deepnet diagnostics model to predict and classify the CV health conditions including the severity level of abnormalities for the trained diseases. A multilayer perceptron model with a softmax layer is utilized to achieve these tasks for 16 classes of abnormalities which contains 4 healthy conditions with respect to critical parameter sets of input variables.

The diagnostics model input is taken from the latent space of PCAE,

$$\gamma = \left[\phi_1 \;\; \phi_2 \ldots \phi_m \;\; \hat{E}_{LV} \; \hat{E}_{max} \; \hat{R}_{AO} \; \hat{R}_{SYS} \; \hat{R}_M\right]^T \tag{5.20}$$

Its output is the healthy and disease condition levels of 16 classes. The output layer's softmax activation function is [129], then

$$\sigma(\vec{z})_i = \frac{e^{\vec{z}_i}}{\sum_{j=1}^{K=16} e^{\vec{z}_j}} \tag{5.21}$$

with $\sigma(\vec{z})_i$ the probability of i. The hidden layers use sigmoid activation functions, and the cross-entropy function is performed to train the network.

Each of the class probabilities are obtained from (5.20), then, the class which has maximum probability is assigned to 1 to represent the stage of both healthy and diseases conditions.

5.3.5 Use of PCAE for CVD Treatment

Once the PCAE is trained for the targeted abnormalities and healthy conditions, the critical parameters may be externally injected into the framework to observe their effects on the CVS principal variables. This mechanism enables an expert physician to tailor some treatment strategies targeting those critical parameters and analyze the CVS response. Total representation of closed loop PCAE is given in Figure 5.4.

After the training process, autoencoder output is feedback to its input and the network is put in a cyclic condition. At this stage the latent space parameter vector element(s) may be switched to a desired parameter $\theta^*(t)$. The cyclic autoencoder output converges to a different regimen that is correlated to the corresponding principal variable state, hence the effect of changing some of the critical parameters on CVS are observed in detail by a cardiologist.

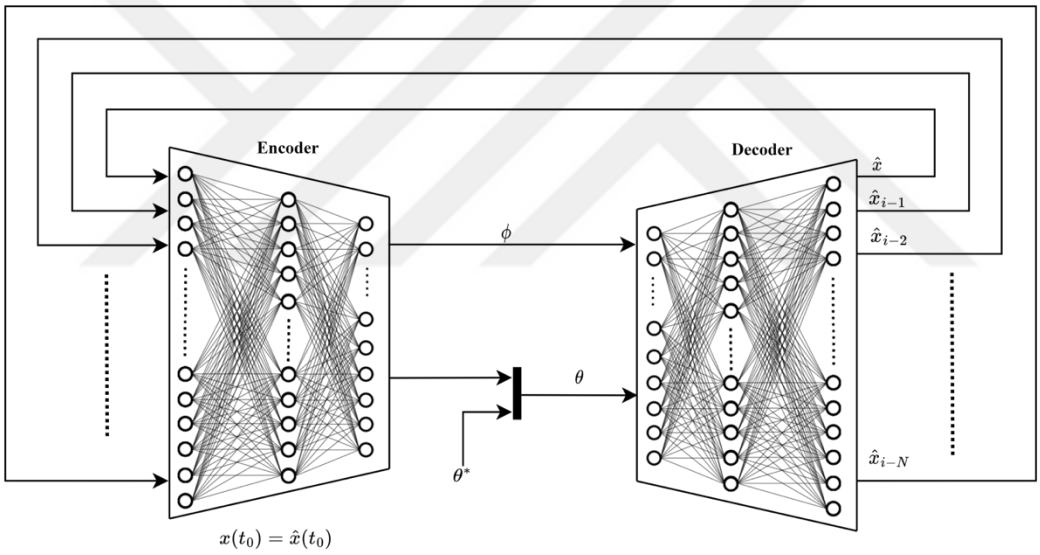


Figure 5.4. Closed loop PCAE operations

5.4 Illustrations

To demonstrate the capabilities of the proposed framework, we have first showed the training and test performances PCAE model driven by in-silico healthy, aortic and MS, and SVR deviation case datasets. Then, the PCAE model is validated on in-vitro tests. Then, the artificial cardiac assist model's performance is shown. Finally, we have shown PCAE CV model response to some select critical parameter changes, including E_{max}, R_{ao}, R_{sym}. Figure 5.5 demonstrates the overall performance analysis process applied for model assessment. All these simulations

resulted in the principal variables, critical parameters consistent with the literature and %94 F1 score accurately classify the selected diseases. $\{E_{lv}, E_{max}, R_{ao}, R_m, R_{sys}\}_{is}$ using (5.1) while the "in-vitro" tests are conducted to produce the same physiological dataset.x_{iv} and θ_{iv}. The trained PCAE driven by x_{is} predicts CV variables $\hat{x}_{OL}$ and parameters $\hat{\theta}_{OL}$. The processed in-vitro test outputs $\hat{x}_{iv}$ and $\hat{\theta}_{iv}$ are compared to model outputs in the performance analysis. The latent space vector $\hat{\gamma}_{OL}$ is utilized by the diagnostics model for the CVD classification with the outputs of four stages of each Healthy (H), MS, AS and SVR change conditions.

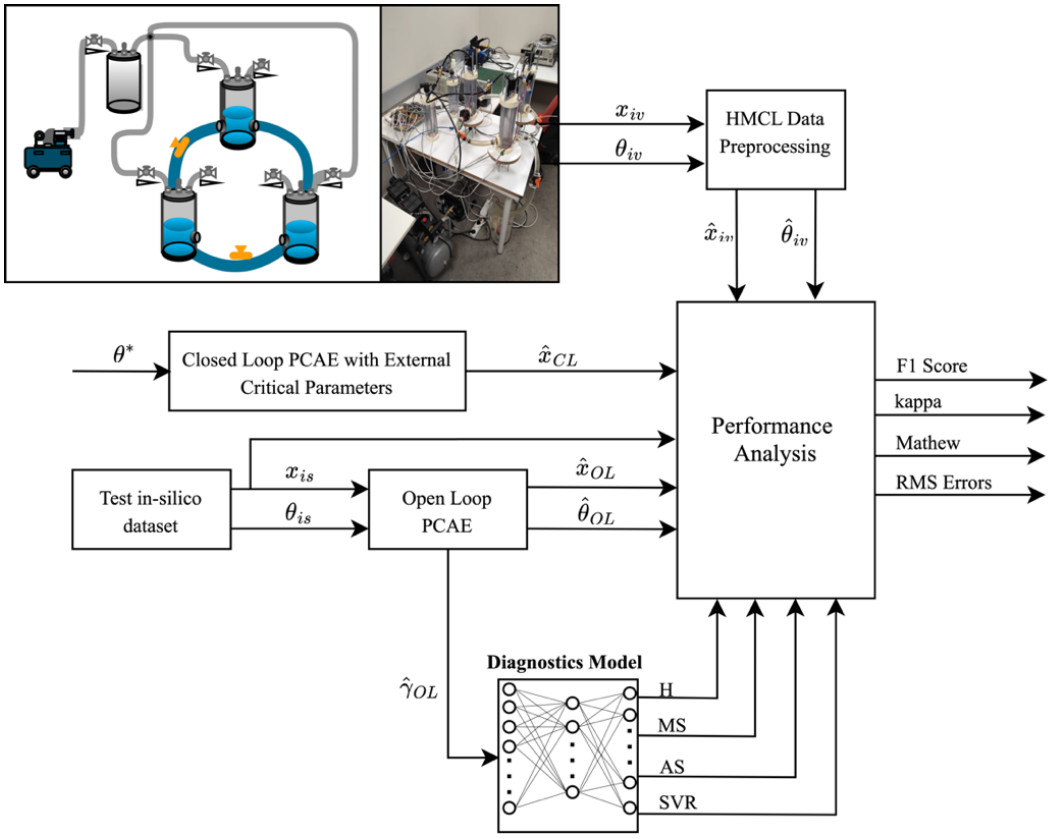


Figure 5.5. Validation processs of the proposed PCAE algorithm

5.4.1 PCAE Modelling Simulations

After experimenting with some of the hyper-parameters, we have reached satisfactory results when the encoder hidden layers of 200-120-15, and λ=1e-10, β=1e-12, ρ=1e-5, $\alpha_1 = 10, \alpha_2 = 1$ are selected.

The trained PCAE is able to match the in-silico data very closely for all of Heathy, AS, SYStemic resistance (SYS), MS cases as shown in the first columns for the

principal variables in Figure 5.6 and for the critical parameters in Figure 5.7. When the same CVS conditions are generated in-vitro tests PCAE responses are shown in the second columns in Figure 5.6 for the principal variables and in Figure 5.7 for the critical parameters. Although the physical limitations of hMCL device used showing some lag and noisy response for E_{lv}, Q_{LV}, E_{max} the remaining variables and parameters have resulted in anticipated signals.

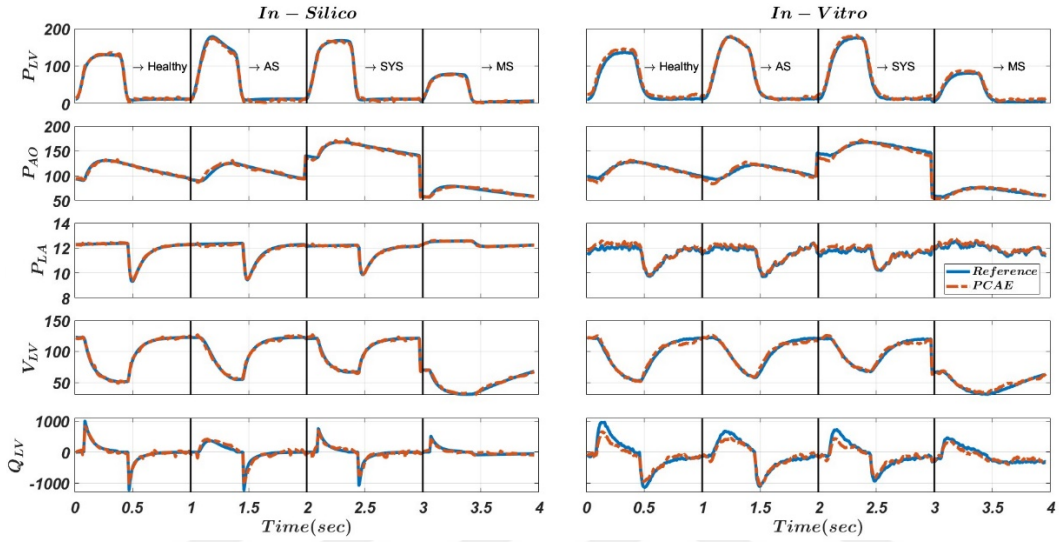


Figure 5.6. PCAE principal variables responses to in-silico model and in-vitro device [117]

In terms of the diseases cases, AS affects only the left ventricular pressure, the volume, and the flow rate at both "in-vitro" and "in-silico" data are in accordance with the physiological findings [116]. Vascular systemic resistance increment pulled up AOP to 150 mmHg but did not affect the $Q_{LV}(t)$ value in all cases. In the MS case, all of the pressures and volume values except $P_{LA}(t)$ are decreased in accordance with the physiological data [130]. Especially for $Q_{LV}(t)$ in diastole phase, highly sensitivity to transfer blood into the LV chamber can be seen.

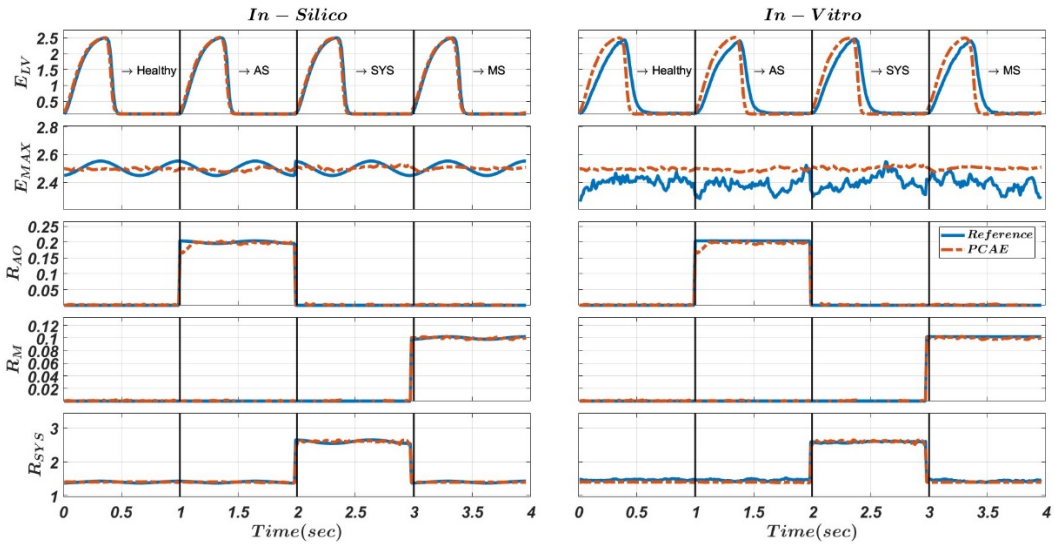


Figure 5.7. PCAE critical parameter responses to in-silico model and in-vitro device [117]

The other parameters $R_{ao}(t), R_M(t)$ and $R_{SYS}(t)$ have perfectly converged to their reference physiological values [76], [88], [117], [130].

Notice that even though the model is trained on the in-silico tests, overall performance of the PCAE is acceptably well when driven by the in-vitro tests for all cases studied.

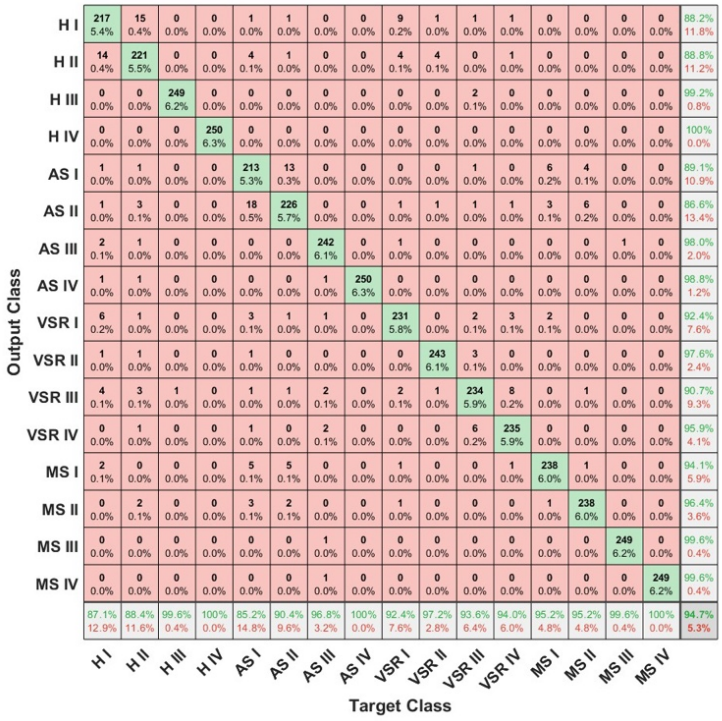


Figure 5.8. Confusion matrix of the CVS diagnostics model classification

The classification performance of each class is shown in the confusion matrix depicted in Figure 5.8. Although the overall performance of 94.76% correct classification is found to be satisfactory, it suggests even better results by paying attention to the following observations. The model's confusion between H-I and H-II as well as AS-I and AS-II is likely to be due to the assumptions made in Table 5.1. Especially for H-I and H-II, the acceptable E_{MAX} and P_{LV} values were increased in the healthy physiological range while V_{LV} was kept constant in accordance with the frank-starling law [81]. Similar observation has been noticed for AS-I and AS-II case, where the V_{LV} is kept constant through the time response.

In order to show a statistical performance of the proposed diagnostics model, F1 score together with the Matthews Correlation Coefficient (MCC) [131] and the kappa statistics [132] given in Table 5.3. MCC is added to take into account of the imbalance between "in-silico" and "in-vitro" tests and the kappa statistics is included to illustrate interrater reliability.

Thus, Table 5.3 indicates that the use of in-silico and in-vitro tests on CVD conditions results in a reliable classification by the proposed model.

Table 5.3 Classification results of CVS data

	Overall F1: 94.76%, Matthews Correlation: 94.32%		
Classes	MCC	Kappa	F1 Score
H Stage I	86.87%	87.72%	87.68%
H Stage II	87.82%	87.61%	88.58%
H Stage III	99.36%	87.47%	99.40%
H Stage IV	100.00%	87.49%	100.00%
AS Stage I	86.30%	87.87%	87.12%
AS Stage II	87.69%	87.32%	88.45%
AS Stage III	97.21%	87.59%	97.38%
AS Stage IV	99.37%	87.42%	99.40%
VSR Stage I	91.89%	87.56%	92.40%
VSR Stage II	97.22%	87.54%	97.39%
VSR Stage III	91.60%	87.36%	92.13%

Table 5.3 Classification results of CVS data (continued)

VSR Stage IV	94.62%	87.66%	94.95%
MS Stage I	94.27%	87.46%	94.63%
MS Stage II	95.50%	87.60%	95.77%
MS Stage III	99.57%	87.50%	99.60%
MS Stage IV	99.79%	87.52%	99.80%

5.4.2 Excitation of PCAE by Critical Parameters

The PCAE in the closed-loop operation produces cyclic CVS variable signals consistent with the literature. When a critical parameter defined within the latent space is deviated from its current condition to change the severity level, we observe that the model outputs, the principal variables, converge to the new state condition observed in in-vitro tests conducted by the hMCL device. Figure 5.9 shows the in-vitro data as reference with H-IV level triggered at 166 s when $\theta_2^* = E_{max}^*$ value is changed to the nominal condition of 2.5 ml/mmHg. The figure demonstrates the output transition of the PCAE model that is converging to the reference signals after a couple of cardiac cycles.

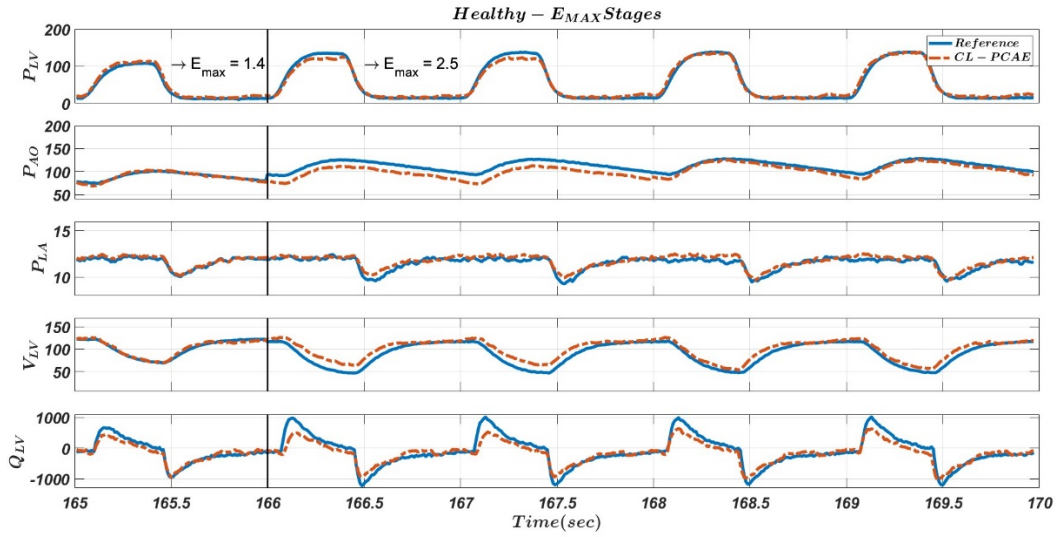


Figure 5.9. Transient response of CVS PVs to externally triggered Emax

We have, then, carried out similar experiments for the other parameters in different morbidity settings. Figure 5.10 depicts the PVs in H-I through H-IV conditions at the steady state.

The AS levels, AS-I – AS-IV, are emulated in the PCAE model by adjusting $\theta_3^* = R_{AO}^*$ and validated by hMCL responses. The steady-state cardiac cycle waveforms for each case are illustrated in Figure 5.11. It noteworthy to mention that only $P_{lv}(t)$ values are increased that is in accordance with the literature [92]. Besides, the LVV was decreased in time while $P_{la}(t)$ was not changed at all stages. It was considered another important property for modelling AS that is in consistent with physiological CVS dynamic. For systemic resistance changes, Figure 5.12 demonstrated the results of CL-PCAE outputs.

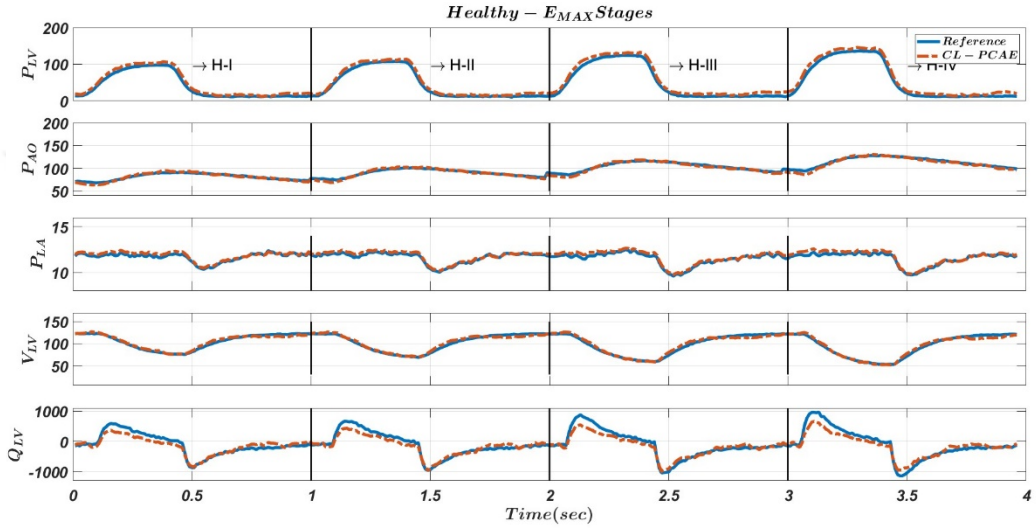


Figure 5.10. Healthy case of the CL-PCAE results

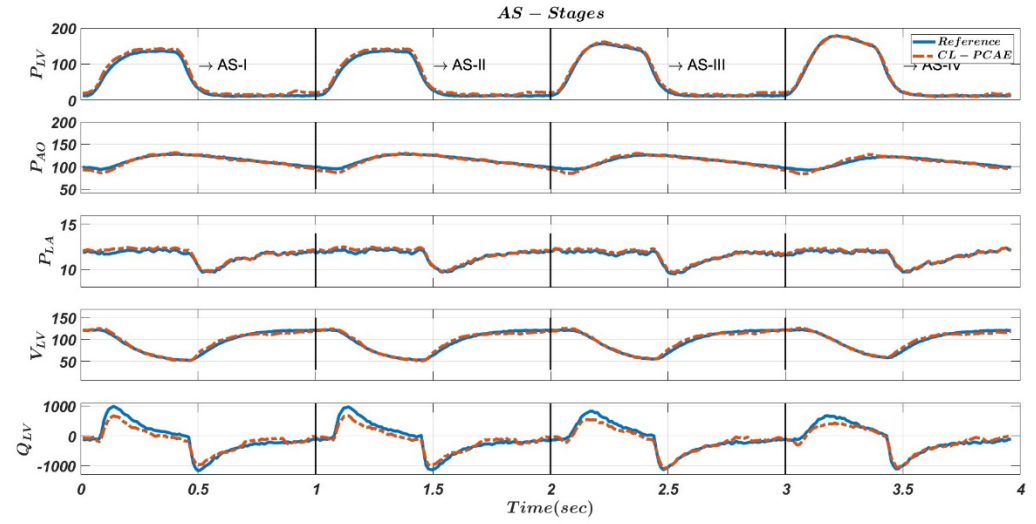


Figure 5.11. AS of the CL-PCAE results

The PCAE model in closed loop possessed perfectly matched results for the whole pressures. The increment on the AOP shown in Figure 5.12 is also in accordance with hMCL measurements. These responses perfectly matched the hMCL

measurements as well as physiological response of systemic resistance change [117].

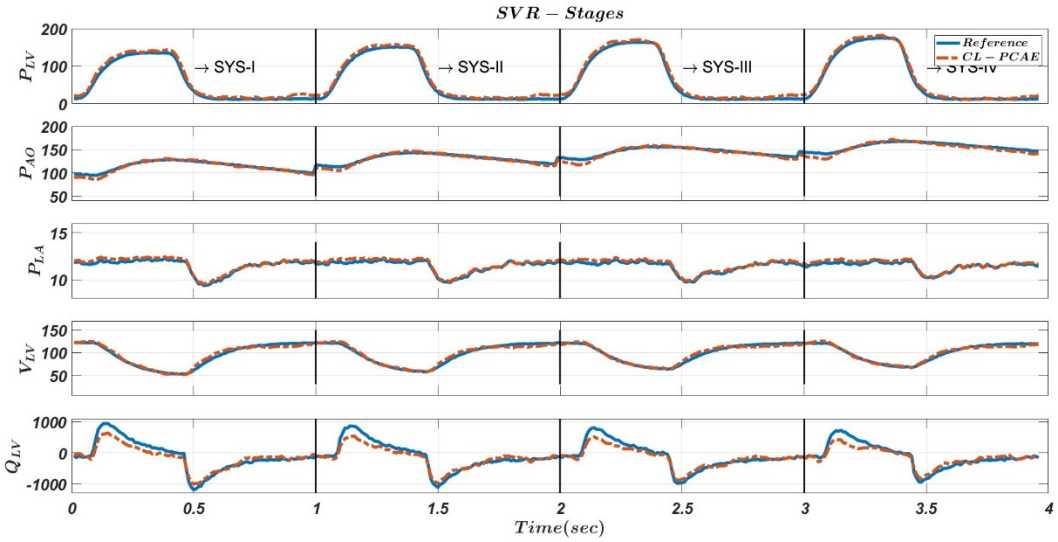


Figure 5.12. Systemic resistance change case of the CL-PCAE results

We have encountered eight different studies within our scope, and we compare our results from the proposed framework on CVS signals estimation to those reported in theirs. The error signal mean (%) and standart deviation (STD) values are listed in Table 5.4. Dabiri et al. establishes a machine learning technique to estimate the real-time left ventricular response using the finite element methods to train XGboost and Cubist network structure [109]. Their models yield high mean but low STD in errors in the left ventricular pressure and volume 0.939±0.067% and 0.923±0.050%. Regazzoni et al. worked on the left ventricular model with electrical and 3D modeling techniques to find proper outputs for the pressure and the volume [133]. The articles focused only on estimation of the LV end-systolic elastance value [34], [110], [126] using CNN and DNN models are employed on both LVAD designs and real patients. On the other hand, Yang et al. suggested an inverse problem for the seven parameters of the same model of ours together with E_{max} and E_{min} estimation based on nonlinear optimization assuming using the systemic arterial pressure [111]. The study given in [116] focuses only on VRC R_{sys} while [112] extends it to the contractility change and the left ventricular pressure. Both are built on EKF based estimation of the CVS parameters using LVAD device-based measurements. The proposed PCAE model trained on Simaan et al. model results in very competitive estimations over the critical parameters as summarized in the table.

5.5 Conclusion

In this study, a framework is proposed for estimating CVS parameters based on principal variables derived from CV measurements. The framework utilizes both in-silico (computer-simulated) and in-vitro (laboratory) measurements and addresses various conditions such as aortic and MS, LV elastance deviation, and systemic resistance changes in four different severity levels.

At the core of the framework lies an autoencoder (AE) type of deep neural network. The AE is designed with a partially guided latent space, which is influenced by physiological parametric signals. The input to the AE consists of principal CV signals such as pressures and flow rates, while physiological consciousness is induced through critical CVS parameters that cannot be directly measured using non-invasive methods. These parameters include the aortic resistance, mitral resistance, systemic resistance, and LV elastance.

. The standard loss function of the AE is modified to enable specific neurons in the latent space to learn predefined CVS parameters. Training datasets are generated using "in-silico" data obtained from a CVS model. To validate the proposed model, a hybrid mock loop device, constructed in-house, is used to collect corresponding CVS parameters and variables through in-vitro tests.

The results of the in-vitro tests demonstrate that the proposed deep neural network successfully predicts the principal CV variables and critical parameters with a mean error below 5.7% across a wide range of normal and abnormal conditions.

In addition to CVS parameter estimation, a diagnostics model is developed using only the latent space vector. This diagnostics model classifies CVS conditions into four severity levels. The overall F1 score, which measures the model's accuracy, for predicting all CVDs is reported as 98.55% for all cases studied.

The proposed framework proves to be effective in estimating CVS parameters and predicting CVS conditions in the four severity levels examined. The study suggests that the framework holds promise for extension to other CV conditions.

Table 5.4 Comparison of estimation of CVS parameters

	(%)	R_{SYS}	R_M	E_{MAX}	P_{LV}	V_{LV}
Physiological Ventricle	Dabiri et al.[109]	-	-	-	0.939 ±0.067	0.923 ±0.050
	Bonnemain et al. [126]	-	-	1.10 ±0.88	-	-
	Laubsher et al. [34]	-	-	0.37 ±NA	-	-
	Bikia et al. [110]	-	-	6.4 ±5.00	-	-
	Regazzoni et al. [133]	-	-	-	0.51 ±NA	0.22 ±NA
	Yang et al.[111]	0.3 ±NA	-0.54 ±NA	-0.29 ±NA	-	-
	Rapp et al. [116]	1.3 ±0.43	-	-	-	-
	Pawar et al. [112]	3.4 ±NA	-	1.53 ±NA	4.67 ±1.06	-
	The PCAE (in-silico)	-0.09 ±0.01	-0.41 ±0.57	0.24 ±2.52	-0.58 ±1.36	-0.04 ±1.57
	The PCAE (in-vitro)	4.65 ±1.65	-0.32 ±0.57	-6.07 ±4.03	-4.34 ±1.86	-0.49 ±4.16

6
CONCLUSION

The proposed thesis presented a novel heart valve model that incorporated parameter selections to accurately represent physiological patterns, including healthy, aortic stenosis, and regurgitation conditions. The model utilized a nonlinear mass-spring-damper approach to simulate the motion of the elastic leaflet body, coupled with a cardiovascular lumped parameter model. By considering factors such as time-varying fluid resistance, aortic flow rate, left ventricular and aortic pressures, and leaflet pose, the model successfully demonstrated phenomena such as backflow, vortex formation, and the dicrotic notch, aligning with the gold standard in physiological evaluation. Additionally, the model revealed a previously unobserved reverse pressure effect on the aortic valve during the diastolic phase. Physiological validation involved comparing the model with reference models and previously reported physiological data. The determined nominal leaflet spring and damping parameters for the healthy valve, aortic stenosis, and aortic regurgitation provided similar patterns of left ventricular and aortic pressure, as well as leaflet opening-closing angles. The model also enabled the observation of blood flow rate reduction in aortic regurgitation, which was not documented in the existing literature. In conclusion, the novel model parameterized critical aortic valve conditions, demonstrated physiological phenomena, and provided a comprehensive framework to simulate various aortic valve conditions.

In the second place, the thesis introduced a novel design and control approach for a hybrid mock circulatory loop (hMCL) used in hemodynamic simulations of critical cardiovascular diseases. The stability proofs of the closed-loop hMCL confirmed its ability to drive proportional valves using a discrete feedback linearization rule. The study presented a new left ventricle volume-elastance equation that combined the autoregulation of the Frank-Starling mechanism with left ventricular contractility. Unlike conventional approaches, the hMCL primarily relied on the volume of the left ventricular gas chamber as the driving force, while ensuring the alignment of other parameters with human data. Notably, the reference signal for the hMCL did not require prior functions or data, except for the maximum and minimum values of left ventricular volume. The performance evaluation of the

hMCL involved obtaining cardiovascular parameters from human data and conducting simulations and experiments to investigate scenarios such as aortic stenosis, changes in systemic vascular resistance, and variations in heart rate. The hMCL demonstrated that increasing heart rate enhanced left ventricular contractility while maintaining consistent physiological pressures. However, this increased contractility was accompanied by a decrease in left ventricular volume, consistent with human data. The hMCL also revealed that aortic stenosis caused an increase in both left ventricular and aortic pressures. Moreover, when systemic vascular resistance changed, the hMCL preserved left ventricular pressure while elevating aortic pressure. The proposed hMCL provided high flexibility and reproducibility, enabling the testing of a wide range of cardiovascular conditions.

In the third place, the thesis presented an improved model for dynamic aortic valve resistance (AVR) using a convolutional neural network (CNN) and a hybrid approach combining "in-silico" and "in-vitro" measurements. The model utilized an aortic valve (AV) model and "in-vitro" measurements enhanced through an extended Kalman filter, providing a rich set of input for efficient deep learning. By converting time signals into a 2D format, the CNN predicted the residue of AVR between the model and "in-vitro" measurements, enabling the estimation of dynamic AVR during the ejection phase. A hybrid mock circulatory loop (hMCL) was employed to validate the proposed estimator in a realistic "in-vitro" testing environment, where one parameter was controlled while allowing others to vary freely to satisfy the Frank-Starling mechanism. The approach enabled accurate real-time observation of fluid mass flow rate of the left ventricle and AVR for the ejection phase using noninvasive measurements. The hMCL results demonstrated the alignment of left ventricular flow rate with reference data, with a low error rate for cardiac output in healthy and aortic stenosis conditions. The proposed model offered a powerful and dynamic AVR estimation, improving upon existing studies that only focused on steady-state AVR at specific conditions.

Finally, the thesis introduced a framework that combined "in vitro" and "in silico" measurements to estimate cardiovascular parameters and diagnose cardiovascular conditions. The framework incorporated a modified autoencoder with a partially guided latent space, allowing for the inclusion of physiological consciousness within the deep neural network. Time-delayed cardiovascular signals, including

pressures, flow rates, and cardiovascular system (CVS) parameters that were not directly measurable, were used as inputs to learn the augmented latent space connectivity. The autoencoder's standard loss function was designed to predict the input signals and CVS parameters that played significant roles in the studied cases, including left ventricle elastance deviation, mitral stenosis, aortic stenosis, and changes in systemic vascular resistance. Labeled training datasets were generated from "in-silico" data obtained from a common CVS model. The proposed models were validated using a hybrid mock loop device, which collected corresponding CVS critical parameters and principal variables through in-vitro tests. The results demonstrated the reproduction of CVS signals with a low error rate. When the model was used in a closed-loop setup and critical parameters were perturbed externally, convergence of the CVS variables to those of the new condition was observed. The diagnostics model exhibited a high capability to classify the severity level of cardiovascular diseases across a wide range of cases, with an overall F1 score of 94.76%.

REFERENCES

[1] A. Stefanovska, "Physics of the human cardiovascular system," *Contemporary Physics*, vol. 40, no. 1, pp. 31–55, Jan. 1999, doi: 10.1080/001075199181693.

[2] S. Mantri, S. M. Wu, and W. R. Goodyer, "Molecular profiling of the cardiac conduction system: the dawn of a new era," *Curr Cardiol Rep*, vol. 23, no. 8, p. 103, Jul. 2021, doi: 10.1007/s11886-021-01536-w.

[3] C. Yilmaz, M. Iscan, and A. Yilmaz, "A fully automatic novel method to determine qt interval based on continuous wavelet transform," *IU-Journal of Electrical & Electronics Engineering*, vol. 17, no. 1, Art. no. 1, Mar. 2017.

[4] M. Iscan, F. Yığıt, and C. Yilmaz, "Heartbeat pattern classification algorithm based on Gaussian mixture model," in *2016 IEEE International Symposium on Medical Measurements and Applications (MeMeA)*, May 2016, pp. 1–6. doi: 10.1109/MeMeA.2016.7533715.

[5] M. Iscan, F. Yigit, and C. Yilmaz, "T-wave end pattern classification based on Gaussian mixture model," in *2016 24th Signal Processing and Communication Application Conference (SIU)*, May 2016, pp. 1953–1956. doi: 10.1109/SIU.2016.7496149.

[6] M. Iscan, Ş. Sariozkan, A. Yilmaz, and C. Yilmaz, "Multilead QT interval analysis algorithm based on continuous wavelet transform," in *2017 4th International Conference on Electrical and Electronic Engineering (ICEEE)*, Apr. 2017, pp. 318–322. doi: 10.1109/ICEEE2.2017.7935842.

[7] A. Noordergraaf, *Circulatory System Dynamics*. Elsevier, 2012.

[8] J.-L. Vincent, "Understanding cardiac output," *Critical Care*, vol. 12, no. 4, p. 174, Aug. 2008, doi: 10.1186/cc6975.

[9] R. Jacob, B. Dierberger, and G. Kissling, "Functional significance of the Frank-Starling mechanism under physiological and pathophysiological conditions," *Eur Heart J*, vol. 13 Suppl E, pp. 7–14, Nov. 1992, doi: 10.1093/eurheartj/13.suppl_e.7.

[10] D. G. Stephenson and D. A. Williams, "Effects of sarcomere length on the force—pCa relation in fast- and slow-twitch skinned muscle fibres from the rat," *J Physiol*, vol. 333, pp. 637–653, 1982.

[11] A. P. Yoganathan, Z. He, and S. Casey Jones, "Fluid mechanics of heart valves," *Annu Rev Biomed Eng*, vol. 6, pp. 331–362, 2004, doi: 10.1146/annurev.bioeng.6.040803.140111.

[12] K. Zilinskas, J. H. Kwon, K. Bishara, K. Hayden, R. Quintao, and T. K. Rajab, "Physiological ventricular simulator for valve surgery training," *Bioengineering*, vol. 9, no. 6, Art. no. 6, Jun. 2022, doi: 10.3390/bioengineering9060264.

[13] V. Tuncay and P. M. A. van Ooijen, "3D printing for heart valve disease: a systematic review," *European Radiology Experimental*, vol. 3, no. 1, p. 9, Feb. 2019, doi: 10.1186/s41747-018-0083-0.

[14] J. Soler-Soler and E. Galve, “Worldwide perspective of valve disease,” *Heart*, vol. 83, no. 6, pp. 721–725, Jun. 2000, doi: 10.1136/heart.83.6.721.

[15] F. Nestler, A. P. Bradley, S. J. Wilson, D. L. Timms, O. H. Frazier, and W. E. Cohn, “A hybrid mock circulation loop for a total artificial heart,” *Artif Organs*, vol. 38, no. 9, pp. 775–782, Sep. 2014, doi: 10.1111/aor.12380.

[16] L. C. Lee, G. S. Kassab, and J. M. Guccione, “Mathematical modeling of cardiac growth and remodeling,” *Wiley Interdiscip Rev Syst Biol Med*, vol. 8, no. 3, pp. 211–226, May 2016, doi: 10.1002/wsbm.1330.

[17] J. Gehron *et al.*, “Development and validation of a life-sized mock circulatory loop of the human circulation for fluid-mechanical studies,” *ASAIO Journal*, vol. 65, no. 8, pp. 788–797, Dec. 2019, doi: 10.1097/MAT.0000000000000880.

[18] M. Swathy and K. Saruladha, “A comparative study of classification and prediction of Cardio-Vascular Diseases (CVD) using Machine Learning and Deep Learning techniques,” *ICT Express*, vol. 8, no. 1, pp. 109–116, Mar. 2022, doi: 10.1016/j.icte.2021.08.021.

[19] N. G. Kang, Y. J. Suh, K. Han, Y. J. Kim, and B. W. Choi, “Performance of prediction models for diagnosing severe aortic stenosis based on aortic valve calcium on cardiac computed tomography: incorporation of radiomics and machine learning,” *Korean J Radiol*, vol. 22, no. 3, pp. 334–343, Mar. 2021, doi: 10.3348/kjr.2020.0099.

[20] J. Kwon *et al.*, “Deep learning–based algorithm for detecting aortic stenosis using electrocardiography,” *Journal of the American Heart Association*, vol. 9, no. 7, p. e014717, Apr. 2020, doi: 10.1161/JAHA.119.014717.

[21] World Health Organization, “Cardiovascular diseases (CVDs),” 2021. https://www.who.int/news-room/fact-sheets/detail/cardiovascular-diseases-(cvds) (accessed Aug. 11, 2022).

[22] V. T. Nkomo, J. M. Gardin, T. N. Skelton, J. S. Gottdiener, C. G. Scott, and M. Enriquez-Sarano, “Burden of valvular heart diseases: a population-based study,” *Lancet*, vol. 368, no. 9540, pp. 1005–1011, Sep. 2006, doi: 10.1016/S0140-6736(06)69208-8.

[23] M. H. Yacoub and J. J. M. Takkenberg, “Will heart valve tissue engineering change the world?,” *Nat Rev Cardiol*, vol. 2, no. 2, Art. no. 2, Feb. 2005, doi: 10.1038/ncpcardio0112.

[24] J. T. Butcher, G. J. Mahler, and L. A. Hockaday, “Aortic valve disease and treatment: the need for naturally engineered solutions,” *Adv Drug Deliv Rev*, vol. 63, no. 4–5, pp. 242–268, Apr. 2011, doi: 10.1016/j.addr.2011.01.008.

[25] B. J. Bellhouse, “Fluid mechanics of a model mitral valve and left ventricle,” *Cardiovasc Res*, vol. 6, no. 2, pp. 199–210, Mar. 1972, doi: 10.1093/cvr/6.2.199.

[26] A. S. Sadée, A. E. Becker, and J. A. Verheul, “The congenital bicuspid aortic valve with post-inflammatory disease--a neglected pathological diagnosis of clinical relevance,” *Eur Heart J*, vol. 15, no. 4, pp. 503–506, Apr. 1994, doi: 10.1093/oxfordjournals.eurheartj.a060534.

[27] J. Davila, “The mechanics of cardiac valves,” *Prosthetic Valves for Cardiac*

Surgery., pp. 3–21, 1960.

[28] G.-R. Hong *et al.*, "Characterization and quantification of vortex flow in the human left ventricle by contrast echocardiography using vector particle image velocimetry," *JACC Cardiovasc Imaging*, vol. 1, no. 6, pp. 705–717, Nov. 2008, doi: 10.1016/j.jcmg.2008.06.008.

[29] J. T. Ottesen, M. S. Olufsen, and J. K. Larsen, *Applied mathematical models in human physiology*, 1st edition. Philadelphia: SIAM: Society for Industrial and Applied Mathematics, 2004.

[30] K. Imanaka, S. Takamoto, T. Ohtsuka, T. Oka, A. Furuse, and S. Omata, "The stiffness of normal and abnormal mitral valves," *Ann Thorac Cardiovasc Surg*, vol. 13, no. 3, pp. 178–184, Jun. 2007.

[31] L. E. Ford, T. Feldman, and J. D. Carroll, "Valve resistance," *Circulation*, vol. 89, no. 2, pp. 893–895, Feb. 1994, doi: 10.1161/01.cir.89.2.893.

[32] T. Korakianitis and Y. Shi, "A concentrated parameter model for the human cardiovascular system including heart valve dynamics and atrioventricular interaction," *Med Eng Phys*, vol. 28, no. 7, pp. 613–628, Sep. 2006, doi: 10.1016/j.medengphy.2005.10.004.

[33] Y. Aboelkassem, D. Savic, and S. G. Campbell, "Mathematical modeling of aortic valve dynamics during systole," *J Theor Biol*, vol. 365, pp. 280–288, Jan. 2015, doi: 10.1016/j.jtbi.2014.10.027.

[34] R. Laubscher, J. Van Der Merwe, P. Herbst, and J. Liebenberg, "Estimation of simulated left ventricle elastance using lumped parameter modelling and gradient-based optimization with forward-mode automatic differentiation based on synthetically generated noninvasive data," *J Biomech Eng*, vol. 145, no. 2, p. 021008, Feb. 2023, doi: 10.1115/1.4055565.

[35] R. Laubscher, J. Van Der Merwe, P. G. Herbst, and J. Liebenberg, "Estimation of pulmonary arterial pressure using simulated non-invasive measurements and gradient-based optimization techniques," *Mathematical and Computational Applications*, vol. 27, no. 5, Art. no. 5, Oct. 2022, doi: 10.3390/mca27050083.

[36] R. Laubscher, J. van der Merwe, J. Liebenberg, and P. Herbst, "Dynamic simulation of aortic valve stenosis using a lumped parameter cardiovascular system model with flow regime dependent valve pressure loss characteristics," *Med Eng Phys*, vol. 106, p. 103838, Aug. 2022, doi: 10.1016/j.medengphy.2022.103838.

[37] G. A. Fishbein and M. C. Fishbein, "Pathology of the aortic valve: aortic valve stenosis/aortic regurgitation," *Curr Cardiol Rep*, vol. 21, no. 8, p. 81, Jul. 2019, doi: 10.1007/s11886-019-1162-4.

[38] T. Pawade, T. Sheth, E. Guzzetti, M. R. Dweck, and M.-A. Clavel, "Why and how to measure aortic valve calcification in patients with aortic stenosis," *JACC Cardiovasc Imaging*, vol. 12, no. 9, pp. 1835–1848, Sep. 2019, doi: 10.1016/j.jcmg.2019.01.045.

[39] V. C. A. Koh, null Einly Lim, null Boon Chiang Ng, null Yong Kuen Ho, and N. H. Lovell, "A simplified state-space model of biventricular assist device-cardiovascular system interaction," *Annu Int Conf IEEE Eng Med Biol Soc*, vol. 2016, pp. 4317–4320, Aug. 2016, doi:

10.1109/EMBC.2016.7591682.

[40] J. Palladino *et al.*, "Assessing the state of the circulatory system via parameters vs. variables," vol. 13, pp. 131–139, Jan. 1996.

[41] C. Pozrikidis, *Fluid Dynamics: Theory, Computation, and Numerical Simulation*. Springer US, 2016.

[42] J. P. Mulier, "Ventricılar pressure as a function of volume and flow," PhD Thesis, KU Leuven, 1994.

[43] M. S. Leaning, H. E. Pullen, E. R. Carson, and L. Finkelstein, "Modelling a complex biological system: the human cardiovascular system—1. Methodology and model description," *Transactions of the Institute of Measurement and Control*, vol. 5, no. 2, pp. 71–86, Apr. 1983, doi: 10.1177/014233128300500202.

[44] F. Liang and H. Liu, "A closed-loop lumped parameter computational model for human cardiovascular system," *JSME International Journal Series C*, vol. 48, pp. 484–493, Jan. 2005, doi: 10.1299/jsmec.48.484.

[45] A. Quarteroni, "Modeling the cardiovascular system: a mathematical challenge," in *Mathematics Unlimited — 2001 and Beyond*, B. Engquist and W. Schmid, Eds., Berlin, Heidelberg: Springer, 2001, pp. 961–970. doi: 10.1007/978-3-642-56478-9_48.

[46] A. Quarteroni, "Mathematical modelling of the cardiovascular system," vol. 3, May 2003.

[47] E. B. Shim, J. Y. Sah, and C. H. Youn, "Mathematical modeling of cardiovascular system dynamics using a lumped parameter method," *Jpn J Physiol*, vol. 54, no. 6, pp. 545–553, Dec. 2004, doi: 10.2170/jjphysiol.54.545.

[48] A. Mirnajafi, J. M. Raymer, L. R. McClure, and M. S. Sacks, "The flexural rigidity of the aortic valve leaflet in the commissural region," *J Biomech*, vol. 39, no. 16, pp. 2966–2973, 2006, doi: 10.1016/j.jbiomech.2005.10.026.

[49] C. Peskin, "The fluid dynamics of heart valves: experimental, theoretical, and computational methods," *Annual Review of Fluid Mechanics*, vol. 14, pp. 235–259, Nov. 2003, doi: 10.1146/annurev.fl.14.010182.001315.

[50] Z. Zhong *et al.*, "Visualization of human aortic valve dynamics using magnetic resonance imaging with sub-millisecond temporal resolution," *J Magn Reson Imaging*, vol. 54, no. 4, pp. 1246–1254, Oct. 2021, doi: 10.1002/jmri.27603.

[51] W. C. Roberts, J. K. Perloff, and T. Costantino, "Severe valvular aortic stenosis in patients over 65 years of age. A clinicopathologic study," *Am J Cardiol*, vol. 27, no. 5, pp. 497–506, May 1971, doi: 10.1016/0002-9149(71)90412-7.

[52] M. Bäck, T. C. Gasser, J.-B. Michel, and G. Caligiuri, "Biomechanical factors in the biology of aortic wall and aortic valve diseases," *Cardiovasc Res*, vol. 99, no. 2, pp. 232–241, Jul. 2013, doi: 10.1093/cvr/cvt040.

[53] J. Ross, E. Braunwald, J. H. Gault, D. T. Mason, and A. G. Morrow, "The mechanism of the intraventricular pressure gradient in idiopathic hypertrophic subaortic stenosis," *Circulation*, vol. 34, no. 4, pp. 558–578, Oct. 1966, doi: 10.1161/01.CIR.34.4.558.

[54] H. N. Sabbah, D. T. Anbe, and P. D. Stein, "Negative intraventricular diastolic

pressure in patients with mitral stenosis: evidence of left ventricular diastolic suction," *Am J Cardiol*, vol. 45, no. 3, pp. 562–566, Mar. 1980, doi: 10.1016/s0002-9149(80)80005-1.

[55] N. Saikrishnan, G. Kumar, F. J. Sawaya, S. Lerakis, and A. P. Yoganathan, "Accurate assessment of aortic stenosis: a review of diagnostic modalities and hemodynamics," *Circulation*, vol. 129, no. 2, pp. 244–253, Jan. 2014, doi: 10.1161/CIRCULATIONAHA.113.002310.

[56] R. A. Nishimura, "Aortic valve disease," *Circulation*, vol. 106, no. 7, pp. 770–772, Aug. 2002, doi: 10.1161/01.CIR.0000027621.26167.5E.

[57] B. R. Travis, B. L. Fowler, and F. Robicsek, "A method for the measurement of left ventricular overload for aortic valve insufficiency," *J Biomech*, vol. 42, no. 12, pp. 1935–1940, Aug. 2009, doi: 10.1016/j.jbiomech.2009.05.020.

[58] J.-C. Han, A. J. Taberner, D. S. Loiselle, and K. Tran, "Cardiac efficiency and Starling's Law of the Heart," *J Physiol*, vol. 600, no. 19, pp. 4265–4285, Oct. 2022, doi: 10.1113/JP283632.

[59] P. I. Aaronson, J. P. T. Ward, and M. J. Connolly, *The cardiovascular system at a glance*, Fifth edition. in At a glance series. Hoboken, NJ: Wiley-Blackwell, 2020.

[60] S. Romiti, M. Vinciguerra, W. Saade, I. Anso Cortajarena, and E. Greco, "Artificial intelligence (ai) and cardiovascular diseases: an unexpected alliance," *Cardiology Research and Practice*, vol. 2020, pp. 1–8, Jun. 2020, doi: 10.1155/2020/4972346.

[61] J. Haas *et al.*, "In vivo assay guidelines," in *Assay Guidance Manual*, Bethesda (MD): Eli Lilly & Company and the National Center for Advancing Translational Sciences, 2004. Accessed: Jun. 14, 2023. [Online]. Available: http://www.ncbi.nlm.nih.gov/books/NBK92013/

[62] Y. Orime *et al.*, "In vitro and in vivo validation tests for total artificial heart," *Artificial Organs*, vol. 18, no. 1, pp. 54–72, Jan. 1994, doi: 10.1111/j.1525-1594.1994.tb03299.x.

[63] C. Newmarker, "8 types of FDA-approved devices that treat the heart," *Medical Design and Outsourcing*, Feb. 13, 2020. https://www.fda.gov/consumers/consumer-updates/fda-approved-devices-help-keep-heart-beating (accessed Aug. 14, 2022).

[64] S. Schampaert, K. A. M. A. Pennings, M. J. G. van de Molengraft, N. H. J. Pijls, F. N. van de Vosse, and M. C. M. Rutten, "A mock circulation model for cardiovascular device evaluation," *Physiol. Meas.*, vol. 35, no. 4, pp. 687–702, Apr. 2014, doi: 10.1088/0967-3334/35/4/687.

[65] G. Ferrari *et al.*, "A hybrid (numerical-physical) model of the left ventricle," *Int J Artif Organs*, vol. 24, no. 7, pp. 456–462, Jul. 2001, doi: 10.1177/039139880102400705.

[66] L. Fresiello, A. W. Khir, A. Di Molfetta, M. Kozarski, and G. Ferrari, "Effects of intra-aortic balloon pump timing on baroreflex activities in a closed-loop cardiovascular hybrid model," *Artif Organs*, vol. 37, no. 3, pp. 237–247, Mar. 2013, doi: 10.1111/j.1525-1594.2012.01540.x.

[67] J. N. Warnock, S. Konduri, Z. He, and A. P. Yoganathan, "Design of a sterile

organ culture system for the ex vivo study of aortic heart valves," *Journal of Biomechanical Engineering*, vol. 127, no. 5, pp. 857–861, Oct. 2005, doi: 10.1115/1.1992535.

[68] F. Cappon, T. Wu, T. Papaioannou, X. Du, P.-L. Hsu, and A. W. Khir, "Mock circulatory loops used for testing cardiac assist devices: A review of computational and experimental models," *Int J Artif Organs*, vol. 44, no. 11, pp. 793–806, Nov. 2021, doi: 10.1177/03913988211045405.

[69] H. Suga, K. Sagawa, and A. A. Shoukas, "Load independence of the instantaneous pressure-volume ratio of the canine left ventricle and effects of epinephrine and heart rate on the ratio," *Circulation Research*, vol. 32, no. 3, pp. 314–322, Mar. 1973, doi: 10.1161/01.RES.32.3.314.

[70] P. H. M. Bovendeerd, P. Borsje, T. Arts, and F. N. van De Vosse, "Dependence of intramyocardial pressure and coronary flow on ventricular loading and contractility: a model study," *Ann Biomed Eng*, vol. 34, no. 12, pp. 1833–1845, Dec. 2006, doi: 10.1007/s10439-006-9189-2.

[71] S. Duschek, M. Muckenthaler, N. Werner, and G. A. Reyes del Paso, "Relationships between features of autonomic cardiovascular control and cognitive performance," *Biological Psychology*, vol. 81, no. 2, pp. 110–117, May 2009, doi: 10.1016/j.biopsycho.2009.03.003.

[72] K. Gwak, M. D. Noh, B. E. Paden, and J. F. Antaki, "Fluidic operational amplifier for mock circulatory systems - simulation and experimental results," in *Proceedings of the 2005, American Control Conference, 2005.*, Portland, OR, USA: IEEE, 2005, pp. 3817–3822. doi: 10.1109/ACC.2005.1470569.

[73] K. R. Walley, "Left ventricular function: time-varying elastance and left ventricular aortic coupling," *Crit Care*, vol. 20, no. 1, p. 270, Dec. 2016, doi: 10.1186/s13054-016-1439-6.

[74] L. A. Baloa, J. R. Boston, and J. F. Antaki, "Elastance-based control of a mock circulatory system," *Annals of Biomedical Engineering*, vol. 29, no. 3, pp. 244–251, Mar. 2001, doi: 10.1114/1.1355275.

[75] G. Ferrari *et al.*, "A hybrid mock circulatory system: testing a prototype under physiologic and pathological conditions:," *ASAIO Journal*, vol. 48, no. 5, pp. 487–494, Sep. 2002, doi: 10.1097/00002480-200209000-00009.

[76] F. M. Colacino, F. Moscato, F. Piedimonte, G. Danieli, S. Nicosia, and M. Arabia, "A modified elastance model to control mock ventricles in real-time: numerical and experimental validation," *ASAIO Journal*, vol. 54, no. 6, pp. 563–573, Nov. 2008, doi: 10.1097/MAT.0b013e31818a5c93.

[77] M. Loh and Yih-Choung Yu, "Feedback control design for an elastance-based mock circulatory system," in *Proceedings of the 2004 American Control Conference*, Boston, MA, USA: IEEE, 2004, pp. 1639–1644 vol.2. doi: 10.23919/ACC.2004.1386812.

[78] M. A. Simaan, A. Ferreira, S. Chen, J. F. Antaki, and D. G. Galati, "A dynamical state space representation and performance analysis of a feedback-controlled rotary left ventricular assist device," *IEEE Trans. Contr. Syst. Technol.*, vol. 17, no. 1, pp. 15–28, Jan. 2009, doi: 10.1109/TCST.2008.912123.

[79] Y. Yokoyama, O. Kawaguchi, T. Shinshi, U. Steinseifer, and S. Takatani, “A new pulse duplicator with a passive fill ventricle for analysis of cardiac dynamics,” *J Artif Organs*, vol. 13, no. 4, pp. 189–196, Dec. 2010, doi: 10.1007/s10047-010-0518-8.

[80] G. Ferrari, M. Kozarski, C. De Lazzari, K. G. Ska, G. Tosti, and M. Darowski, “Development of a hybrid (numerical-hydraulic) circulatory model: prototype testing and its response to iabp assistance,” *Int J Artif Organs*, vol. 28, no. 7, pp. 750–759, Jul. 2005, doi: 10.1177/039139880502800714.

[81] S. D. Gregory, M. Stevens, D. Timms, and M. Pearcy, “Replication of the Frank-Starling response in a mock circulation loop,” in *2011 Annual International Conference of the IEEE Engineering in Medicine and Biology Society*, Boston, MA: IEEE, Aug. 2011, pp. 6825–6828. doi: 10.1109/IEMBS.2011.6091683.

[82] S.-H. Jansen-Park *et al.*, “Effects of interaction between ventricular assist device assistance and autoregulated mock circulation including frank-starling mechanism and baroreflex,” *Artif Organs*, vol. 40, no. 10, pp. 981–991, Oct. 2016, doi: 10.1111/aor.12635.

[83] E. Mirzaei, M. Farahmand, and E. Kung, “An algorithm for coupling multibranch in vitro experiment to numerical physiology simulation for a hybrid cardiovascular model,” *Int J Numer Meth Biomed Engng*, vol. 36, no. 3, Mar. 2020, doi: 10.1002/cnm.3289.

[84] S. D. Gregory *et al.*, “An advanced mock circulation loop for in vitro cardiovascular device evaluation,” *Artif Organs*, vol. 44, no. 6, Jun. 2020, doi: 10.1111/aor.13636.

[85] T. Salesch, J. Gesenhues, M. Habigt, M. Mechelinck, M. Hein, and D. Abel, “Parameter optimization and validation of a cost efficient hybrid mock loop of the cardiovascular system,” in *2021 European Control Conference (ECC)*, Delft, Netherlands: IEEE, Jun. 2021, pp. 762–768. doi: 10.23919/ECC54610.2021.9654952.

[86] E. Vignali, E. Gasparotti, A. Mariotti, D. Haxhiademi, L. Ait-Ali, and S. Celi, “High-versatility left ventricle pump and aortic mock circulatory loop development for patient-specific hemodynamic in vitro analysis,” *ASAIO J*, vol. 68, no. 10, pp. 1272–1281, Oct. 2022, doi: 10.1097/MAT.0000000000001651.

[87] M. Rocchi, M. Ingram, P. Claus, J. D’hooge, B. Meyns, and L. Fresiello, “Use of 3D anatomical models in mock circulatory loops for cardiac medical device testing,” *Artificial Organs*, p. aor.14433, Nov. 2022, doi: 10.1111/aor.14433.

[88] E. S. Rapp, S. R. Pawar, and R. G. Longoria, “Hybrid mock circulatory loop simulation of extreme cardiac events,” *IEEE Trans. Biomed. Eng.*, vol. 69, no. 9, pp. 2883–2892, Sep. 2022, doi: 10.1109/TBME.2022.3156963.

[89] A. Packy, G. A. D’Souza, M. Farahmand, L. Herbertson, and C. G. Scully, “Simulating radial pressure waveforms with a mock circulatory flow loop to characterize hemodynamic monitoring systems,” *Cardiovasc Eng Tech*, vol. 13, no. 2, pp. 279–290, Apr. 2022, doi: 10.1007/s13239-021-00575-2.

[90] F. Bardi, E. Gasparotti, E. Vignali, S. Avril, and S. Celi, “A hybrid mock

circulatory loop for fluid dynamic characterization of 3d anatomical phantoms," *IEEE Trans. Biomed. Eng.*, pp. 1–11, 2022, doi: 10.1109/TBME.2022.3224581.

[91] S. Vandenberghe *et al.*, "Modeling ventricular function during cardiac assist: does time-varying elastance work?," *ASAIO Journal*, vol. 52, no. 1, pp. 4–8, Jan. 2006, doi: 10.1097/01.mat.0000196525.56523.b8.

[92] M. Iscan and A. Yesildirek, "Novel aortic heart valve model parameterizing normal and pathological cases: Aortic stenosis and regurgitation," *Transactions of the Institute of Measurement and Control*, p. 01423312231163363, Apr. 2023, doi: 10.1177/01423312231163363.

[93] M. Iscan, A. I. Tas, B. Vural, A. B. Ozden, and C. Yilmaz, "Antenna tracker design with a discrete lyapunov stability based controller for mini unmanned aerial vehicles," *IJMSIT*, vol. 6, no. 1, Art. no. 1, Jul. 2022.

[94] A. C. Guyton and J. E. Hall, *Medical physiology*, 10th edition. Elsevier Health Sciences, 2000.

[95] J.-E. Tarride *et al.*, "A review of the cost of cardiovascular disease," *Can J Cardiol*, vol. 25, no. 6, pp. e195–e202, Jun. 2009.

[96] W. Zhao *et al.*, "Surgical treatment of patients with aortic valve disease complicated with moderate functional mitral regurgitation and heart failure with midrange ejection fraction: a cohort study," *J Thorac Dis*, vol. 14, no. 8, pp. 2771–2780, Aug. 2022, doi: 10.21037/jtd-22-278.

[97] H. G. Bahraseman, E. M. Languri, N. Yahyapourjalaly, and D. M. Espino, "Fluid-structure interaction modeling of aortic valve stenosis at different heart rates," *Acta Bioeng Biomech*, vol. 18, no. 3, pp. 11–20, 2016.

[98] S. B. Shuvo, S. N. Ali, S. I. Swapnil, M. S. Al-Rakhami, and A. Gumaei, "CardioXNet: A novel lightweight deep learning framework for cardiovascular disease classification using heart sound recordings," *IEEE Access*, vol. 9, pp. 36955–36967, 2021, doi: 10.1109/ACCESS.2021.3063129.

[99] M. J. M. M. Hoeijmakers *et al.*, "Estimation of valvular resistance of segmented aortic valves using computational fluid dynamics," *J Biomech*, vol. 94, pp. 49–58, Sep. 2019, doi: 10.1016/j.jbiomech.2019.07.010.

[100] R. Couceiro *et al.*, "Beat-to-beat cardiac output inference using heart sounds," in *2011 Annual International Conference of the IEEE Engineering in Medicine and Biology Society*, Aug. 2011, pp. 5657–5661. doi: 10.1109/IEMBS.2011.6091369.

[101] K. S. Dyson, J. K. Shoemaker, P. Arbeille, and R. L. Hughson, "Modelflow estimates of cardiac output compared with Doppler ultrasound during acute changes in vascular resistance in women," *Experimental Physiology*, vol. 95, no. 4, pp. 561–568, 2010, doi: 10.1113/expphysiol.2009.050815.

[102] J. Koenig, L. K. Hill, D. P. Williams, and J. F. Thayer, "Estimating cardiac output from blood pressure and heart rate: the liljestrand & zander formula," *Biomed Sci Instrum*, vol. 51, pp. 85–90, 2015.

[103] N. Fazeli and J.-O. Hahn, "Estimation of cardiac output and peripheral resistance using square-wave-approximated aortic flow signal," *Front Physiol*, vol. 3, p. 298, 2012, doi: 10.3389/fphys.2012.00298.

[104] H. Xiao *et al.*, "Estimation of cardiac stroke volume from radial pulse waveform by artificial neural network," *Comput Methods Programs Biomed*, vol. 218, p. 106738, May 2022, doi: 10.1016/j.cmpb.2022.106738.

[105] N. J. Dabanloo, F. Adaei, and A. M. Nasrabadi, "The performance of neural network in the estimation of cardiac output using arterial blood pressure waveforms," in *2011 Computing in Cardiology*, Sep. 2011, pp. 145–148.

[106] Q. Guo and X. Wu, "Measuring cardiac output through thermodilution based on machine learning," *J. Mech. Med. Biol.*, vol. 21, no. 05, p. 2140003, Jun. 2021, doi: 10.1142/S0219519421400030.

[107] H.-L. Yang *et al.*, "Development and validation of an arterial pressure-based cardiac output algorithm using a convolutional neural network: retrospective study based on prospective registry data," *JMIR Med Inform*, vol. 9, no. 8, p. e24762, Aug. 2021, doi: 10.2196/24762.

[108] H.-L. Yang, H.-C. Lee, C.-W. Jung, and M.-S. Kim, "A deep learning method for intraoperative age-agnostic and disease-specific cardiac output monitoring from arterial blood pressure," in *2020 IEEE 20th International Conference on Bioinformatics and Bioengineering (BIBE)*, Oct. 2020, pp. 662–666. doi: 10.1109/BIBE50027.2020.00112.

[109] Y. Dabiri, A. Van der Velden, K. L. Sack, J. S. Choy, G. S. Kassab, and J. M. Guccione, "Prediction of left ventricular mechanics using machine learning," *Front Phys*, vol. 7, p. 117, Sep. 2019, doi: 10.3389/fphy.2019.00117.

[110] V. Bikia *et al.*, "Estimation of left ventricular end-systolic elastance from brachial pressure waveform via deep learning," *Frontiers in Bioengineering and Biotechnology*, vol. 9, 2021, doi: 10.3389/fbioe.2021.754003.

[111] X. Yang, J. S. Leandro, T. D. Cordeiro, and A. M. N. Lima, "An inverse problem approach for parameter estimation of cardiovascular system models," in *2021 43rd Annual International Conference of the IEEE Engineering in Medicine & Biology Society (EMBC)*, Nov. 2021, pp. 5642–5645. doi: 10.1109/EMBC46164.2021.9629603.

[112] S. R. Pawar, E. S. Rapp, J. R. Gohean, and R. G. Longoria, "Parameter identification of cardiovascular system model used for left ventricular assist device algorithms," *Journal of Engineering and Science in Medical Diagnostics and Therapy*, vol. 5, no. 1, p. 011006, Feb. 2022, doi: 10.1115/1.4053065.

[113] V. Bikia *et al.*, "Noninvasive estimation of aortic hemodynamics and cardiac contractility using machine learning," *Sci Rep*, vol. 10, no. 1, Art. no. 1, Sep. 2020, doi: 10.1038/s41598-020-72147-8.

[114] V. Bikia *et al.*, "Noninvasive cardiac output and central systolic pressure from cuff-pressure and pulse wave velocity," *IEEE J Biomed Health Inform*, vol. 24, no. 7, pp. 1968–1981, Jul. 2020, doi: 10.1109/JBHI.2019.2956604.

[115] Huan Huang, Ming Yang, Wangfu Zang, Shunjie Wu, and Yafei Pang, "In vitro identification of four-element Windkessel models based on iterated unscented kalman filter," *IEEE Trans. Biomed. Eng.*, vol. 58, no. 9, pp. 2672–2680, Sep. 2011, doi: 10.1109/TBME.2011.2161477.

[116] E. S. Rapp, S. R. Pawar, J. R. Gohean, E. R. Larson, R. W. Smalling, and

R. G. Longoria, “Estimation of systemic vascular resistance using built-in sensing from an implanted left ventricular assist device,” *Journal of Engineering and Science in Medical Diagnostics and Therapy*, vol. 2, no. 4, p. 041008, Nov. 2019, doi: 10.1115/1.4045204.

[117] M. Iscan and A. Yesildirek, “A new cardiovascular mock loop driven by novel active capacitance in normal and abnormal conditions,” submitted for publication.

[118] M. Iscan, A. I. Tas, B. Gurkan, and C. Yilmaz, “A novel elliptic trajectory formula for active RSSI-based antenna tracking algorithm,” *Transactions of the Institute of Measurement and Control*, p. 01423312231170925, May 2023, doi: 10.1177/01423312231170925.

[119] K. P. Murphy, *Machine learning: A probabilistic perspective*, Illustrated edition. Cambridge, MA: The MIT Press, 2012.

[120] D. P. Kingma and J. Ba, “Adam: A method for stochastic optimization,” *CoRR*, Dec. 2014, Accessed: Jun. 12, 2023. [Online]. Available: https://www.semanticscholar.org/paper/Adam%3A-A-Method-for-Stochastic-Optimization-Kingma-Ba/a6cb366736791bcccc5c8639de5a8f9636bf87e8

[121] M. Abdi, A. Karimi, M. Navidbakhsh, G. Pirzad Jahromi, and K. Hassani, “A lumped parameter mathematical model to analyze the effects of tachycardia and bradycardia on the cardiovascular system,” *International Journal of Numerical Modelling: Electronic Networks, Devices and Fields*, vol. 28, no. 3, pp. 346–357, 2015, doi: 10.1002/jnm.2010.

[122] R. G. Nadakinamani *et al.*, “Clinical data analysis for prediction of cardiovascular disease using machine learning techniques,” *Computational Intelligence and Neuroscience*, vol. 2022, p. e2973324, Jan. 2022, doi: 10.1155/2022/2973324.

[123] A. Shimazaki *et al.*, “Deep learning-based algorithm for lung cancer detection on chest radiographs using the segmentation method,” *Sci Rep*, vol. 12, no. 1, Art. no. 1, Jan. 2022, doi: 10.1038/s41598-021-04667-w.

[124] S. Sanchez-Martinez *et al.*, “Machine learning for clinical decision-making: challenges and opportunities in cardiovascular imaging,” *Frontiers in Cardiovascular Medicine*, vol. 8, 2022, doi: 10.3389/fcvm.2021.765693.

[125] Y. Zhou, Y. He, J. Wu, C. Cui, M. Chen, and B. Sun, “A method of parameter estimation for cardiovascular hemodynamics based on deep learning and its application to personalize a reduced-order model,” *Numer Methods Biomed Eng*, vol. 38, no. 1, Jan. 2022, doi: 10.1002/cnm.3533.

[126] J. Bonnemain, M. Zeller, L. Pegolotti, S. Deparis, and L. Liaudet, “Deep neural network to accurately predict left ventricular systolic function under mechanical assistance,” *Frontiers in Cardiovascular Medicine*, vol. 8, 2021, doi: 10.3389/fcvm.2021.752088.

[127] D. P. Stonko *et al.*, “A technical and data analytic approach to pressure-volume loops over numerous cardiac cycles,” *JVS-Vascular Science*, vol. 3, pp. 73–84, Jan. 2022, doi: 10.1016/j.jvssci.2021.12.003.

[128] B. A. Olshausen and D. J. Field, “Sparse coding with an overcomplete basis set: A strategy employed by V1?,” *Vision Research*, vol. 37, no. 23, pp. 3311–

3325, Dec. 1997, doi: 10.1016/S0042-6989(97)00169-7.

[129] X. Li, L. Yu, D. Chang, Z. Ma, and J. Cao, “Dual cross-entropy loss for small-sample fine-grained vehicle classification,” *IEEE Transactions on Vehicular Technology*, vol. 68, no. 5, pp. 4204–4212, May 2019, doi: 10.1109/TVT.2019.2895651.

[130] Y. N. V. Reddy, J. P. Murgo, and R. A. Nishimura, “Complexity of defining severe ‘stenosis’ from mitral annular calcification,” *Circulation*, vol. 140, no. 7, pp. 523–525, Aug. 2019, doi: 10.1161/CIRCULATIONAHA.119.040095.

[131] B. W. Matthews, “Comparison of the predicted and observed secondary structure of T4 phage lysozyme,” *Biochimica et Biophysica Acta (BBA) - Protein Structure*, vol. 405, no. 2, pp. 442–451, Oct. 1975, doi: 10.1016/0005-2795(75)90109-9.

[132] M. L. McHugh, “Interrater reliability: the kappa statistic,” *Biochem Med (Zagreb)*, vol. 22, no. 3, pp. 276–282, 2012.

[133] F. Regazzoni, M. Salvador, L. Dede’, and A. Quarteroni, “A machine learning method for real-time numerical simulations of cardiac electromechanics,” *Computer Methods in Applied Mechanics and Engineering*, vol. 393, p. 114825, Apr. 2022, doi: 10.1016/j.cma.2022.114825.

PUBLICATIONS FROM THE THESIS

Papers

1. M. Iscan and A. Yesildirek, “Novel aortic heart valve model parameterizing normal and pathological cases: Aortic stenosis and regurgitation,” Transactions of the Institute of Measurement and Control, p. 01423312231163363, Apr. 2023, doi: 10.1177/01423312231163363.

2. M. Iscan and A. Yesildirek, “A new cardiovascular mock loop driven by novel active capacitance in normal and abnormal conditions,” Applied Bionics and Biomechanics, 2023, submitted for publication.

3. M. Iscan and A. Yesildirek, “A novel framework to diagnose cardiovascular diseases using physiological conscious deep neural networks,” IEEE Access, 2023, submitted for publication.